國立臺灣大學理學院物理研究所

碩士論文

Department of Physics

Collage of Science

National Taiwan University

Master Thesis

B 介子至 η 介子和 h 介子之二體稀有衰變與電荷宇稱對稱破壞之量測

Measurements of Branching fractions and CP Asymmetries of B→ η h decays

許祖達

Chou Tat Hoi

指導教授：張寶棣

Advisor: Paoti Chang

中華民國 100 年 8 月

Acknowledgment

First I would like to thank my parents for their supports that allow me to finish the educations. Also, I am grateful to everyone who gives me comments and suggestion. Especially, I thank my advisor Paoti Chang, people work or study in Belle Collaboration, and members in NTUHEP.

中文摘要

在此篇論文中,我們使用了日本國家高能加速器中心 B 介子工廠 (KEKB) 及其 Belle 偵測器。我們從 772×10^{6} B 介子對中分析了 B 介子至 η 介子和 h 介子之二體稀有衰變與電荷宇稱對稱破壞。其中 η 介子由兩個光子或三個 π 介子重組而成。h 介子則分別代表了帶電 K 介子，電 π 介子和中性 K 介子。

最後我們在 $B^{+}\to\eta K^{+}$ 和 $B^{+}\to\eta\pi^{+}$ 衰變中找到超過 3σ 的電荷宇稱對稱破壞徵兆。同時我們也首次量測到 $B^{0}\to\eta K^{0}$ 衰變。

Abstract

We present the improved measurements of the $B \to \eta h$ branching fraction and CP asymmetries using a data sample of 711 fb^{-1} that contains 771.58 ± 10.57 million $B\overline{B}$ pairs collected on Υ(4S) resonance with the Belle detector at the KEKB asymmetric energy e^+e^- collider. Here h means $\pi^{\pm}$, $K^{\pm}$ and K_S^0. And η is selected in $\eta \to \gamma\gamma$ and $\eta \to \pi^+\pi^-\pi^0$ decays.

The evidence of CP asymmetry for $B^{\pm} \to \eta K^{\pm}$ is found with 3.8 σ, and 3.0 σ in $B^{\pm} \to \eta\pi^{\pm}$ CP asymmetry. The branching fraction of $B^0 \to \eta K^0$ is observed with 5.4 σ standard deviation from zero.

Contents

List of Figures

List of Tables

Chapter 1

Prologue

1.1 Standard Model

The Standard Model of particle physics (SM) [15] is a theoretical picture concerning the electroweak, electromagnetic, and strong interactions. The elementary particles are separated into four families, namely the quarks, leptons, gauge bosons and other bosons(Higgs boson). Quarks and leptons consist of six particles, split into three generations, And with the first generation being the lightest, and the third the heaviest in quarks and charged leptons. Furthermore, gauge bosons are force carrying mediators in the three interactions.

The dynamics in Standard Model depend on 28 parameters, whose numerical values are established by experiment. The 28 parameters include 6 leptons mass, 6 quarks mass, 3 CKM mixing angle, 1 CKM CPV phase, 3 gauge coupling constant, 1 QCD vacuum angle, 1 Higgs quadractic coupling, 1 Higgs self-coupling strength, 3 PMNS mixing angle, 1 PMNS Dirac CPV phase, and 2 PMNS Majorana CPV phase .

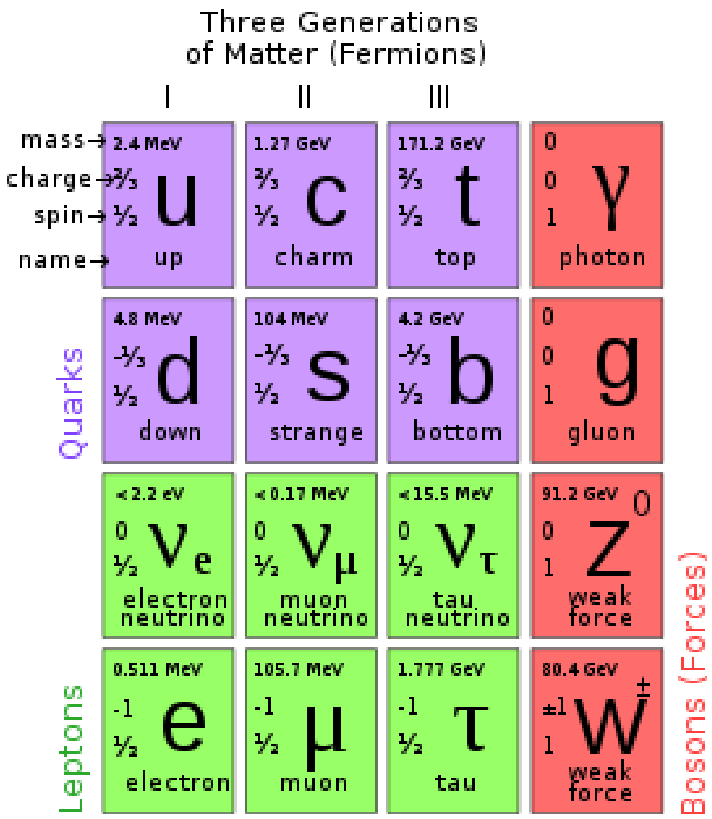

Figure 1.1: The three generation quarks and leptons, with the gauge bosons in the rightmost column.

1.2 CP violation and CKM matrix

Parity(**P**) conservation is believed to be true before C.-S. Wu found the parity violation in the β decay in 1957. After that, people replace parity conservation to charge conjugation and parity (**CP**) conservation. But in 1964, the violation of CP symmetry was found in the decays of neutral K meson system by James Cronin and Val Fitch [18].

In Standard Model weak interaction is the only way that qaurks and leptons can change to anther type. And the flavor changing of quark is described by

$$\begin{pmatrix} d' \\ s' \\ b' \end{pmatrix} = V_{CKM} \begin{pmatrix} d \\ s \\ b \end{pmatrix} = \begin{pmatrix} V_{ud} & V_{us} & V_{ub} \\ V_{cd} & V_{cs} & V_{cb} \\ V_{td} & V_{ts} & V_{tb} \end{pmatrix} \begin{pmatrix} d \\ s \\ b \end{pmatrix} , \tag{1.1}$$

where the 3×3 unitary matrix is called CKM matrix or quark mixing matrix [19]. The CKM matrix can parameterized in several ways, one of the parameterization, called Wolfenstein's parameterization, which transfer the CKM matrix in the form of an expansion in $\lambda = \sin\theta_c$, where θ_c is Cabibbo angle. And Wolfenstein's parameterization has an advantage of giving four parameters in a same order.

$$V_{CKM} = \begin{pmatrix} 1-\frac{\lambda^2}{2} & \lambda & A\lambda^3(\rho - i\eta) \\ -\lambda & 1-\frac{\lambda^2}{2} & A\lambda^2 \\ A\lambda^3(1-\rho-i\eta) & -A\lambda^2 & 1 \end{pmatrix} + O(\lambda^4) , \tag{1.2}$$

1.3 Motivation

Our motivation is to give branching ratios of $B \to \eta h$ decays with about 50% more data compare to the previous measurement in Belle. And in order to rise the significance we also going to 3-D fit instead of 2-D fit.

In SM, η and $\eta^{'}$ quark wave functions are linear combinations of $\frac{u\bar{u}+d\bar{d}}{\sqrt{2}}$ and $s\bar{s}$. It is expected to enhance the $B^{\pm} \to \eta' K^{\pm}$ decay amplitude but suppress the $B^{\pm} \to \eta K^{\pm}$ decay amplitude. Thus, studying $B^{\pm} \to \eta K^{\pm}$ may give us more information in $\eta - \eta^{'}$ mixing and $B(B^{\pm} \to \eta' K^{\pm})$ puzzle. Moreover, interference of different diagrams may provide a large direct CP asymmetry in $B^{\pm} \to \eta K^{\pm}$ and $B^{\pm} \to \eta\pi^{\pm}$. Therefore, the previous BaBar and Belle measurements give a CP asymmetry near to -30% in $B^{\pm} \to \eta K^{\pm}$ decay. It's very interesting and important to confirm the $A_{cp}(\eta K^{\pm})$. And here shows the Feynman diagrams involved in our study.

We report the final updated measurements of branching fractions and partial rate asymmetries for B decays to a pseudoscalar-pseudoscalar mesons with one η meason in the final state. Our decay modes are considered: $\eta(\gamma\gamma)K^{+}$, $\eta(\pi^{+}\pi^{-}\pi^{0})K^{+}$, $\eta(\gamma\gamma)K^{0}$, $\eta(\pi^{+}\pi^{-}\pi^{0})K^{0}$, $\eta(\gamma\gamma)\pi^{+}$, $\eta(\pi^{+}\pi^{-}\pi^{0})\pi^{+}$ The data sample consists of 710 fb^{-1} for data from Exps 7-65, corresponding to 772 million $B\overline{B}$ pairs. Here shows the braching ratios in $B \to \eta h^{\pm}$ decay measured by pervious experiments in PDG.

Table 1.1: The branching ratio in $B \to \eta K^{\pm}$ decay is $2.33^{+0.33}_{-0.34}$ in PDG .

Branching Ratio (10^{-6})	Author	TECN	COMMENT
$2.94^{+0.39}_{-0.34} \pm 0.21$	Aubert	09AV BABR [1]	$e^{+}e^{-} \to \Upsilon(4S)$
$2.21^{+0.48}_{-0.42}(stat)^{\pm 0.25}_{-0.18}(syst)$	Wicht	08 BELL[2]	$e^{+}e^{-} \to \Upsilon(4S)$
$1.9 \pm 0.3^{+0.2}_{-0.1}$	Chang	07B BELL[3]	$e^{+}e^{-} \to \Upsilon(4S)$
$2.2^{+2.8}_{-2.2}$	Richichi	00 CLE2[4]	$e^{+}e^{-} \to \Upsilon(4S)$

Table 1.2: The branching ratio in $B \to \eta\pi^{\pm}$ decay is 4.07 ± 0.32 in PDG .

Branching Ratio (10^{-6})	Author	TECN	COMMENT
$4.00 \pm 0.40 \pm 0.24$	Aubert	09AV BABR	$e^{+}e^{-} \to \Upsilon(4S)$
$4.2 \pm 0.4 \pm 0.2$	Chang	07B BELL	$e^{+}e^{-} \to \Upsilon(4S)$
$1.2^{+2.8}_{-1.2}$	Richichi	00 CLE2	$e^{+}e^{-} \to \Upsilon(4S)$

Table 1.3: The branching ratio in $B \to \eta K_S^0$ decay is $1.15^{+0.43}_{-0.38} \pm 0.09$ in PDG.

Branching Ratio (upper limit) (10^{-6})	Author	TECN	COMMENT
$1.15^{+0.43}_{-0.38} \pm 0.09 (< 1.8)$	Aubert	09AV BABR	$e^+e^- \to \Upsilon(4S)$
(< 1.9) [not used in PDG]	Chang	07B BELL	$e^+e^- \to \Upsilon(4S)$

Table 1.4: The branching ratio in η decay [PDG].

Decay mode	Branching Ratio (%)
$2\ \gamma$	39.31 ± 0.20
$\pi^+\ \pi^-\ \pi^0$	22.74 ± 0.28

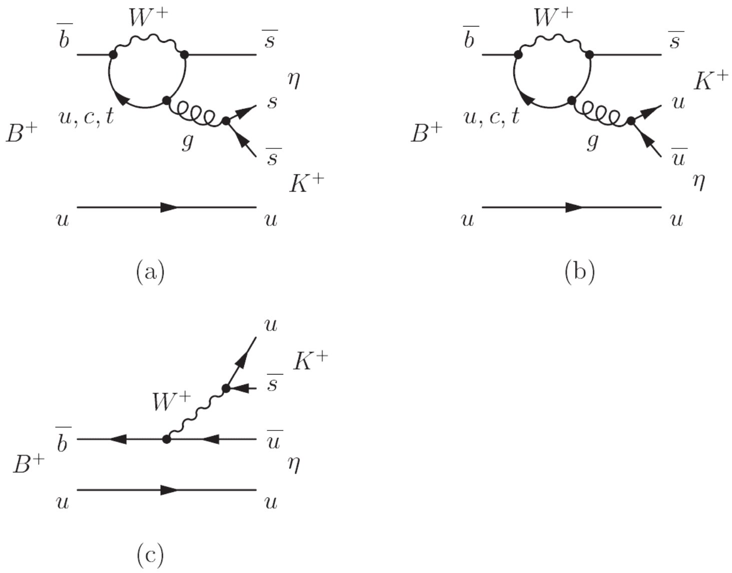

Figure 1.2: Examples of Feynman diagrams involved in $B^\pm \to \eta K^\pm$ decay.

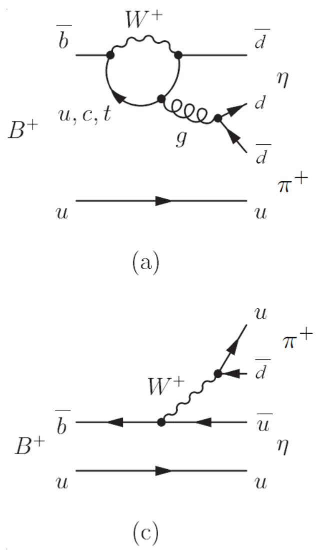

Figure 1.3: Examples of Feynman diagrams involved in $B^{\pm} \to \eta\pi^{\pm}$ decay.

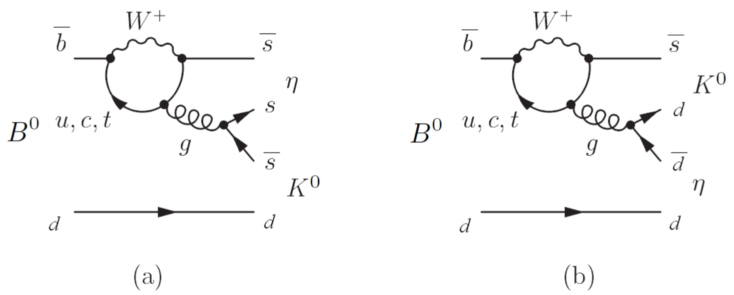

Figure 1.4: Examples of Feynman diagrams involved in $B^{\pm} \to \eta K^0_S$ decay.

Chapter 2

KEK B-Factory

The KEK B-Factory (KEKB) [22] is an e^+-e^- collider which located at the High Energy Accelerator Research Organization (KEK) in Tsukuba area, Ibaraki Prefecture, Japan. The construction of KEKB accelerator and detector started in April 1994. Operatoin was started at Dec. 1998 and truned off at June 30 2010. It's main goal is to search for signatures of physics beyond the standard model through high-sensitivity measurements. It also presents the measurements of CP asymmetry in B meson decays. The results of KEKB agree the prediction of KM model [19], and provided a strong experimental support for M. Kobayashi and T. Maskawa to win the 2008 Nobel Prize in Physics [24].

2.1 KEKB Accelerator

The KEKB accelerator is an two-rings, asymmetric, e^+-e^- collider. Which is based on the existing TRISTAN tunnel of 3 km circumference to construct the high energy ring (HER) and low energy ring (LER). The HER stores e^- and the LER stores e^+. The energy of e^+ and e^- is 3.5 and 8 GeV, and provide the center-of-mass energy of e^+-e^- beams at the $\Upsilon(4S)$ resonance, and large number of B meson pairs can be produce via $e^+e^- \to \Upsilon(4S) \to B\overline{B}$.

In KEKB accelerator electrons and positrons beam collide at a crossing angle of ± 11 mrad at the center of the BELLE detector. It not only allows superconducting RF cavity to be filled within the beam but also avoid parasitic collisions. The crossing angle also eliminate the need of the separation-bend magnets and reduces beam-related backgrounds in BELLE detector.

The main parameters of KEKB are summarized in Table 2.1, and Figure 2.1 shows the configuration of the accelerator.

Table 2.1: The parameters of the KEKB accelerator.

Ring		LER	HER	Unit
Energy	E	3.5	8.0	GeV
Circumference	C	3016.26		m
Luminosity	L	1×10^{34}		$\mathrm{cm}^{-2}\mathrm{s}^{-1}$
Crossing angle	θ_x	± 11		mrad
Tune shifts	ξ_x/ξ_y	0.039/0.052		
Beta function at IP	β_x^*/β_y^*	0.33/0.01		m
Beam current	I	2.6	1.1	A
Natural bunch length	σ_z	0.4		cm
Energy spread	σ_ε	7.1×10^{-4}	6.7×10^{-4}	
Bunch spacing	s_b	0.59		m
Particles/bunch	N	3.3×10^{10}	1.4×10^{10}	
Emittance	$\varepsilon_x/\varepsilon_y$	$1.8 \times 10^{-8}/3.6 \times 10^{-10}$		
Synchrotron	ν_s	$0.01 \sim 0.02$		
Betatron tune	ν_x/ν_y	45.52/45.08	47.52/43.08	
Momentum compaction factor	α_p	$1 \times 10^{-4} \sim 2 \times 10^{-4}$		
Energy loss/turn	U_0	$0.81^{\dagger}/1.5^{\dagger\dagger}$	3.5	MeV
RF voltage	V_c	$5 \sim 10$	$10 \sim 20$	MV
RF frequency	f_{RF}	508.887		MHz
Harmonic number	h	5120		
Longitudinal damping time	τ_ε	$43^{\dagger}/23^{\dagger\dagger}$	23	ms
Total beam power	P_b	$2.7^{\dagger}/4.5^{\dagger\dagger}$	4.0	MW
Radiation power	P_{SR}	$2.1^{\dagger}/4.0^{\dagger\dagger}$	3.8	MW
HOM power	P_{HOM}	0.57	0.15	MW
Bending radius	ρ	16.3	104.5	m
Length of bending magnet	l_B	0.915	5.86	m

†: without wigglers, ††: with wigglers

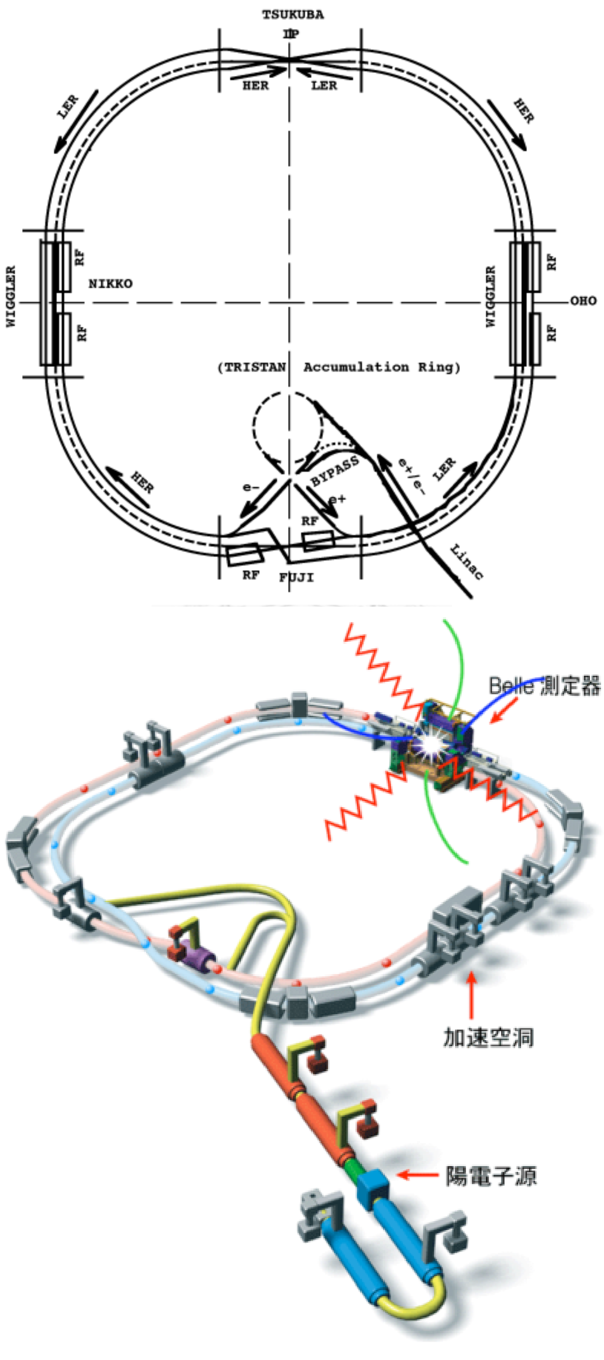

Figure 2.1: Schematic layout of KEKB from the top and side view.

2.2 Belle Detector

The Belle detector [25] is a collection of sub-detectors built around the interaction point of the KEKB accelerator. The coordinate system of the Belle detector is defined with the z-axis antiparallel to the e^+ beam and the x-axias pointing inward, toward the center of the KEKB storage rings. It is often to use polar corrdinates(θ, ϕ,and r) with polar angle θ defined as the angle away from the z-axis. The Belle detector subsystems cover a full 2π in ϕ and three ranges in polar angle θ: the barrel region ($34° < \theta < 127°$), the forward endcap ($17° < \theta < 34°$), and the backward endcap($127° < \theta < 150°$). Table 2.2 summarize the performance of the Belle detector and its sub-detectors, and Figure 2.2 shows the configuration of them in isometric and side view.

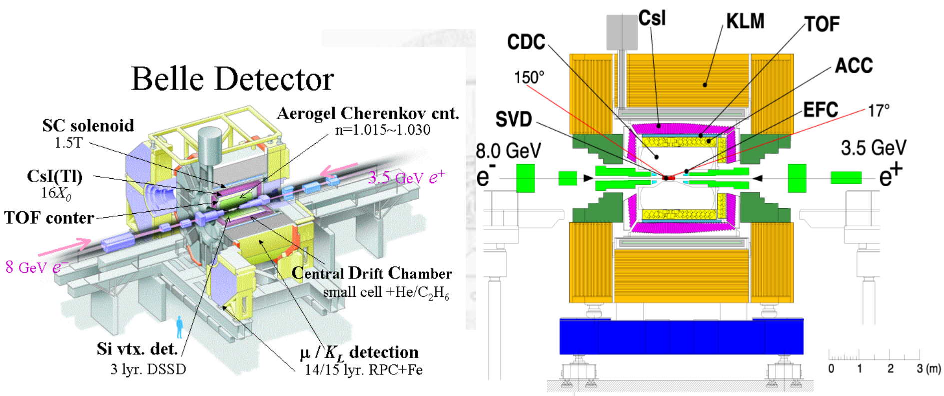

Figure 2.2: The structure of the Belle detector in isometric and side view. [26].

2.2.1 Beam Pipe

Since the multiple Coulomb scattering could affects the track resolution, it is important to minimise the impact of the beampipe on particle trajectories with a thin material(low atomic number). So a beryllium beampipe was installed in the Belle Detector. The beam pipe is a dual layer cylinder with radii 20.0 mm and 23.0 mm, which thickness are 0.5 mm. The gap between these two beryllium walls provides a channel for helium gas, which is used as a coolant. In 2003, the original beampipe was replaced by a new one which

Table 2.2: The detail of each sub-detector in the Belle detector.

Detector	Type	Configuration	Readout	Performance
Beam pipe DS-I	Beryllium double wall	Cylindrical, r = 20mm, 0.5/2.5/0.5(mm) = Be/He/Be w/ He gas cooled		
Beam pipe DS-II	Beryllium double wall	Cylindrical, r = 15mm, 0.5/2.5/0.5(mm) = Be/PF200/Be		
EFC	BGO	Photodiode readout Segmentation : 32 in ϕ; 5 in θ	160×2	Rms energy resolution: 7.3% at 8 GeV 5.8% at 2.5 GeV
SVD1	Double-sided Si strip	3-layers: 8/10/14 ladders Strip pitch: 25(p)/50(n)μm	ϕ: 40.96k z: 40.96k	$\sigma(z_{CP}) \sim 78.0\mu$m for $B \to \phi K_s^0$
SVD2	Double-sided Si strip	4-layers: 6/12/18/18 ladders Strip pitch: 75(p)/50(n)μm (layer1-3) 73(p)/65(n)μm (layer4)	ϕ: 55.29k z: 55.296k	$\sigma(z_{CP}) \sim 78.9\mu$m for $B \to \phi K_s^0$
CDC	Small cell drift chamber	Anode: 50 layers Cathode: 3 layers r = 8.3 - 86.3 cm $-77 \leq z \leq 160$ cm	Anode: 8.4k Cathod: 1.8k	$\sigma_{r\phi} = 130\mu$m $\sigma_z = 200 \sim 1400\mu$m $\sigma_{Pt}/Pt = 0.3\%\sqrt{p_t^2+1}$ $\sigma_{dE/dx} = 0.6\%$
ACC	Silica aerogel	960 barrel/228 end-cap FM-PMT readout		$N_{p.e.} \geq 6$ K/π seperation: $1.2 < p < 3.5$GeV/c
TOF	Scintillator	128 ϕ segmentation r = 120 cm, 3-cm long	128×2	$\sigma_t = 100$ ps K/π seperation:
TSC		64 ϕ segmentation	64	up to 1.2 GeV/c
ECL	CsI (Towered-structure)	Barrel: r = 125 - 162 cm End-cap: z = -102 cm and +196cm	6624 1152(F) 960(B)	$\sigma_E/E = 1.3\%/\sqrt{E}$ $\sigma_{pos} = 0.5$ cm$/\sqrt{E}$ (E in GeV)
KLM	Resistive plate counters	14 layers (5 cm Fe + 4cm gap) 2 RPCs in each gap	θ: 16k ϕ: 16k	$\Delta\phi = \Delta\theta = 30$mr for K_L $\sim 1\%$ hadron fake
Magnet	Supercon.	Inner radius = 170 cm		B=1.5T

inner radius is 15.0 mm. The cross-section of the beam pipe is shown in Figure 2.3. The arrangment of the beam pipe and these masks are in Figure 2.4.

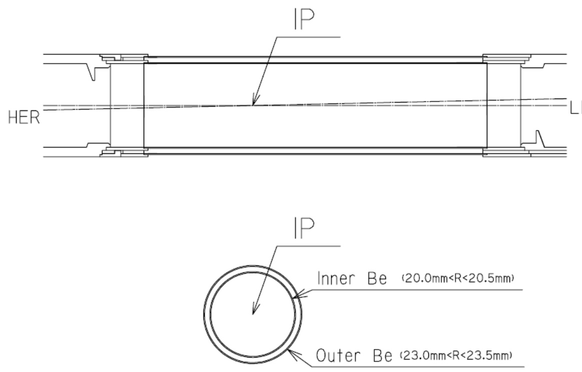

Figure 2.3: The cross-section of the beam pipe at the IP [25].

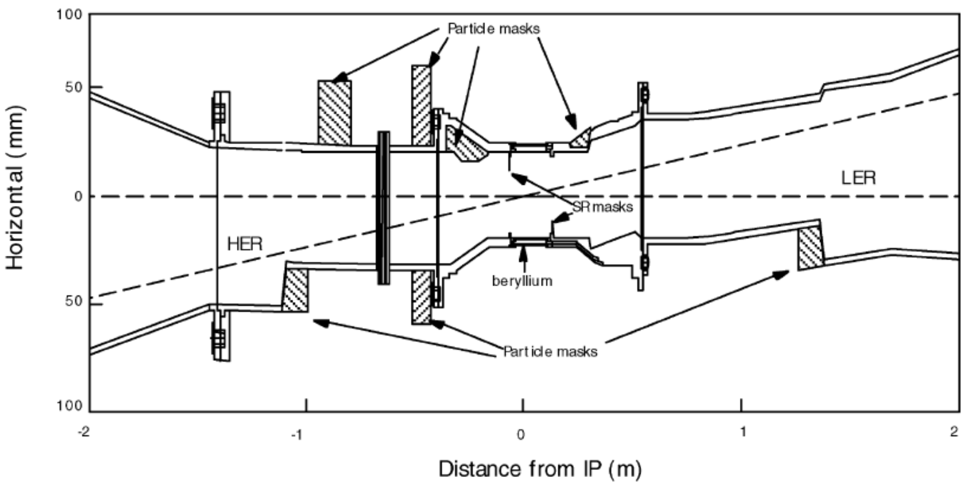

Figure 2.4: The structure of the beam pipe and horizontal masks [25].

2.2.2 Silicon Vertex Detector (SVD)

The primary goal of the SVD is to measure the B meson decay vertex, which is essential for time-dependent CPV study. SVD1 was a three layers Double-sided Silicon Detector($DSSD$) in a barrel-only design($23° < \theta < 139°$), comprising of 8, 10, and 14 ladders in the inner, middle, and outer layers, respectively. Each ladder is constructed from two joined half-ladders. In summer 2003, the SVD 2 was replaced by a new SVD system (SVD 2). The SVD 2 consists four layers consisting of 6, 12, 18, and 18 ladders from the innermost layer, respectively. And covers more percentage of full solid angle then SVD I ($17° < \theta < 150°$).

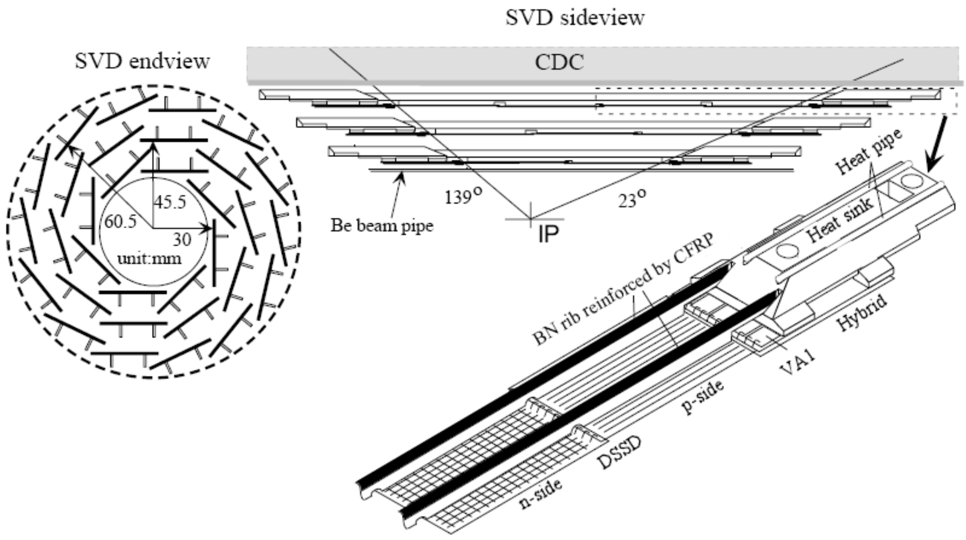

Figure 2.5: Configuration of SVD [25].

2.2.3 Extreme Forward Calorimeter (EFC)

The Extreme Forward Calorimeter (EFC) extend the polar angle coverage in both extreme forward and backward regions ($6.4° < \theta < 11.5°$ and $163.3° < \theta < 171.2°$) which do not cover by ECL. It is useful to improve the experimental sensitivity in some special decay channels such as $B \to \tau\nu$ decay. The main material of EFC is the radiation-hard BGO (Bismuth Germanate, $Bi_4Ge_3O_12$) crystal calorimeter due to their higher radiation tolerance.

In fact, the EFC has never been used in decay reconstruction. However, its geometric location allows it to act as a beam mask to reduce radiation backgrounds to the CDC. In addition, EFC is used for online luminosity and background monitoring. The structure of the cone-like EFC are shown in Fig. 2.6.

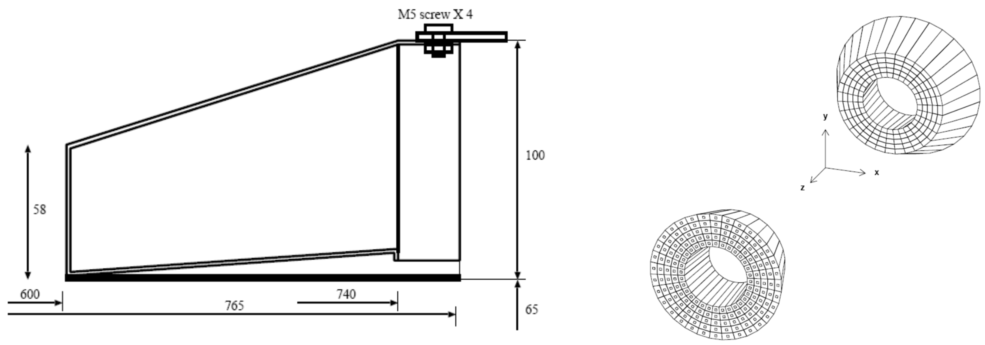

Figure 2.6: Side view of forward EFC (left) and isometric view of the forward and backward EFC detectors (right) [25].

2.2.4 Central Drift Chamber (CDC)

The Central Drift Chamber (CDC) with inner(outer) radius 103.5(874) mm and covers the angular range from $17° < \theta < 150°$. The CDC has a total of a total of 8400 drift cells placed on 50 cylindrical layers. Each of its 8400 drift cells consists of a sense wire, held at a high voltage(2.35 kV), surrounded by field wires, held at low voltage. The CDC is filled with a 50% helium, 50% ethane (C_2H_6) mixture.The configuration of CDC can be seen in Fig. 2.7. The CDC is used to provide the information of momentum and dE/dx (for particle identification) from charged particles. Charged particles passing through the gas ionize electrons, and the ionized electrons drift forwards to the sense wire. Therefore, the track information is collected.

The particle transverse momentum can be determined from the curvature of the helix(r) as $p_T = 0.3$Br, where p_T is in units of GeV/c, B is the magnetic field in Tesla, and r is in meters. More details of CDC are summarized in Table 2.3, and the configuration of CDC drift cells are shown in Fig. 2.8.

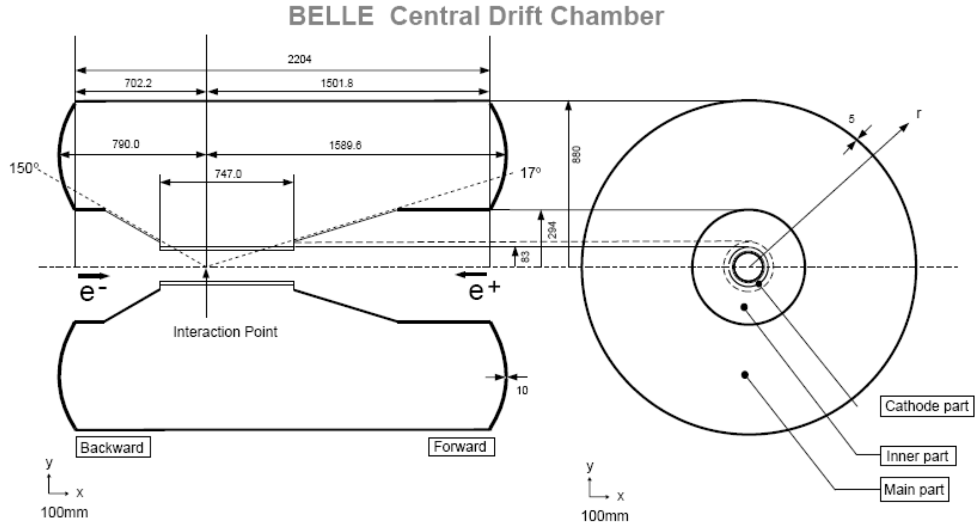

Figure 2.7: Overview of CDC structure [25]. The lengths in the figure are in units of mm.

2.2.5 Aerogel Cherenkov counter system (ACC)

The Aerogel Cherenkov counter (ACC) is used to provide particle identification information to distinguish $K^{\pm}$ from $\pi^{\pm}$ in high monmentum range (1.2 GeV/$c \sim$ 4.0 GeV/c) by Cherenkov radiation. Cerenkov radiation is emitted if the velocity of a charged particle exceeds the speed of light in medium, $n > \frac{1}{\beta} = \sqrt{1 + (\frac{m}{p})^2}$, where m and p are the mass and momentum of the charged particle, and n is the refractive index of the material. Therefore, it is possible to distinguish kaons from pions by selecting a material in which pions will emit Cherenkov light, but kaons will not.

The ACC can be separated into barrel and forward end-cap part. The barrel part is consists of 960 counter modules, and 228 in the end-cap part. The counter module is a thin aluminum box containing two principal components: a stack of ultralight aerogel with index of refraction (n = 1.010, 1.013, 1.015, 1.020, 1.028 and 1.030), and one or two fine mesh photomultipler tubes (PMTs) to detect Cherenkov light. Figure 2.10 shows the configuration of ACC, and Figure 2.11 shows the counter module in the barrel and end-cap

Table 2.3: Configuration of the CDC sense wire and cathode strips [25].

Superlayer type	No. of layers	Channels per layer	Radius (mm)	Stereo angle (mrad) [strip pitch (mm)]
Cathode	1	$64(z)\times8(\phi)$	83.0	[8.2]
Axial 1	2	64	88.0−98.0	0.
Cathode	1	$80(z)\times8(\phi)$	103.0	[8.2]
Cathode	1	$80(z)\times8(\phi)$	103.5	[8.2]
Axial 1	4	64	108.5−159.5	0.
Stereo 2	3	80	178.5−209.5	71.46−73.75
Axial 3	6	96	224.5−304.0	0.
Stereo 4	3	128	322.5−353.5	-42.28−-45.80
Axial 5	5	144	368.5−431.5	0.
Stereo 6	4	160	450.5−497.5	45.11−49.36
Axial 7	5	192	512.5−575.5	0.
Stereo 8	4	208	594.5−641.5	-52.68−-57.01
Axial 9	5	240	656.5−719.5	0.
Stereo 10	4	256	738.5−785.5	62.10−67.09
Axial 11	5	288	800.5−863.0	0.

parts.

2.2.6 Time-of-Flight Counters (TOF)

The Time of Flight Counter (TOF) provide particle identification information to distinguish charged kaons from pions in the low momentum region(less then 1.2 GeV/c).

The TOF covers the agnle range region of $34^\circ < \theta < 120^\circ$, and it consists of 128 TOF counters and 64 trigger scintillation counters (TSC). One TOF/TSC modules is consists of two trapezoidally shaped TOF and one TSC counters. Signals could be read by fine-mesh-dynode photomultiplier tubes (FM-PMT) which is mounted directly on the TOF and TSC scintillation counters and placed in a magnetic field of 1:5 T. Figure 2.12 shows a TOF/TSC module geometry..

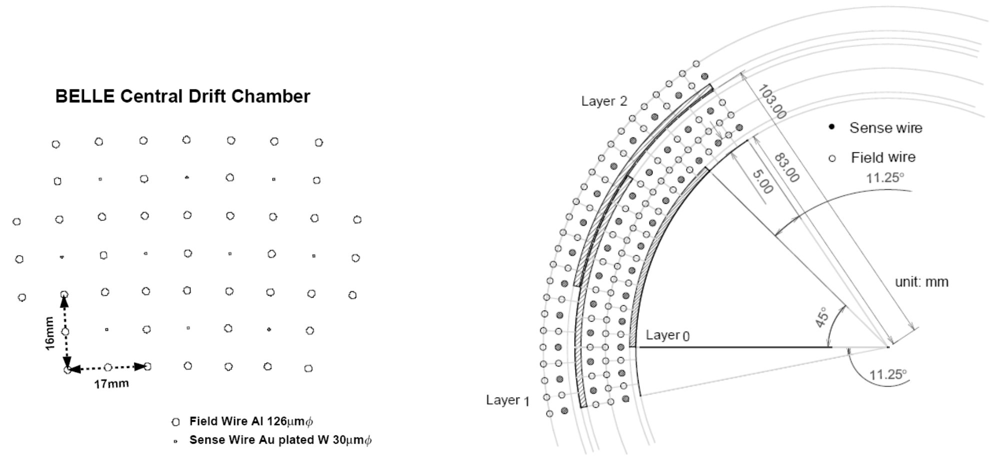

Figure 2.8: Cell structure (left) and the cathode sector configuration (right) [25].

In TOF, the mass m of the charged particle is calculated from the following formula:

$$M_{track}^2 = \left(\frac{1}{\beta^2} - 1\right) P^2 = \left(\left(\frac{cT_{obs}^{twc}}{L_{path}}\right)^2 - 1\right) P^2 \ , \tag{2.1}$$

where T_{obs}^{twc} is the time walk correction on the measured FM-PMT signal time to get a precise observed time, and $L_{path}(P)$ stands for the path length (momentum) obtained from the CDC track. Fig. 2.13 shows the mass distribution for momenta below 1.2 GeV/c.

For each charged track, the CDC, ACC and TOF information are are combined to give a likelihood ratio to the particle identification, mainly for the separation of protons/kaons/pions. Fig. 2.14 shows a plot that indicate the regions in which they work well in distinguishing charged particles.

2.2.7 Electromagnetic Calorimeter (ECL)

The Electromagnetic Calorimeter (ECL) is mainly used to detect the energy and position of photons from B meson decays by measuring electromagnetic

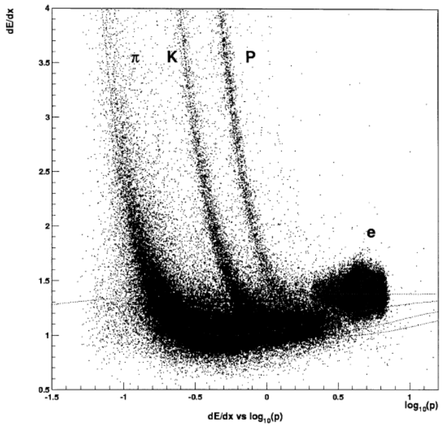

Figure 2.9: The plot of dE/dx and particle momentum, together with the expected truncated mean [25].

showers. And the photons momentum could be caluate with the photons' mother's decay point or IP. Combining the ECL information and dE/dx information in CDC and light yield in ACC, the ECL can also provide nice electron idnetification. Figure 2.15 shows the configuration of ECL.

High energy incident electron or photon causes an electromagnetic shower when interacting with a material. If the material is doped with a fluor, the ionization energy losses from the shower are converted into visible light, which can be measured by a photodetector. Thus, cesium iodide crystals, doped with thallium as a fluor (CsI(Tl)), are chosen. The ECL consists of 8,736 CsI(Tl) crystals shaped in a half-tower and point to the IP. The size of crystals range from 55 × 55 mm^2 (front face) and 82 × 82 mm^2 (rear face) for barrel part, and vary from 44.5 to 70.8 mm and from 54 to 82 mm, respectively in end-cap part. The length of each crystal is chosen to be 30 cm ($16.2X_0$). The whole ECL is comprised of a barrel section with 3m in length and 1.25m inner radius. And cover the polar angle region of $17° < \theta < 150°$, the total covred solid-angle is 91% of 4π, other details of ECL can be seen in Table 2.4.

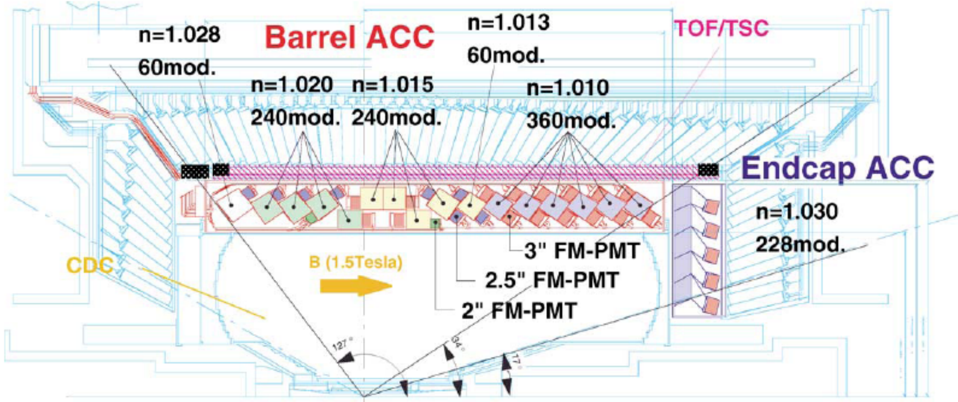

Figure 2.10: The arrangement of ACC in the Belle detector [25].

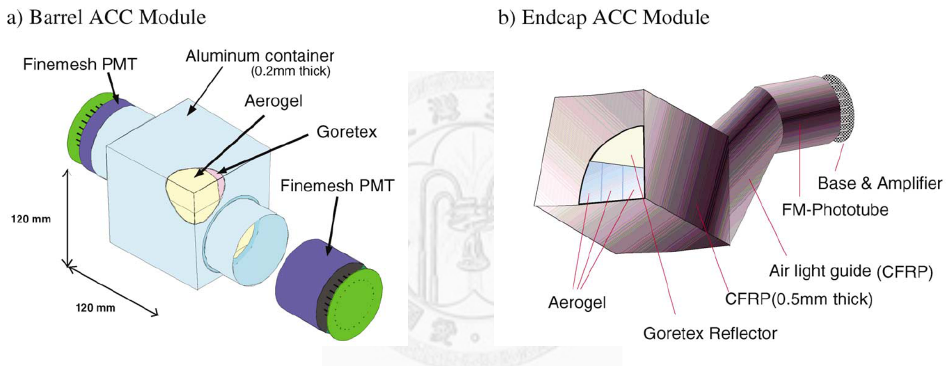

Figure 2.11: Schematic drawing of a typical ACC counter module: (a) barrel and (b) end-cap ACC [25].

2.2.8 K$_L$ and Muon Detector (KLM)

The K$_L$ and Muon Detector (KLM), which covering the polar angle region from 20° to 155°, is located outside the solenoid and designed to detect K_L^0 and $\mu^\pm$ particle with enough momentum to reach the KLM, $P > 0.6GeV/c$. The KLM consists of 15 (14) layers of glass-electrode-resistive plate counters (RPCs) and 14 (14) layers of 4.7 cm-thick iron plates in the octagonal barrel region (the forward and backword end-caps). Those multiple layers of charged particle detectors and iron allow discrimination between muons and charged hadrons ($\pi^\pm, K^\pm$) based upon their range and transverse scattering.

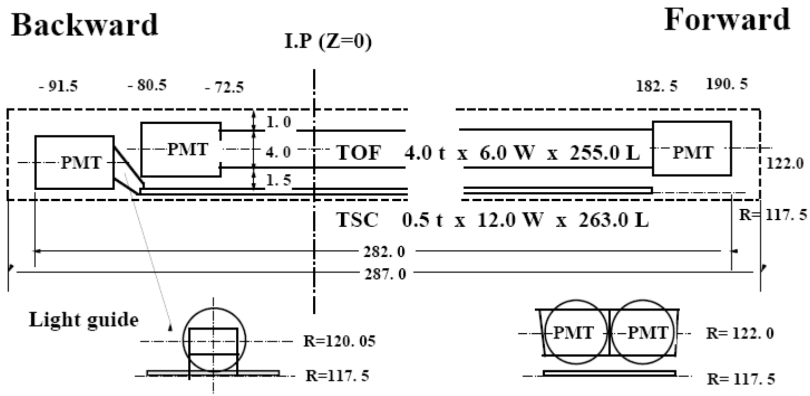

Fig. 54. Dimensions of a TOF/TSC module.

Figure 2.12: A TOF/TSC module [25].

Table 2.4: Parameters of ECL [25].

Item	θ coverage	θ seg.	ϕ seg.	No. of crystals
Forward end-cap	$12.4^\circ - 31.4^\circ$	13	48−144	1152
Barrel	$32.2^\circ - 128.7^\circ$	46	144	6624
Backward end-cap	$130.7^\circ - 155.1^\circ$	10	64−144	960

Muons travel much farther with smaller deflections than strongly interacting hadrons. K_L will deposit most of energy in the iron of the KLM proper. And K_L candidate can be distinguished from another charged hadron because K_L never leave any associated track in the CDC. We can also get the position information of K_L by measuring the showers. However, the KLM detector can not measure K_L energy well. Other details can be seen in Figure 2.17. Figure 2.16 shows the cross section of a KLM super-layer.

2.2.9 Solenoid Magnet

In the Belle detector, charged particles are bent in a helix from which track momentum can be measured in the CDC. The bend is given by a superconducting solenoid magnet which provides a magnetic field of 1.5 T parallel

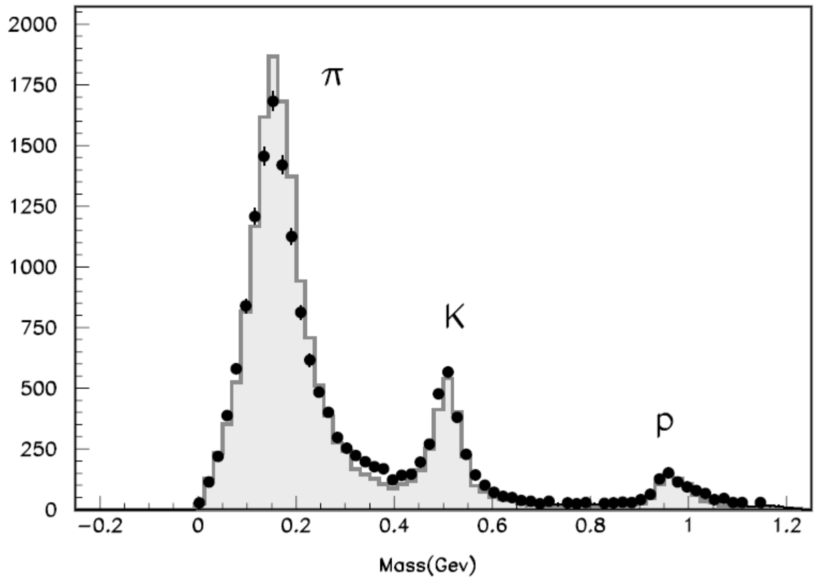

Figure 2.13: Mass distribution from TOF for particle momenta below 1.2 GeV/c [25].

to the beam pipe in a cylindrical volume of 3.4 m in diameter and 4.4 m in length. And it's cooling system is based on liquid helium which is circulating through a tube on the inner surface of the cylinder.

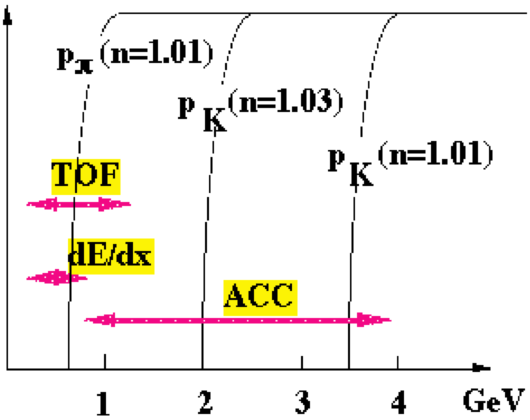

Figure 2.14: The CDC, ACC and TOF are useful for particle identification in different momentum region [26].

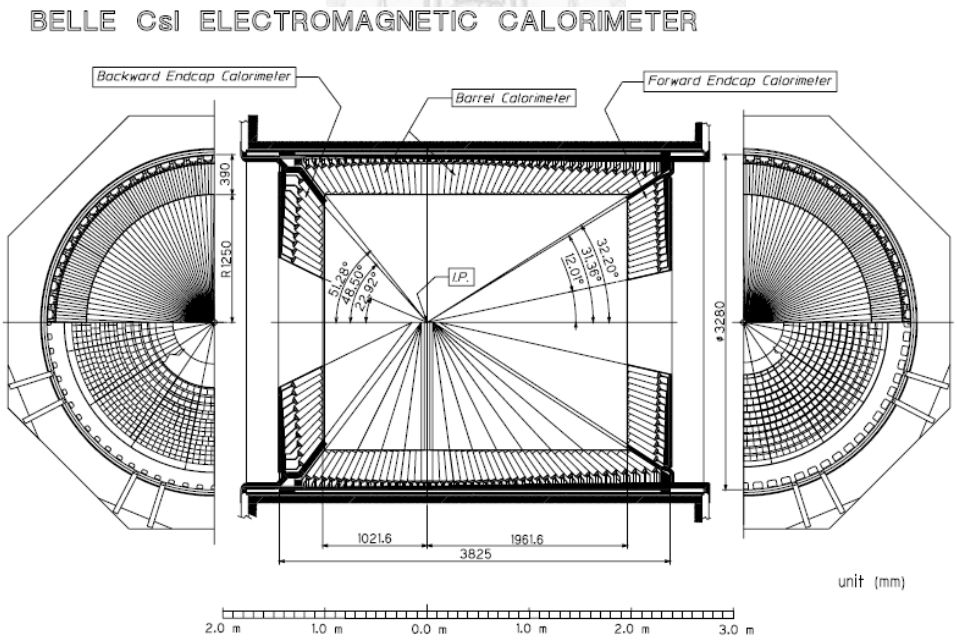

Figure 2.15: Configuration of ECL [25].

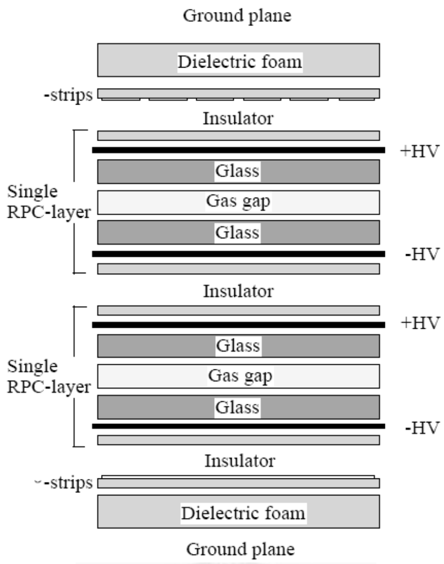

Figure 2.16: Cross-section of a KLM superlayer [25].

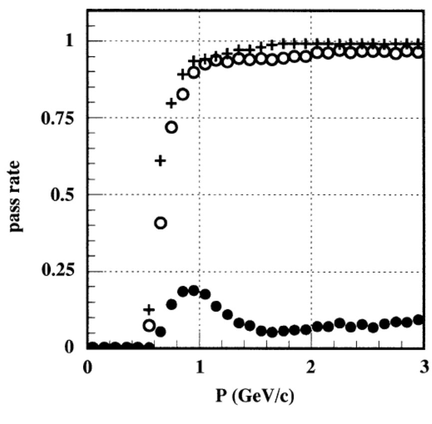

Figure 2.17: Pass rate of the muon preselection (primary requirement is two associated KLM hits at least) for muons (open circle) and pions (closed circle) within $23^{\circ} < \theta < 150^{\circ}$. The crosse are for muons with one hits at least [27].

Chapter 3

Basic Selection and and B Reconstruction

3.1 Introduction

3.2 Reconstruction and Event Selection

Candidate η mesons are reconstructed in the decay modes: $\eta \to \gamma\gamma$ and $\eta \to \pi^+\pi^-\pi^0$. In the $\eta \to \gamma\gamma$ reconstruction, the energy of the photons forming the η is required to be greater than 50 MeV and the energy asymmetry, $|E_{\gamma 1} - E_{\gamma 2}|/(E_{\gamma 1} + E_{\gamma 2})$, is required to be less than 0.9 to reject soft photon background. We remove η candidates if either of the daughter photons can be combined with any other photon with $E_\gamma >$100 MeV to form a π^0 candidate. As to $\eta \to \pi^+\pi^-\pi^0$, candidate π^0 is chosen from the Mdst_π^0 bank with photon energy above 50 MeV. We require the recontructed π^0 mass to be within 115 MeV/c^2 and 155 MeV/c^2 in this analysis.

And Clear η mass peak can be seen in both $\gamma\gamma$ and $\pi^+\pi^-\pi^0$ decay modes. The final η candidates are selected by requiring the mass windows cuts: 501$< M_\eta <$573 MeV/c^2 for $\eta \to \gamma\gamma$ and 538.5$< M_\eta <$556.5 MeV/c^2 for $\eta \to \pi^+\pi^-\pi^0$ as indicated by the arrows. Then each η candidate is constrained to the nominal η mass (547.9 MeV/c^2) and two charged pions in $\eta \to \pi^+\pi^-\pi^0$ are constrained to run through interacton point (IP).

Charged particles directly from B and η decays are required to come from the IP, $\Delta r < 0.3$ cm and $\Delta z < 3.0$ cm. Charged kaons and pions are distinguished using the standard atc_pid$(3, 1, 5, K/\pi) > 0.6$ are indentified as kaons and atc_pid$(3, 1, 5, K/\pi) < 0.4$ as pions. Tracks that are highly electron like ($e\_id > 0.95$) or muon like ($\mu\_id > 0.95$) are rejected in this analysis. Candidates K_S^0 are selected using the good_K_S^0 module [5],and K_S^0 mass windows cuts 488< $M_{K_S^0}$ <508 MeV/c^2 is required.

B signals are identified using the beam constrained mass which is difined by M_{bc}=$\sqrt{E_{beam}^2 - (\overrightarrow{P_h} + \frac{\overrightarrow{P_\eta}}{|P_\eta|}\sqrt{(E_{beam} - E_h)^2 - M_\eta})^2}$ [Appendix C], and energy difference $\Delta E = E_{recon} - E_{beam}$ computed in the $\Upsilon(4S)$ CM frame. Here $E_{beam}, E_{recon}$and P_h are the beam energy,the reconstructed energy and the $K^\pm, \pi^\pm$ or K_S^0 momentum of the signal candidate, respectively. And M_η is equal to 0.547853 GeV/c^2. The M_{bc} resloution is $\sim$ 3MeV/c^2, which is dominated by the beam energy spread of KEKB. The ΔE resolution is mode dependent, which is wider for the $\gamma\gamma$ mode and narrower for the $\pi^+\pi^-\pi^0$ mode. Events with M_{bc} >5.2 GeV/c^2 and $|\Delta E|$ <0.3 GeV are selected in sample box. And we choose $5.27 < M_{bc} < 5.29$ GeV/c^2, $-0.15 < \Delta E < 0.1$ GeV as a signal box in $B \to \eta(\gamma\gamma)h$ mode. And $5.27 < M_{bc} < 5.29$ GeV/c^2, $-0.1 < \Delta E < 0.08$ GeV in $B \to \eta(\pi^+\pi^-\pi^0)h$ mode.

Table 3.1: Summary of particle selection criteria

Particle	Requirement
$\eta(\gamma\gamma)$	$E_\gamma > 50MeV$ $\frac{\lvert E_{\gamma 1}-E_{\gamma 2}\rvert}{(E_{\gamma 1}+E_{\gamma 2})} < 0.9$ π^0 veto $501 < M_\eta < 573$ MeV/c^2
$\eta(\pi^+\pi^-\pi^0)$	$E_\gamma > 50MeV$ in π^0 reconstruction $\lvert cos\theta_{hel}(\pi^0)\rvert < 0.95$ in π^0 reconstruction $115 < M_{\pi^0} < 152$ MeV/c^2 $\lvert\Delta r\rvert < 0.3$ cm for charged pion $\lvert\Delta z\rvert < 3$ cm for charged pion $\L_{K,\pi} < 0.6$ for charged pion $EID < 0.95$ for charged pion $\mu ID < 0.95$ for charged pion $538.5 < M_\eta < 556.5$ MeV/c^2
K^0_S	Applied $goodK_S$ selection 488$< M_{K^0_S} <$508 MeV/c^2
$h^\pm$ in $B^\pm \to \eta h^\pm$	$\lvert\Delta r\rvert < 0.3$ cm $\lvert\Delta z\rvert < 3$ cm $\L_{K,\pi} < 0.4$ for $\pi^\pm$ $\L_{K,\pi} > 0.6$ for $K^\pm$ $EID < 0.95$ $\mu ID < 0.95$

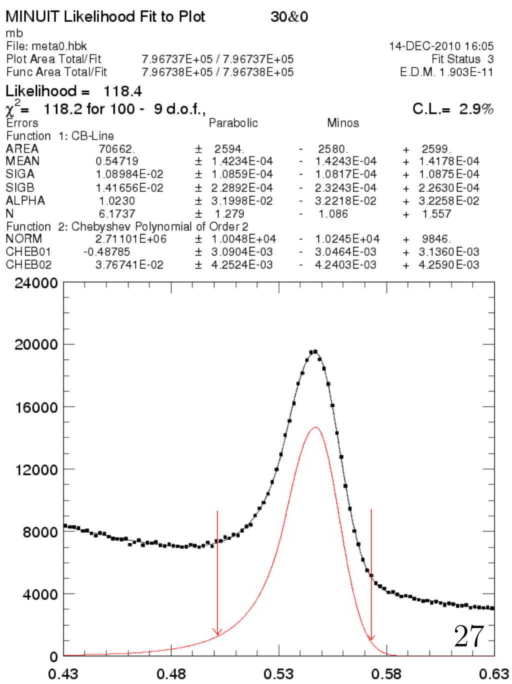

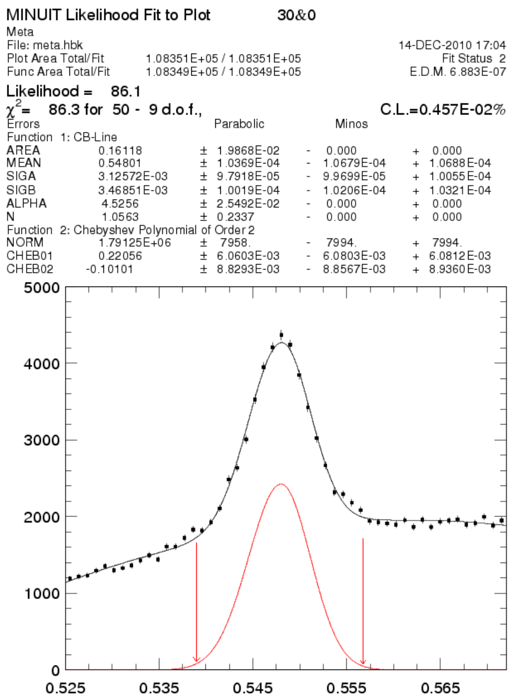

Figure 1.1.1: Invariant mass distribution of $\eta \to \gamma\gamma$ ($left$) and $\eta \to \pi^+\pi^-\pi^0$ ($right$) in data sample.

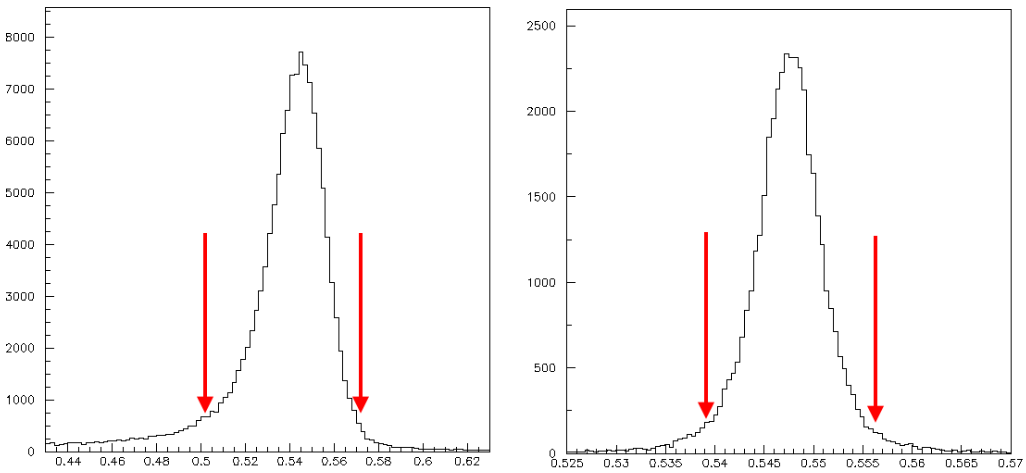

Figure 1.1.2: Invariant mass distribution of $\eta \to \gamma\gamma$ ($left$) and $\eta \to \pi^+\pi^-\pi^0$ ($right$) in signal MC without true events selection.

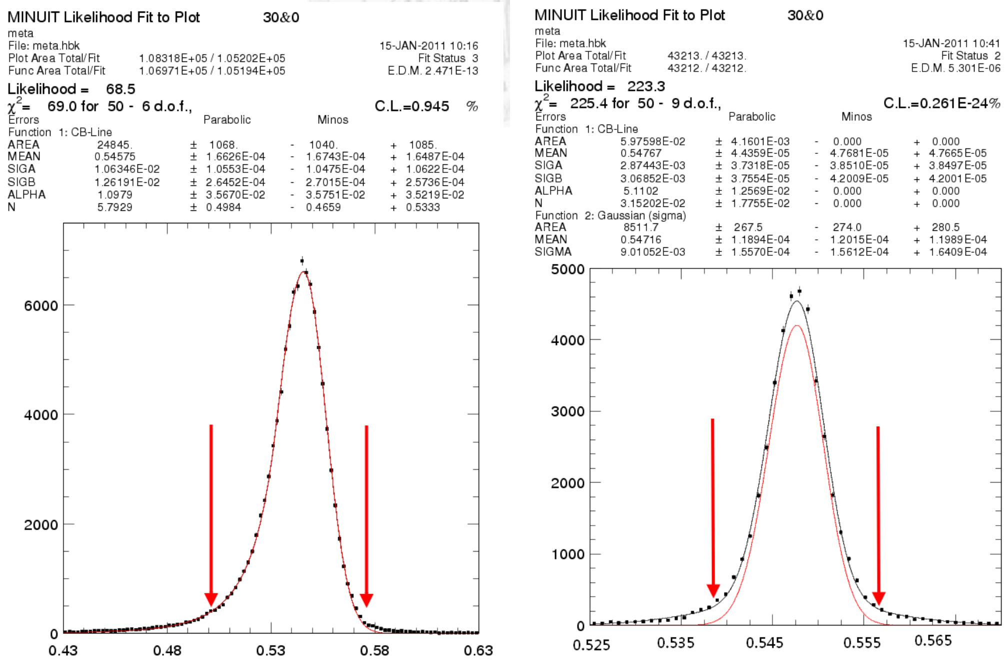

Figure 1.1.3: Invariant mass distribution of $\eta \to \gamma\gamma$ ($left$) and $\eta \to$

$\pi^+\pi^-\pi^0$ (*right*) in signal MC with true events selection.

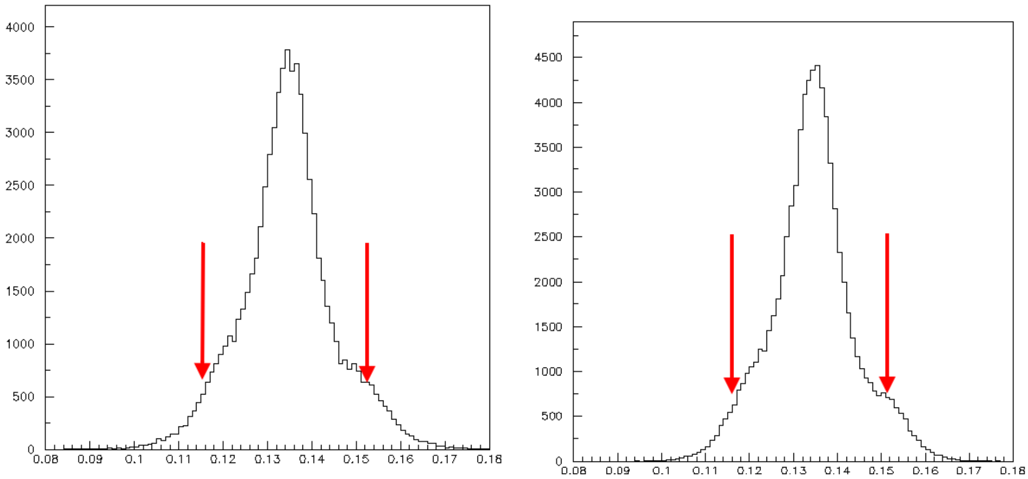

Figure 1.2.1: Invariant mass distribution of π^0 candidates in data (*left*) and signal MC (*right*) sample without true events selection.

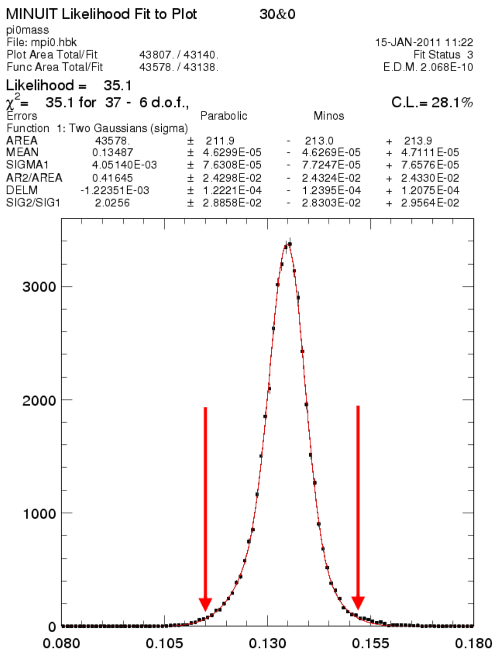

Figure 1.2.2: Invariant mass distribution of π^0 candidates in signal MC sample with true events selection.

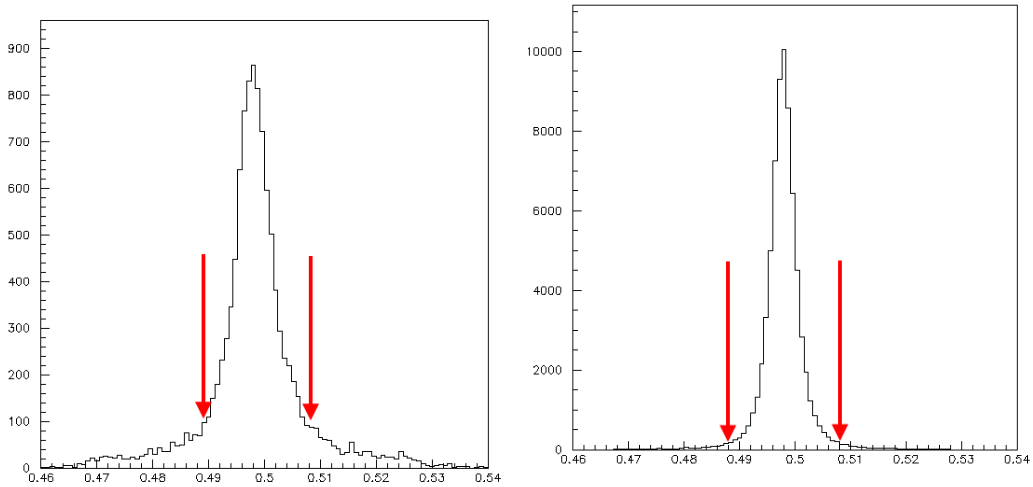

Figure 1.3.1: Invariant mass distribution of K_S^0 candidates in data ($left$) and signal MC ($right$) sample without true events selection.

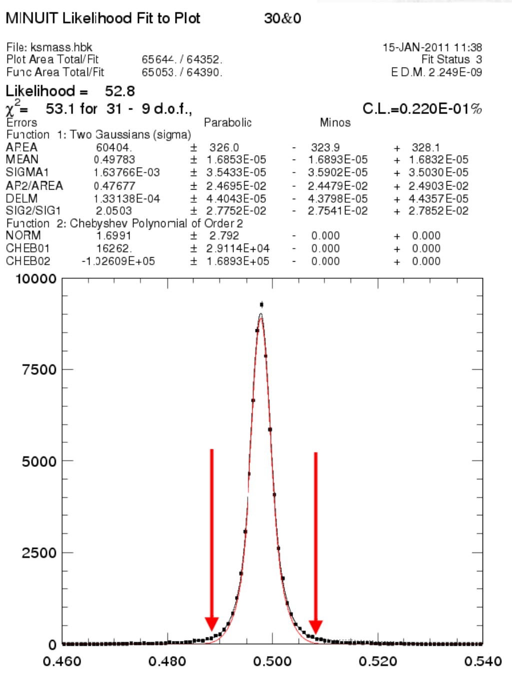

Figure 1.3.2: Invariant mass distribution of K_S^0 candidates in signal MC sample with true events selection.

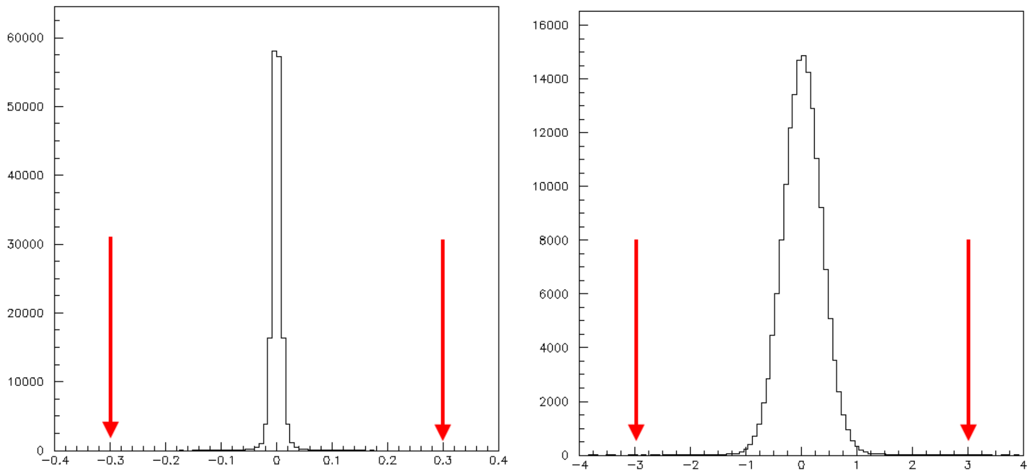

Figure 1.3: The Δr (*left*) and Δz (*right*) distribution of the charged particles candidates in signal MC sample.

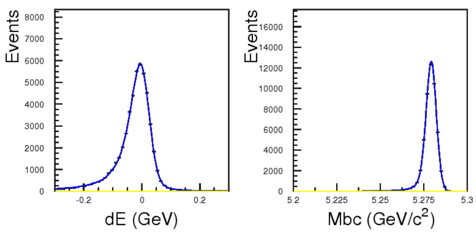

(a) $B^{\pm} \to \eta(\gamma\gamma)K^{\pm}$

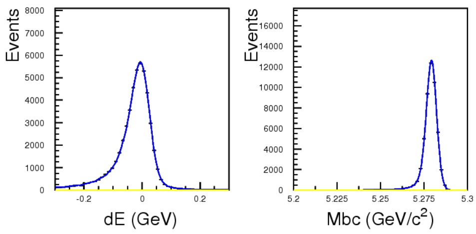

(b) $B^{\pm} \to \eta(\gamma\gamma)\pi^{\pm}$

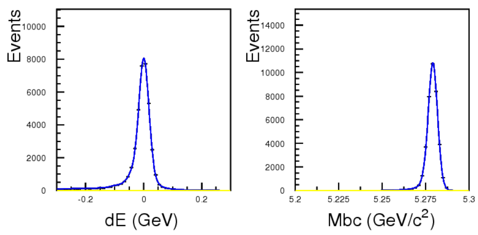

(c) $B^{\pm} \to \eta(\pi^+\pi^-\pi^0)K^{\pm}$

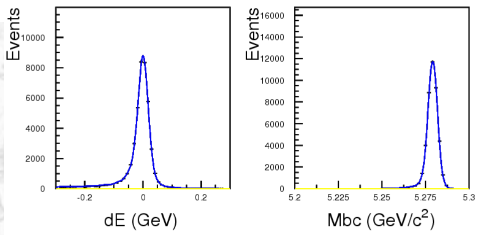

(d) $B^{\pm} \to \eta(\pi^+\pi^-\pi^0)\pi^{\pm}$

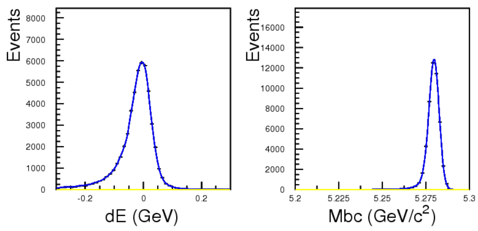

(e) $B^{\pm} \to \eta(\gamma\gamma)K^0_S$

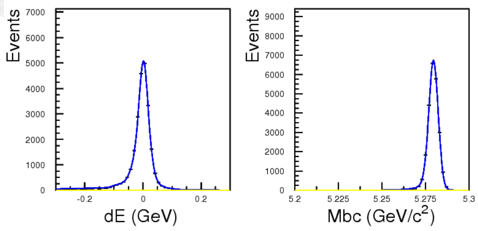

(f) $B^{\pm} \to \eta(\pi^+\pi^-\pi^0)K^0_S$

Figure 3.1: The Siganl MC ΔE and M_{bc} distribution and P.D.F.S.

Chapter 4

Background Suppression

4.1 Continuum Backgrounds

Our dominant background comes from the the $e^+e^- \to q\overline{q}(q = u, d, s, c)$ continuum events. The jet-like $q\overline{q}$ events allows us to separate them from more spherical $B\overline{B}$ events with event-shape variables.

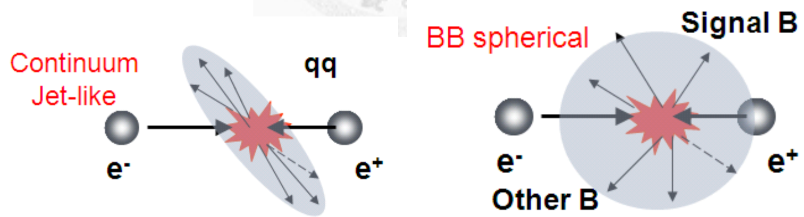

Figure 4.1: The momentum topology of jet-like $q\overline{q}$ events and spherical-like $B\overline{B}$ events.

4.1.1 Super Fox/Wolfram moment (SFW)

The definition of Fox/Wolfram moment is

$$R_l = \frac{H_l}{H_0} \text{ , where } H_l = \sum_{ij} \frac{|\overrightarrow{P_i}||\overrightarrow{P_j}|}{E_{total}} P_l(\cos\theta_{ij}) \ , \tag{4.1}$$

where P_l denotes the Legendre polynomial of order l, $\overrightarrow{P_i}$ and $\overrightarrow{P_j}$ stands for the momentum of daughter particles, and θ_{ij} is the included angle between $\overrightarrow{P_i}$ and $\overrightarrow{P_j}$. And Super Fox/Wolfram moment (SFW) is used to separate Fox/Wolfram moment into three parts, both daughter particles come from candidate B (denoted as ss), one daughter particle comes from candidate B and another comes from other particles (denoted as so), and both daughter particles come from other particles (denoted as oo)

$$R_l = R_l^{ss} + R_l^{so} + R_l^{oo} \ ,$$

We use the Fox/Wolfram moment up to fourth order,but R_l^{so},R_3^{so},R_l^{oo} are left out.

4.1.2 Fisher discriminant

We prepare a Fisher discriminant, large signal MC and $q\overline{q}$ MC samples for the continuum background suppression study. The main concept of the Fisher discriminant is to combine n-dimensional variables into one dimension by a linearly weighted sum.

We optimize the coefficients separately in 7 different missing mass (M_{miss}) regions based on 17 kinematic variables in the CM frame. The definition of M_{miss} is

$$MM^2 = \begin{cases} (E_{\Upsilon(4S)} - \Sigma_{n=1}^{N_t} E_n)^2 - (\Sigma_{n=1}^{N_t} \overrightarrow{P_n})^2 & \text{(a)} \\ -((E_{\Upsilon(4S)} - \Sigma_{n=1}^{N_t} E_n)^2 - (\Sigma_{n=1}^{N_t} \overrightarrow{P_n})^2) & \text{(b)} \end{cases} \tag{4.2}$$

$$\text{(a): if}, E_{\Upsilon(4S)} - \Sigma_{n=1}^{N_t} E_n > 0, \text{(b): otherwise}$$

where N_t stands for the total number of tracks in each event, and $E_n(\overrightarrow{P_n})$ stands for the energy(momentum) of each track. Table 4.1 summarizes the region of M_{miss} for each bin.

Table 4.1: The regions of missing mass of KSFW

Region	1	2	3	4
MM^2 (GeV/c^2)	< -0.5	$-0.5 < -0.3$	$0.3 < 1.0$	$1.0 < 2.0$
Region	5	6	7	
MM^2 (GeV/c^2)	$2.0 < 3.5$	$3.5 < 6.0$	> 6.0	

This algorithm, so-called KSFW, has been developed by H. Kakuno, and the variables are shown in the following.

(1) Total transverse momentum (P_t), summing up the momenta of all particles (1 variable).

(2) The ratio of nth-order to zeroth-order Super Fox-Wolfram (SFW) momentents, computing the ratio up to 5th-order by using different sets of particles: the charged particles from the B candidate and the remaining charged ones (5 variables); the neutral particles from the B candidate and the remaining neutral ones, only odd order is used (3 variables); the neutral particles from the B candidate and the total missing momentum, only odd order is used (3 variables); the charged and neutral particles excluding the particles from the B candidate (5 variables). The fisher distance for each M_{miss} bin are shown in Table 4.2, and the distributions of Fisher discriminant for each M_{miss} bin are shown in Fig. 4.2.

Table 4.2: The fisher distance for each M_{miss} bin.

M_{miss}	0	1	2	3	4	5	6
$\eta(\gamma\gamma)K^{\pm}$	1.79	2.15	1.99	1.93	1.58	1.32	1.25
$\eta(\pi^+\pi^-\pi^0)K^{\pm}$	1.76	2.16	2.03	1.83	1.60	1.38	1.24

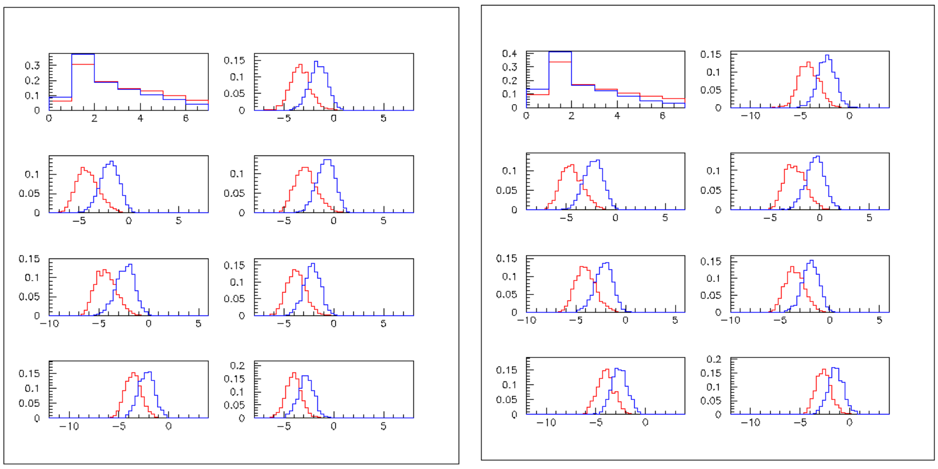

Figure 4.2: The distributions of M_{miss} and Fisher discriminant for each M_{miss} bin. The left figures stands for $\eta(\gamma\gamma)K^{\pm}$ and right ones stands for $\eta(\pi^{+}\pi^{-}\pi^{0})K^{\pm}$. The red line stands for signal MC and blue line stands for $q\overline{q}$ MC.

In addition to the Fisher discriminant, two variables are used to form the signal and background probability density function (PDFs), which are the $cos\theta_B$ and ΔZ. The θ_B is the B decay angle with respect to the z axis, and the ΔZ is the vertex difference on the z axis between the signal B event and its accompanying B. And we don't use the charge track in K_s^0 to calculate ΔZ, so no ΔZ information was used in $B \to \eta(\gamma\gamma)K_S^0$ decay.

4.1.3 Likelihood Ratio ($\mathcal{L}R$)

The products of the PDFs give the event-by-event signal and background likelihood, $\mathcal{L}_S$ and $\mathcal{L}_B$, allowing a selection to be applied to the likelihood ratio which is defined as

$$\mathcal{L}R = \frac{\mathcal{L}_S}{\mathcal{L}_S + \mathcal{L}_B}$$

Figure 4.3 shows the distribution of Fisher discriminant, $cos\theta_B$, ΔZ, and $\mathcal{L}R$ in signal MC and $q\overline{q}$ MC.

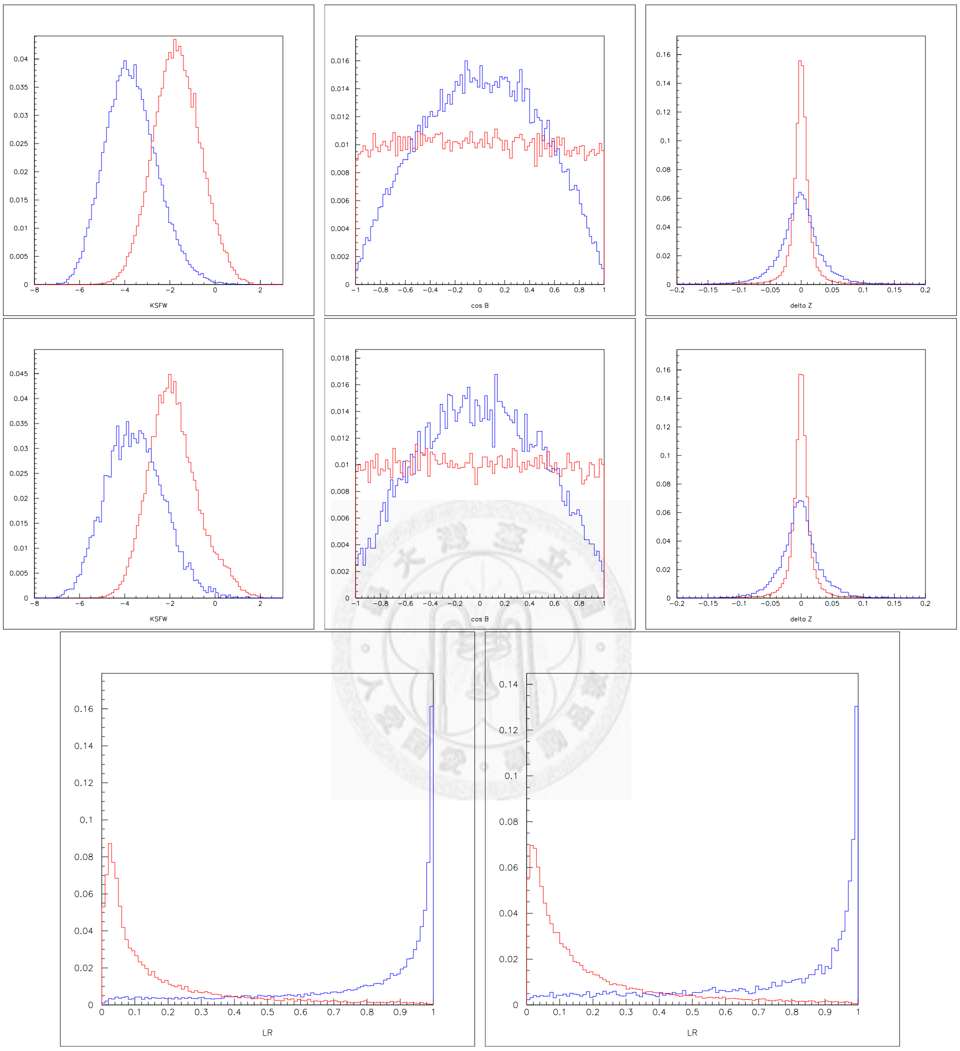

Figure 4.3: The distributions of the components of $\mathcal{L}R$ and itself. The top three figures denote Fisher discriminant, $cos\theta_B$, and ΔZ for the $B^{\pm} \to \eta(\gamma\gamma)K^{\pm}$ decay while the middle three ones are for $B^{\pm} \to \eta(\pi^+\pi^-\pi^0)K^{\pm}$ decay. The bottom left figure denotes the $\mathcal{L}R$ distribution for $B^{\pm} \to \eta(\gamma\gamma)K^{\pm}$ decay, and the The bottom right figure is for $B^{\pm} \to \eta(\pi^+\pi^-\pi^0)K^{\pm}$ decay. The blue line stands for signal MC while the red line stands for $q\bar{q}$ MC.

4.1.4 2D Fit (M_{bc} & ΔE)

The two dimensional fit is fitting at M_{bc} <5.2 and $|\Delta E| < 0.3$ with a high Likelihood Ratio cut. And the two dimensional fit is used in all previous $B \to \eta h$ study in belle.

Additional background discriminatoin in 2D fit is the flavor tagging information "q" and "r". The value of the preferred flavor q equals +1 for B^0/B^+ and -1 for $\overline{B}^0/B^-$. The tagging quality factor r ranges from 0 to 1 for no flavor to unambiguous flavor. For the $B^\pm \to \eta K^\pm$ and $B^\pm \to \eta\pi^\pm$ modes we separate the events in 6 "$q_B \times q \times r$" bins, where q_B is the charge of B candidate and $q \times r$ is from the tag B. The bins are more narrow near $q_B \times q \times r = -1$ and wider near $q_B \times q \times r = 1$. For the $B^0 \to \eta K^0$ mode we also separate the events in 6 "r" bins. Figure 4.4 shows the distributions of $q_B \times q \times r$ for $B^\pm \to \eta K^\pm$ and r for $B^0 \to \eta K^0$.

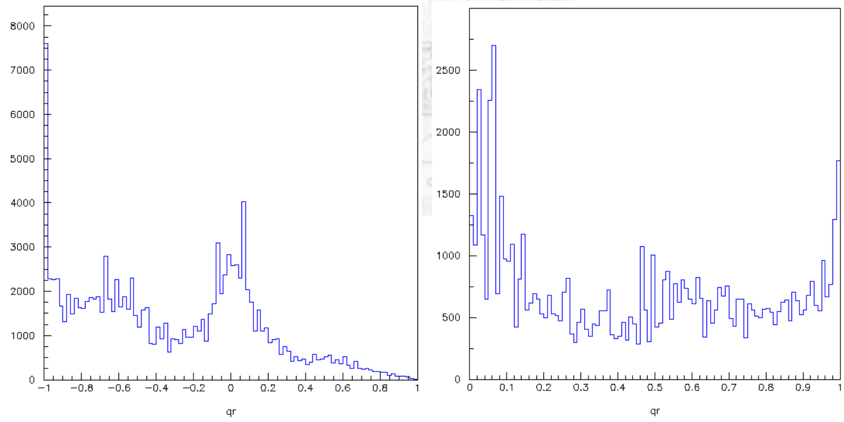

Figure 4.4: The "$q_B \times q \times r$" distributions for $B^\pm \to \eta K^\pm$ $(left)$ and "r" distributions for $B^\pm \to \eta K^0_S(right)$.

The $\mathcal{L}R$ cuts selection in 2D fit is optimized by maximizing the statistical significance ,Total Figure of Merit (F.O.M.), defined as $\sum_{i=1}^{n} \frac{N_{S,i}}{\sqrt{N_{S,i}+N_{B,i}}}$, where $N_{S,i}$ and $N_{B,i}$ denote the expected total signal and background yields in the signal box for the i^{th} $q_B \times q \times r$ bins.

We calculate N_S by

$$N_S = N_{B\overline{B}} \times \mathcal{B}F_{P.D.G.} \times \epsilon_{\rm MC}$$

where $N_{B\overline{B}}$, $\mathcal{B}F_{P.D.G.}$, and $\epsilon_{\rm MC}$ stands for the total number of B events from Exp. 7∼65. More information about FOM is showed at [Appendix A].

4.1.5 3D Fit (M_{bc} , ΔE & LR)

The three dimensional fit is fitting at M_{bc} <5.2 , $|\Delta E| < 0.3$,and $LR > 0.2$. In three dimensional fit we just need to apply a low Likelihood Ratio cut, so it will remain more siganl than the two dimensional fit.

Table 4.3: The summary of expected signal in signal box for 2D fit and 3D fit in each decay mode.

Decay mode	2D Fit	3D Fit
$\eta(\gamma\gamma)K^{\pm}$	148	240
$\eta(\gamma\gamma)\pi^{\pm}$	310	437
$\eta(\gamma\gamma)K_S^0$	174	196
$\eta(\pi^+\pi^-\pi^0)K^{\pm}$	59	93
$\eta(\pi^+\pi^-\pi^0)\pi^{\pm}$	22	34
$\eta(\pi^+\pi^-\pi^0)K_S^0$	9	13

Although 3D fit will remain more signal,and it also include more background in the fitting region. In order to compare the 2D fit and 3D fit, we do a simple ensemble test to check which one is better. The simple ensemble test just include signal and continum background. We put 148 signal and 6000 continum background in 2D fit and 240 signal and 98000 continum background in 3D fit to model the $\eta(\gamma\gamma)K^{\pm}$ mode. Finally we compare the $Yield_{mean}/Error_{mean}$ in 2D fit and 3D fit, then we find that 3D fit is better in this study. The $Yield_{mean}/Error_{mean}$ value is 7.48 in 2D fit and 8.68 in 3D fit. Figure 4.5 shows the M_{bc} and ΔE fitting result in 2D fit. Figure 4.6 shows the M_{bc}, ΔE and LR fitting result in 3D fit. Figure 4.7 shows the pull, yield and error result in 2D fit and Figure 4.8 for 3D fit. and here pull is difined by $PULL = (Yield - Mean)/Error$. Mean equal to 148 in 2D fit and 240 in 3D fit.

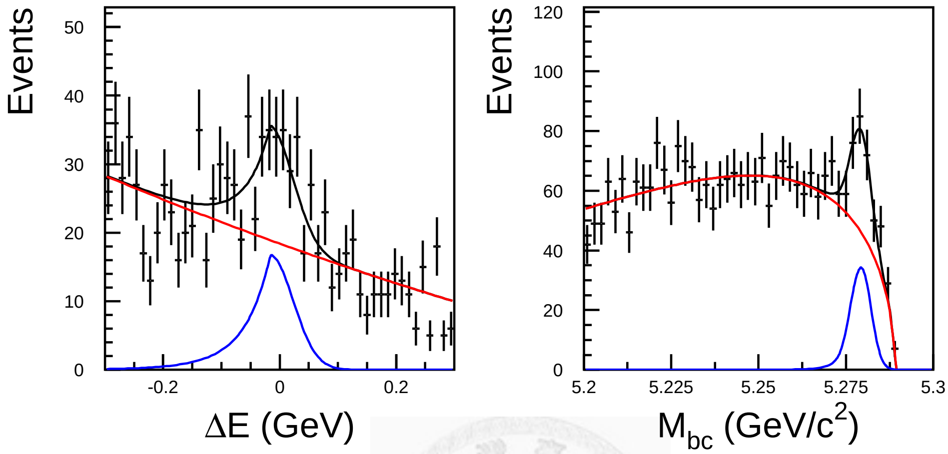

Figure 4.5: ΔE and M_{bc} fitting result in 2D ensemble test .

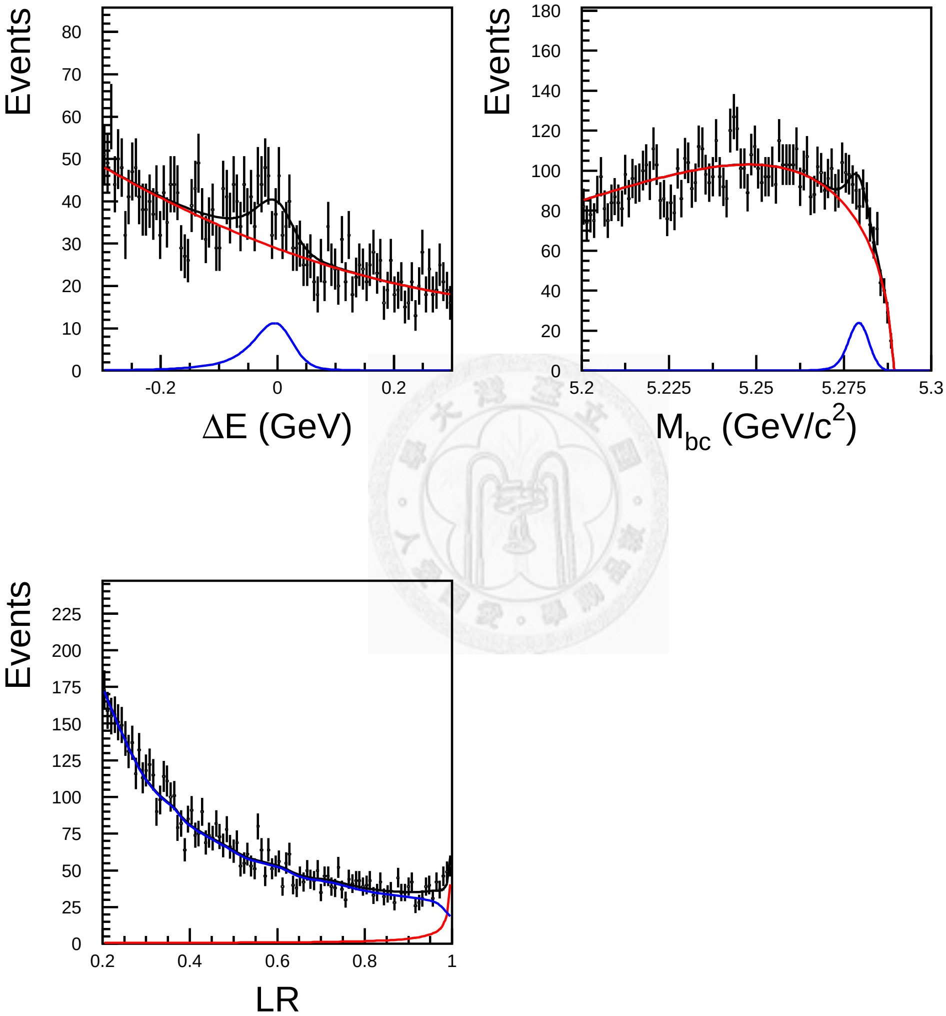

Figure 4.6: ΔE M_{bc}, and LR fitting result in 3D ensemble test .

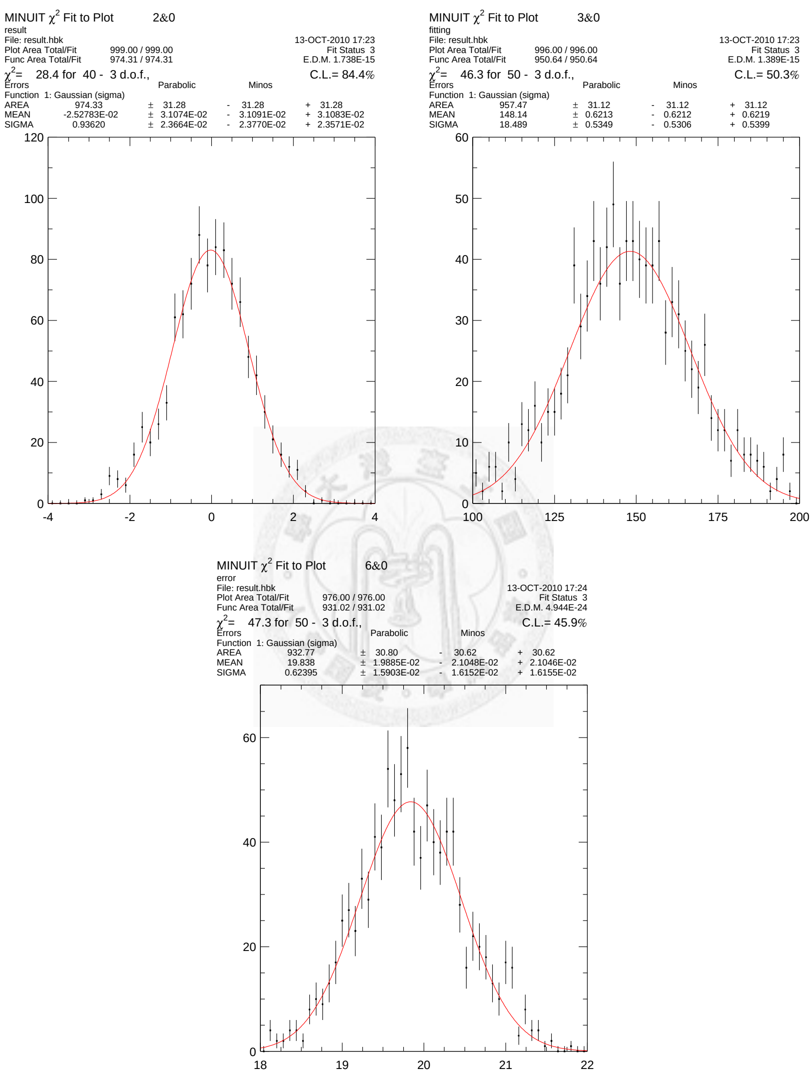

Figure 4.7: Pull, yield, error in 2D ensemble test .

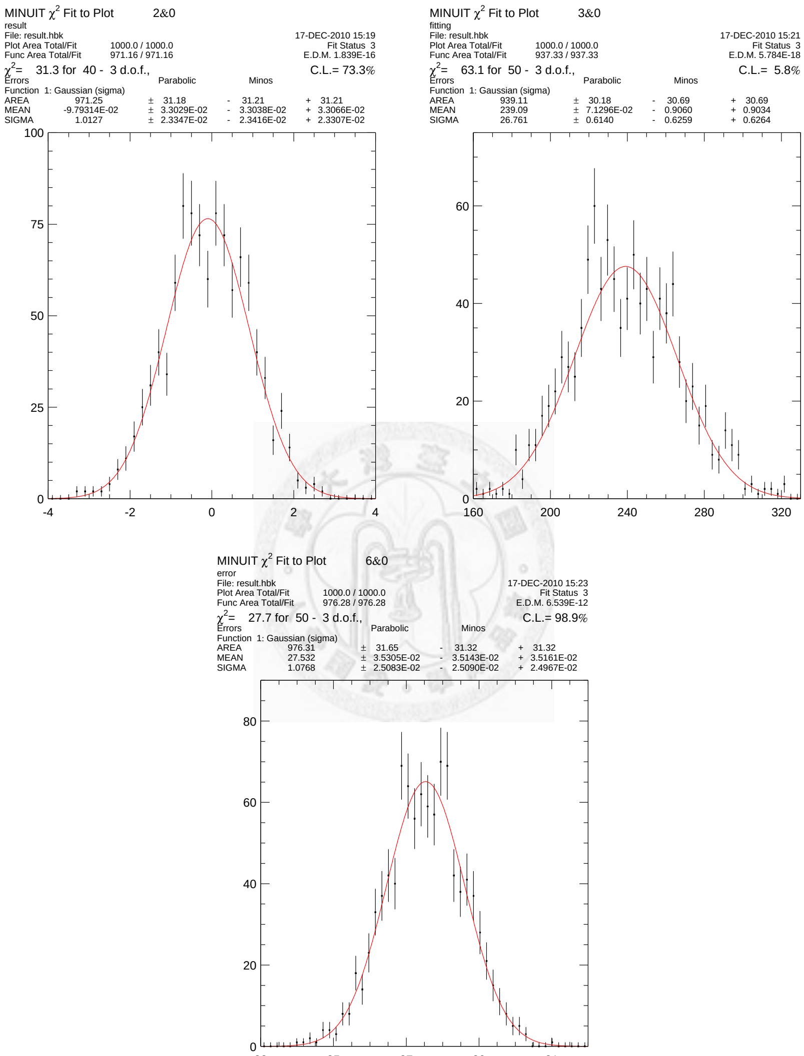

Figure 4.8: Pull, yield, error in 3D ensemble test .

4.2 Generic $B\overline{B}$ and rare B Backgrounds

There are two kinds of the $B\overline{B}$ backgrounds. The generic $B\overline{B}$, which denotes the $b \to c$ transition, and rare B, which denotes the $b \to u, d, s$ transition. These events are very few compared with $q\overline{q}$ continuum events. The generic $B\overline{B}$ background is less than 0.1% continuum background and have no peak at ΔE and M_{bc}, so we will neglect them. And for the rare B background we generate MC which is 50 times larger than real data to study its ΔE, M_{bc} and LR pdf. We will include the rare B background pdf in the real data fitting. Figure 4.9 shows the generic $B\overline{B}$ background $\Delta E - M_{bc}$ scatter plots and Figures 4.10 and 4.11 for rare B background.

4.3 Feedacross Backgrounds

In the $B^{\pm} \to \eta h^{\pm}$ fitting,we do the simultaneous fit of $B^{\pm} \to \eta(\gamma\gamma)K^{\pm}$ and $B^{\pm} \to \eta(\gamma\gamma)\pi^{\pm}$ (also have a simultaneous fit of $B^{\pm} \to \eta(\pi^+\pi^-\pi^0)K^{\pm}$ and $B^{\pm} \to \eta(\pi^+\pi^-\pi^0)\pi^{\pm}$), since these two decay modes feed across each other. The feedacross are constrained according to the KID efficiency and fake rate shown in the follow.

$$N^{(f)}_{\eta K^{\pm}} = N2_{fit(\eta\pi^{\pm})} \times \frac{\epsilon 1_{\eta\pi^{\pm}} \times (f_{K^+} + f_{K^-})}{\epsilon 2_{\eta\pi^{\pm}} \times (\epsilon_{\pi^+} + \epsilon_{\pi^-})}$$

$N^{(f)}_{\eta K^{\pm}}$: $\eta\pi$ fake to ηK

$N2_{fit(\eta\pi^{\pm})}$: the fitting yield of $\eta\pi$ in the $\eta\pi$ sample

$\epsilon 1_{\eta\pi^{\pm}}$:the $\eta\pi^{\pm}$ efficiency with KID cut in the ηK sample

$\epsilon 2_{\eta\pi^{\pm}}$:the $\eta\pi^{\pm}$ efficiency with KID cut in the $\eta\pi$ sample

$f_{K^{\pm}}$: the ratio of KID fake rate of $\frac{DATA}{MC}$

$\epsilon_{\pi^{\pm}}$: the ratio of KID efficiency of $\frac{DATA}{MC}$

Table 4.4 and Figure 4.12, show the ratio between feedacross backgrounds and fitting yield.

Table 4.4: The summary of ratio between feedacross backgrounds and fitting yield. For example, if there are 1 signal yield in $B^{\pm} \to \eta(\gamma\gamma)\pi^{\pm}$ decay mode, the fitter will force 0.08215 feedacross background in $B^{\pm} \to \eta(\gamma\gamma)K^{\pm}$ decay mode.

Decay mode	Ratio	Feedacross mode
$\eta(\gamma\gamma)K^{\pm}$	0.08215	$\eta(\gamma\gamma)\pi^{\pm}$
$\eta(\gamma\gamma)\pi^{\pm}$	0.11190	$\eta(\gamma\gamma)K^{\pm}$
$\eta(\pi^{+}\pi^{-}\pi^{0})K^{\pm}$	0.07685	$\eta(\pi^{+}\pi^{-}\pi^{0})\pi^{\pm}$
$\eta(\pi^{+}\pi^{-}\pi^{0})\pi^{+}$	0.11090	$\eta(\pi^{+}\pi^{-}\pi^{0})K^{+}$

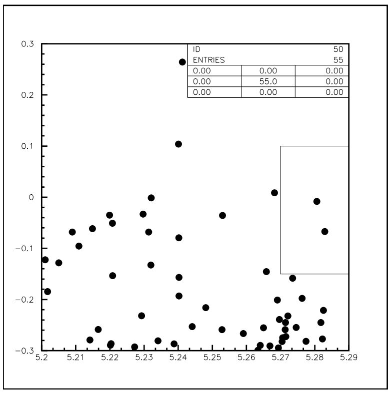

(a) $B^{\pm} \to \eta(\gamma\gamma)K^{\pm}$

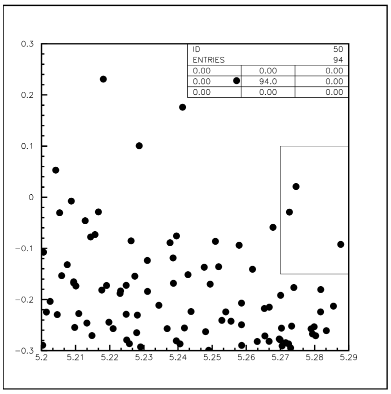

(b) $B^{\pm} \to \eta(\gamma\gamma)\pi^{\pm}$

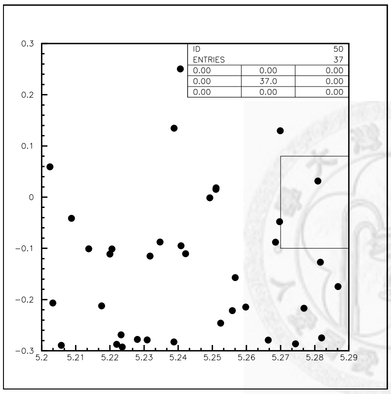

(c) $B^{\pm} \to \eta(\pi^{+}\pi^{-}\pi^{0})K^{\pm}$

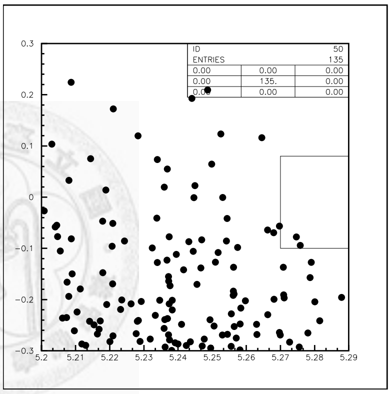

(d) $B^{\pm} \to \eta(\pi^{+}\pi^{-}\pi^{0})\pi^{\pm}$

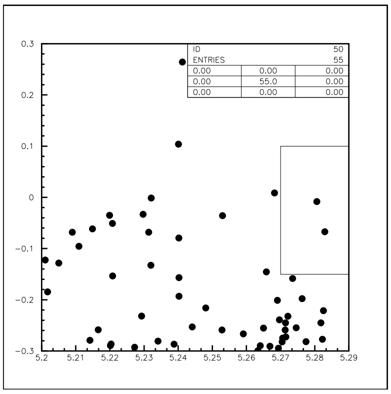

(e) $B^{\pm} \to \eta(\gamma\gamma)K_S^0$

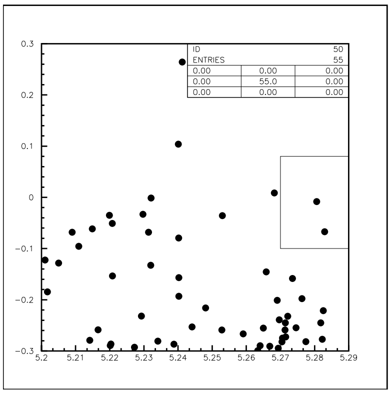

(f) $B^{\pm} \to \eta(\pi^{+}\pi^{-}\pi^{0})K_S^0$

Figure 4.9: The generic $B\overline{B}$ background $\Delta E - M_{bc}$ scatter plots.

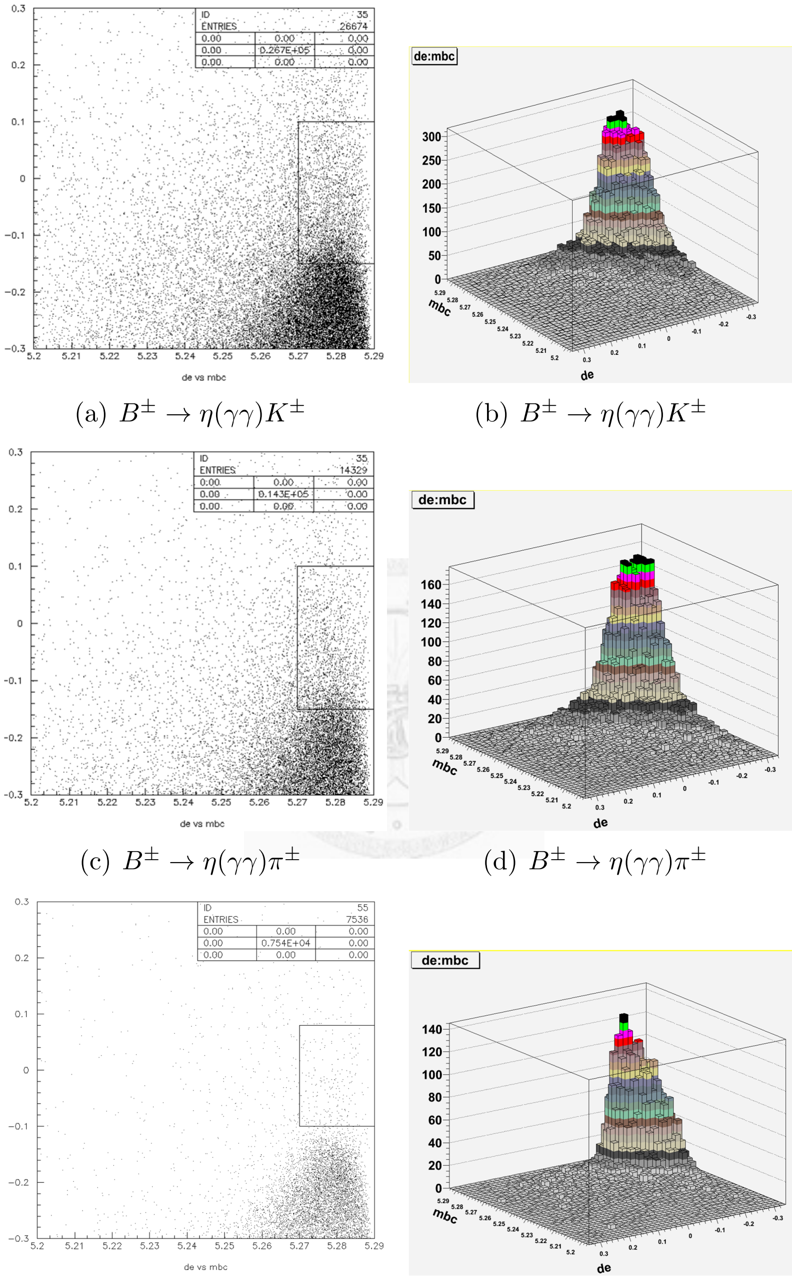

(a) $B^{\pm} \to \eta(\gamma\gamma)K^{\pm}$ (b) $B^{\pm} \to \eta(\gamma\gamma)K^{\pm}$

(c) $B^{\pm} \to \eta(\gamma\gamma)\pi^{\pm}$ (d) $B^{\pm} \to \eta(\gamma\gamma)\pi^{\pm}$

(e) $B^{\pm} \to \eta(\pi^+\pi^-\pi^0)K^{\pm}$ (f) $B^{\pm} \to \eta(\pi^+\pi^-\pi^0)K^{\pm}$

Figure 4.10: The rare $B\overline{B}$ background $\Delta E - M_{bc}$ scatter plots. Signal and feedacross background are already removed.

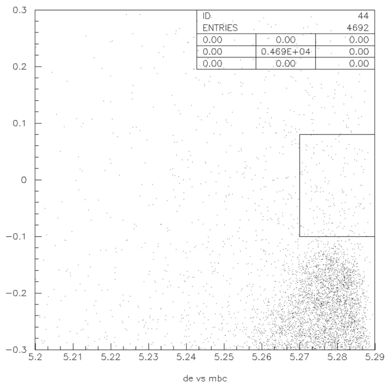

(a) $B^{\pm} \to \eta(\pi^+\pi^-\pi^0)\pi^{\pm}$

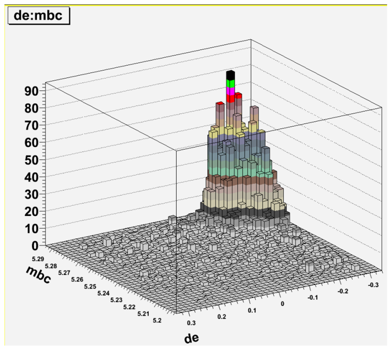

(b) $B^{\pm} \to \eta(\pi^+\pi^-\pi^0)\pi^{\pm}$

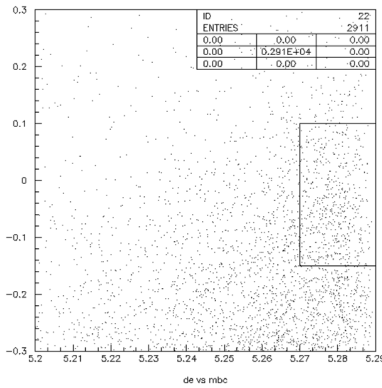

(c) $B^{\pm} \to \eta(\gamma\gamma)K_S^0$

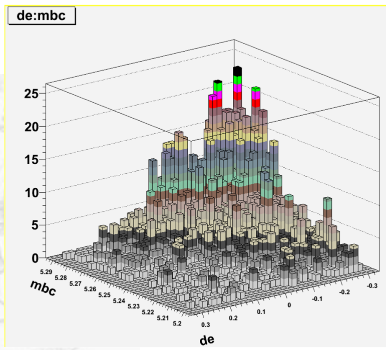

(d) $B^{\pm} \to \eta(\gamma\gamma)K_S^0$

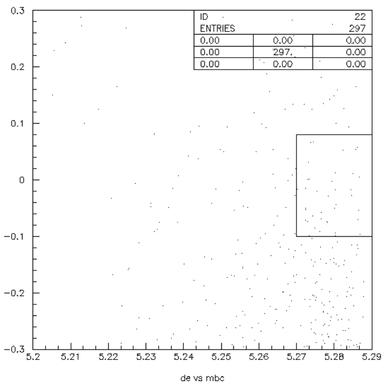

(e) $B^{\pm} \to \eta(\pi^+\pi^-\pi^0)K_S^0$

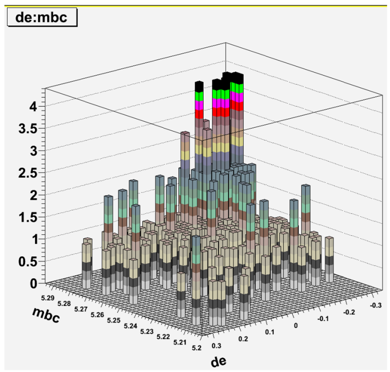

(f) $B^{\pm} \to \eta(\pi^+\pi^-\pi^0)K_S^0$

Figure 4.11: The rare $B\overline{B}$ background $\Delta E - M_{bc}$ scatter plots. Signal and feedacross background are already removed.

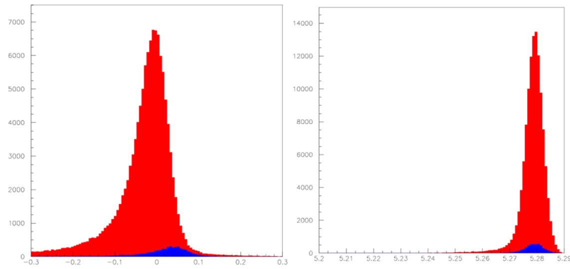

(a) $B^{\pm} \to \eta(\gamma\gamma)K^{\pm}$ signal and $B^{\pm} \to \eta(\gamma\gamma)\pi^{\pm}$ feed across

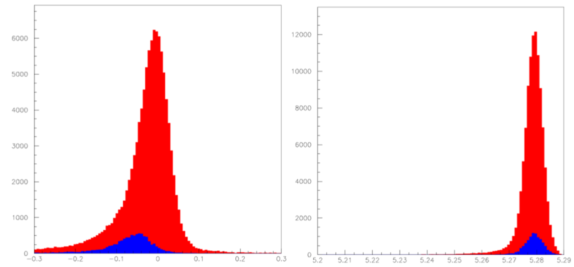

(b) $B^{\pm} \to \eta(\gamma\gamma)\pi^{\pm}$ signal and $B^{\pm} \to \eta(\gamma\gamma)K^{\pm}$ feed across

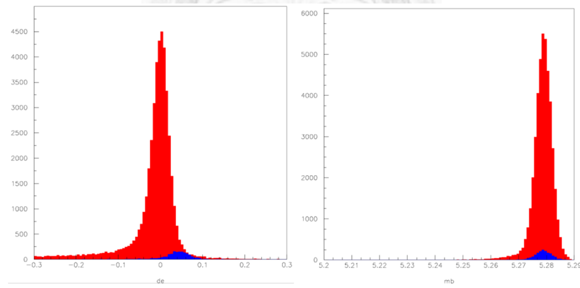

(c) $B^{\pm} \to \eta(\pi^+\pi^-\pi^0)K^{\pm}$ signal and $B^{\pm} \to \eta(\pi^+\pi^-\pi^0)\pi^{\pm}$ feed across

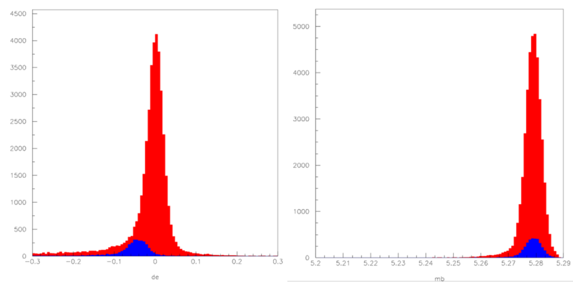

(d) $B^{\pm} \to \eta(\pi^+\pi^-\pi^0)\pi^{\pm}$ signal and $B^{\pm} \to \eta(\pi^+\pi^-\pi^0)K^{\pm}$ feed across

Figure 4.12: The signal (red) and feed across background (blue) ΔE and M_{bc} distribution and relative ratio in $B \to \eta h$ decay.

Chapter 5

Control Sample Study

Since M_{bc} ,ΔE and LR signal shapes are obtained with Monte Carlo simulations, it is necessary to study the difference between Monte Carlo simulation and real data.

We use the the decay mode $B^+ \to \overline{D}^0(K^+\pi^-\pi^0)\pi^+$ as our control sample. This high statistics decay mode has two photons and three charge particles in final state, which is similar to $B \to \eta(\pi^+\pi^-\pi^0)h$. And is also a good choice for $B \to \eta(\gamma\gamma)h$ (Because of the low statistics of $B \to \pi^0(\gamma\gamma)h$ decay, we do not use it as our control sample. And J. Wicht already showed that the $\mathcal{L}R$ cut systmatics error is rise to 6.9% with $B \to \pi^0(\gamma\gamma)h$ as his control sample. [12]).

The control sample here is used to study:

- The calibration factors between MC and real data
- The error of calibration factors (used to give systmatics error for M_{bc} ,ΔE PDF)
- The verification of $\mathcal{L}R$ cut and $\mathcal{L}R$ pdf.

We choose the full case B data (Exp.7$\sim$65) as the data sample and apply a very close selection criteria as used in the $B^\pm \to \eta(\pi^+\pi^-\pi^0)h^\pm$ decays.

All of them are listed in Table 5.2. And the ΔE width calibration factor is coming from inclusive $\overline{D}^0 \to K^+\pi^-\pi^0$.

Table 5.1: The selection criteria of $B^+ \to \overline{D}^0(K^+\pi^-\pi^0)\pi^+$

Basic selections	
Impact parameter	$\lvert\Delta r\rvert < 0.3$ cm
	$\lvert\Delta z\rvert < 3.0$ cm
KID	Kaon : $K/\pi > 0.6$
	Pion : $K/\pi < 0.4$
eID	eID < 0.95
μID	μID < 0.95
π^0 mass	0.115 GeV/$c^2 < M_{\pi^0} < 0.152$ GeV/c^2
Special selections	
D^0 mass	1.82 GeV/$c^2 < M_{D^0} < 1.89$ GeV/c^2

Table 5.2: The selection criteria of inclusive $\overline{D}^0 \to K^+\pi^-\pi^0$

Basic selections	
Impact parameter	$\lvert\Delta r\rvert < 0.3$ cm
	$\lvert\Delta z\rvert < 3.0$ cm
KID	Kaon : $K/\pi > 0.6$
	Pion : $K/\pi < 0.4$
eID	eID < 0.95
μID	μID < 0.95
π^0 mass	0.115 GeV/$c^2 < M_{\pi^0} < 0.152$ GeV/c^2
Special selections	
D^{0*} mass	D^{0*} mass - D^0 mass < 150 MeV/c^2
D^0 daughters momentum cut	>1.0 GeV

5.1 The calibration factors between MC and real data

In the signal pdf calibration, we use the control sample to calibrate the difference by extracting the signal yield with 3-D unbinned extended maximum likelihood translated $\mathcal{L}R$, $M_{\rm bc}$ and ΔE fit from both data and MC. The fitting results are shown in Fig C.6 and C.5, and the fudge factors are listed in Table 5.4. The ΔE mean shift for $\eta(\gamma\gamma)h$ mode is studying in $B \to \pi^0 K$ and $B \to \pi^0\pi$ decays. Which is $6.89 + 2.07 - 4.94$ MeV.

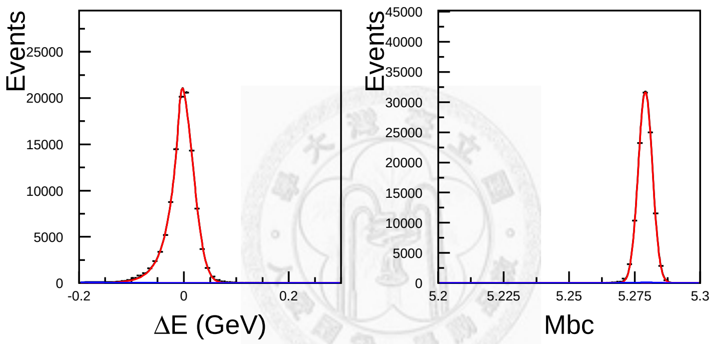

Figure 5.1: The ΔE (left) and $M_{\rm bc}$ (right) distribution for $B^+ \to \overline{D}^0(K^+\pi^-\pi^0)\pi^+$ signal MC.

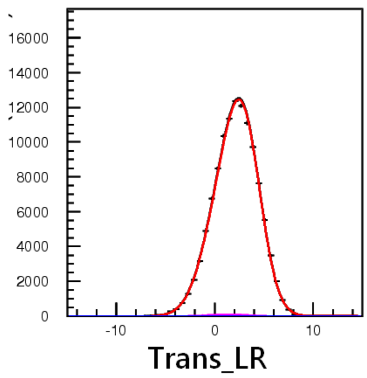

Figure 5.2: The translated $\mathcal{L}R$ distribution for $B^+ \to \overline{D}^0(K^+\pi^-\pi^0)\pi^+$ signal MC.

Table 5.3: The fitting results of Fig. 3.1 and Fig. 3.2. The shape parameter of the PDFs are listed in Table 5.4.

	Fig. 3.1 (Signal MC)	Fig. 3.2 (Exp. $7 \sim 65$ Data)
Entries	107897 ± 330	68642 ± 412

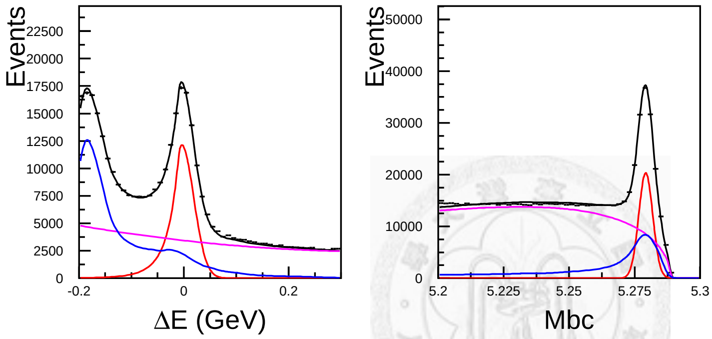

Figure 5.3: The ΔE (left) and $M_{\rm bc}$ (right) distribution for $B^+ \to \overline{D}^0(K^+\pi^-\pi^0)\pi^+$ realdata (Exp. $7 \sim 65$).

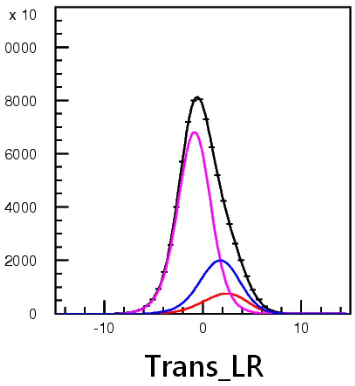

Figure 5.4: The translated $\mathcal{L}R$ distribution for $B^+ \to \overline{D}^0(K^+\pi^-\pi^0)\pi^+$ realdata (Exp. $7 \sim 65$).

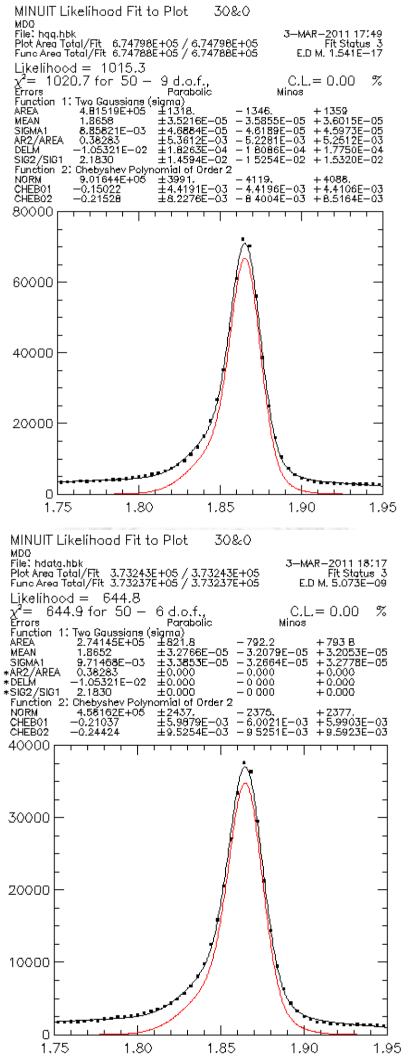

Figure 5.5: The D^0 mass distribution of inclusive $\overline{D}^0 \to K^+\pi^-\pi^0$ decay, in $c\bar{c}$ MC (top) and real data (down).

Table 5.4: The calibration factors. All units are MeV/c^2 for $M_{\rm bc}$ parameters and MeV for ΔE parameters.

	$M_{\rm bc}$ mean	$M_{\rm bc}$ width
Signal MC	5279.025 ± 0.007	2.638 ± 0.009
Data	5279.210 ± 0.015	2.659 ± 0.013
Difference/Ratio	0.185 ± 0.017	1.008 ± 0.006
	ΔE mean	ΔE width
Signal MC	-5.525 ± 0.159	8.858 ± 0.047
Data	-6.447 ± 0.223	9.715 ± 0.034
Difference/Ratio	-0.922 ± 0.274	1.097 ± 0.006
	translated $\mathcal{L}R$ mean	translated $\mathcal{L}R$ width
Signal MC	3.2122 ± 0.0064	1.7142 ± 0.0042
Data	3.2050 ± 0.0108	1.7148 ± 0.0072
Difference/Ratio	-0.0072 ± 0.0126	1.0004 ± 0.0049

Chapter 6

Signal Extraction

6.1 Signal And Background PDFs

We preform a three-dimentional unbinned extended maximum likelihood fit to $M_{\rm bc}$, ΔE and $\mathcal{L}R$ for extracting the $B \to \eta h$ signal yields. And get the $\mathcal{A}^S_{CP}$ (partial rate asymmetries for signals).

The extended likelihood for $B^0 \to \eta h^0$ is defined as

$$\begin{aligned}\mathcal{L} &= \frac{e^{-(N_S+N_B)}}{N!} \times \prod_{i=1}^{N} [\frac{(1-q_B\mathcal{A}^S_{CP})}{2} N_S P^i_S(M_{\rm bc}, \Delta E, \mathcal{L}R) \\ & \quad + \frac{(1-q_B\mathcal{A}^B_{CP})}{2} N_B P^i_B(M_{\rm bc}, \Delta E, \mathcal{L}R) \end{aligned} \tag{6.1}$$

where N denotes the number of events in the candidate region (5.20 GeV/c^2 < $M_{\rm bc}$ < 5.29 GeV/c^2, -0.3 GeV < ΔE < 0.3 GeV), $P^i_{S(B)}$ denotes the probability density function (PDF) of signal (qq and rare B backgrounds) for the ith event. q_B denotes the flavor of B^0 (+1/-1 for $B^0/\overline{B^0}$). And $\mathcal{A}^S_{CP}(\mathcal{A}^B_{CP})$ are the partial rate asymmetries for signals(qq and rare B background).

For the $B^{\pm} \to \eta h^{\pm}$ mode, The extended likelihood is defined as

$$\begin{aligned}
\mathcal{L} &= \frac{e^{-(N_S+N_B)}}{N!} \times \prod_{i=1}^{N} [\frac{(1-q_B\mathcal{A}_{CP}^S)}{2} N_S P_S^i(M_{\rm bc}, \Delta E, \mathcal{L}R) \\
&\quad + \frac{(1-q_B\mathcal{A}_{CP}^B)}{2} N_B P_B^i(M_{\rm bc}, \Delta E, \mathcal{L}R) \qquad (6.2)\\
&\quad + \frac{(1-q_B\mathcal{A}_{CP}^S)}{2} N_{FC} P_{FC}^i(M_{\rm bc}, \Delta E, \mathcal{L}R)] \;, \qquad (6.3)
\end{aligned}$$

where q_B denotes the flavor of B (+1/-1 for B^+/B^-), and $\mathcal{A}_{CP}^S(\mathcal{A}_{CP}^B)$ are the partial rate asymmetries for signals(qq and rare B background). By maximizing $\mathcal{L}$, we can get the signal yield (N_S). And N_{FC} denotes the feedacross yield (the feedacross background in $\eta K^{\pm}$ ($\eta\pi^{\pm}$) mode share a same $\mathcal{A}_{CP}^S$ value with signal in $\eta\pi^{\pm}$ ($\eta K^{\pm}$) mode).

In the $B \to \eta K_S^0$ decay mode, the flavor of B meson is determined via the accompany B meson. We calibrate the A_{cp} with $B^0 - \overline{B^0}$ oscillation probability and the faulty tagging as

$$A_{cp}(1-\chi_d)(1-w_l).$$

Where $\chi_d = 0.1872 \pm 0.0024$ is the $B^0 - \overline{B^0}$ mixing parameter [6], which denotes the probabilitly of a $B^0(\overline{B^0})$ decay with a $\overline{B^0}(B^0)$ channel. And the w_l denotes the wrong tagging fraction with r dependence. r denotes the tagging quality of the $B^0(\overline{B^0})$ flavor. And we sepatate r with six bins. The summary of w_l is showed at Table 6.1 [7] [14].

Because there is a correlation between $M_{\rm bc}$ and ΔE [Appendix C], we use a 2-D smooth function to model the $M_{\rm bc}$ and ΔE PDFs in signal, rare B background and feedacross background. We get their PDF by the production of 2-D $M_{\rm bc} - \Delta E$ PDFs and $\mathcal{L}R$ PDFs. And the continumm background PDF is the production of $M_{\rm bc}$, ΔE and $\mathcal{L}R$. The parameters of continumm background $M_{\rm bc}$ and ΔE PDF are set to float, while the parameters of signal PDF are fixed at Monte-Carlo value, but the peak position and width are calibrated via control sample. The details are listed in Table 6.7. Here smooth function means smoothed histogram.

Table 6.1: The wrong-tagging fraction w_l for tagged B^0 and $\overline{B^0}$ in each r bin.

r interval	w_l for $B^0(tagged)$	w_l for $\overline{B^0}(tagged)$
$0.000 \sim 0.250$	0.462 ± 0.007	0.453 ± 0.007
$0.250 \sim 0.500$	0.339 ± 0.011	0.333 ± 0.011
$0.500 \sim 0.625$	0.211 ± 0.012	$0.246 \pm^{0.013}_{0.012}$
$0.625 \sim 0.750$	0.148 ± 0.010	0.173 ± 0.011
$0.750 \sim 0.875$	0.101 ± 0.011	0.122 ± 0.011
$0.875 \sim 1.000$	$0.020 \pm^{0.007}_{0.006}$	0.020 ± 0.006

Table 6.2: The PDFs for $M_{\rm bc}$, ΔE and translated $\mathcal{L}R$ 3-D fit in $B \to \eta(\gamma\gamma)h$ modes.

		PDF
Signals	$M_{\rm bc}$	One Gaussian
	ΔE	CBline function
	$\mathcal{L}R$	One Gaussian
Continuum Background	$M_{\rm bc}$	Argus function
	ΔE	2^{nd} order Chebyshev
	$\mathcal{L}R$	Two Gaussian
Rare B Background	$M_{\rm bc}$	2-D smooth function
	ΔE	2-D smooth function
	$\mathcal{L}R$	One Gaussian
Feedacross Background	$M_{\rm bc}$	One Gaussian
	ΔE	CBline function
	$\mathcal{L}R$	One Gaussian

Table 6.3: The PDFs for $M_{\rm bc}$, ΔE and translated $\mathcal{L}R$ 3-D fit in $B \to \eta(\pi^+\pi^-\pi^0)h$ modes.

		PDF
Signals	$M_{\rm bc}$	One Gaussian
	ΔE	Two Gaussian
	$\mathcal{L}R$	One Gaussian
Continuum Background	$M_{\rm bc}$	Argus function
	ΔE	2^{nd} order Chebyshev
	$\mathcal{L}R$	Two Gaussian
Rare B Background	$M_{\rm bc}$	2-D smooth function
	ΔE	2-D smooth function
	$\mathcal{L}R$	One Gaussian
Feedacross Background	$M_{\rm bc}$	One Gaussian
	ΔE	Two Gaussian
	$\mathcal{L}R$	One Gaussian

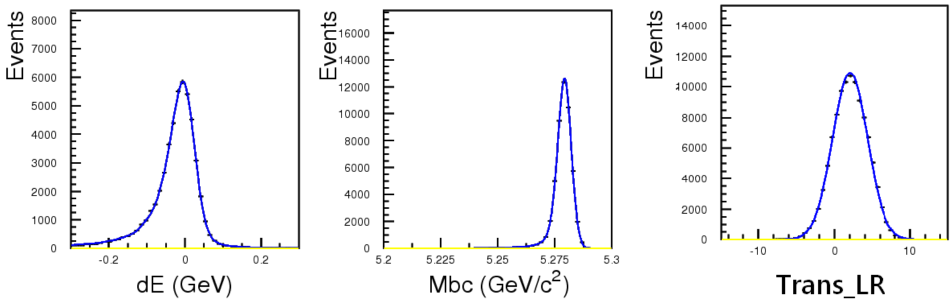

(a) $B^{\pm} \to \eta(\gamma\gamma)K^{\pm}$

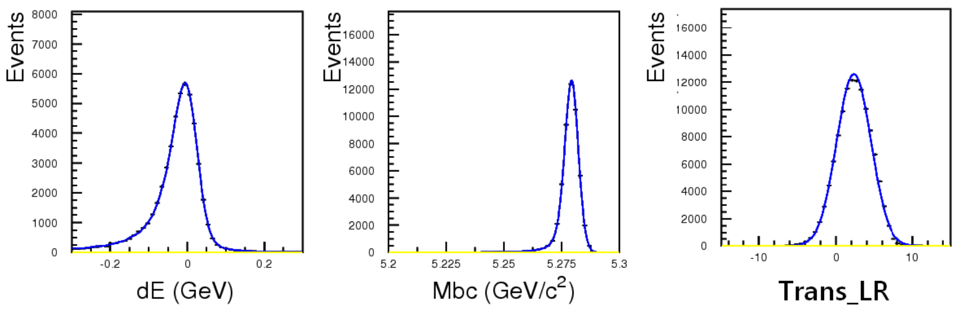

(b) $B^{\pm} \to \eta(\gamma\gamma)\pi^{\pm}$

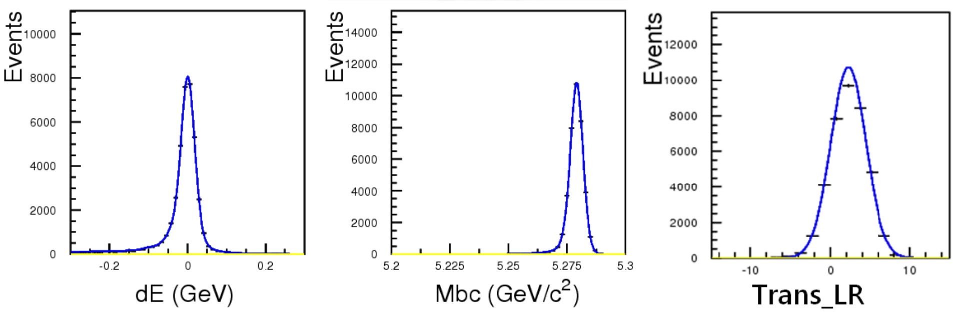

(c) $B^{\pm} \to \eta(\pi^{+}\pi^{-}\pi^{0})K^{\pm}$

Figure 6.1: The 3D fit ΔE, M_{bc} and translated $\mathcal{L}R$ plots in ηh siganl MC (from left to right).

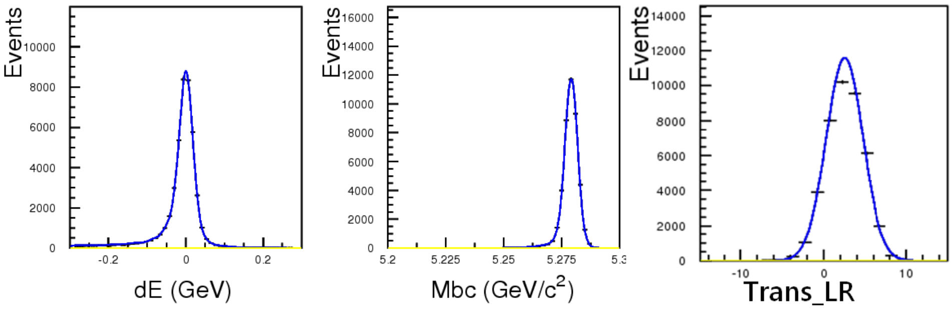

(a) $B^{\pm} \to \eta(\pi^+\pi^-\pi^0)\pi^{\pm}$

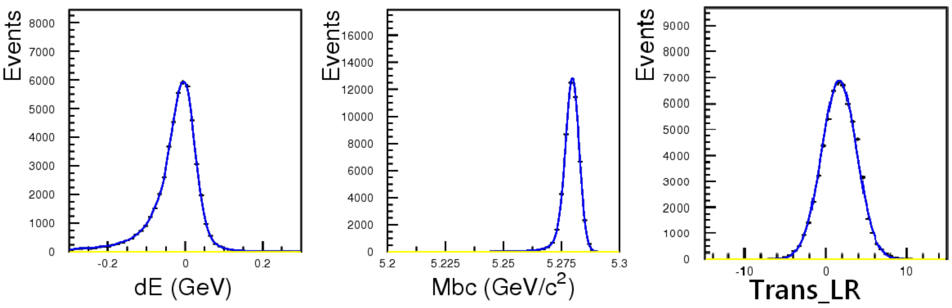

(b) $B^0 \to \eta(\gamma\gamma)K_S^0$

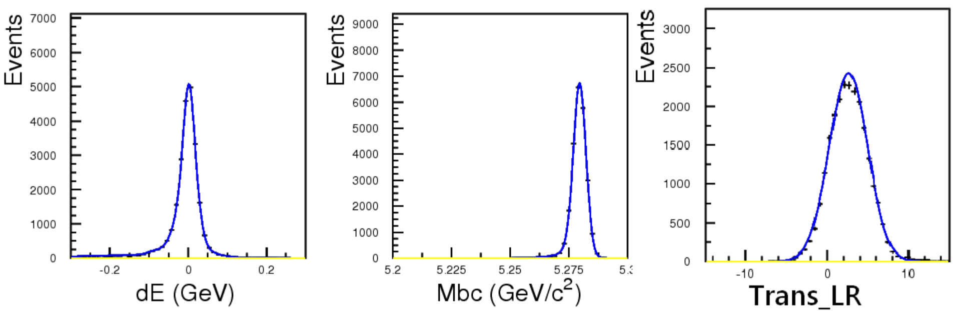

(c) $B^0 \to \eta(\pi^+\pi^-\pi^0)K_S^0$

Figure 6.2: The 3D fit ΔE, M_{bc} and translated $\mathcal{L}R$ plots in ηh siganl MC (from left to right).

6.2 Ensemble Test

Ensemble test is used to check the fit bias in our fitter, The fit bias in P. Chang's $B \to \eta h$ study is very small, is not so large in J. Wicht's [2]. And the fit bias for $B \to \eta h$ experiment in Babar is very large [1]. Babar have 9.8% fit bias in the $B^{\pm} \to \eta(\gamma\gamma)K^{\pm}$ mode (8.7% fit bias in $B^{\pm} \to \eta(\pi^{+}\pi^{-}\pi^{0})K^{\pm}$).

In our ensemble, all the signals are come from GSIM MC, and backgrounds are toy. So, the correlation effect in signal has been included. Since we do the simultaneous fit for $B^{\pm} \to \eta(\gamma\gamma)K^{\pm}$ and $B^{\pm} \to \eta(\gamma\gamma)\pi^{\pm}$ (also have a simultaneous fit for $B^{\pm} \to \eta(\pi^{+}\pi^{-}\pi^{0})K^{\pm}$ and $B^{\pm} \to \eta(\pi^{+}\pi^{-}\pi^{0})\pi^{\pm}$). So, we have four ensemble tests for six $B \to \eta h$ mode. And there is 1000 samples in each ensemble test.

The number of events in our ensemble tests' samples is generated by poisson distribution. The pull value is defined by : $PULL = \frac{Yield - Poisson_{mean}}{Error}$.

In order to study the fit bias of A_{CP}, we let the signal in our sample carry the A_{CP} of PDG value which is -0.37 for $B^{\pm} \to \eta K^{\pm}$ and -0.13 for $B^{\pm} \to \eta\pi^{\pm}$. Since there is no A_{CP} value of $B^{\pm} \to \eta K_S^0$ mode showed in PDG, we let the signal A_{CP} equal to -0.1, -0.2, -0.3, -0.4 and -0.5. So, there are 200 samples for each A_{CP} value in $B^0 \to \eta K_S^0$ ensemble test. And all background A_{CP} is equal to 0 in our sample.

The ensemble tests result show that we have a small signal yield fit bias in $B^{\pm} \to \eta(\gamma\gamma)K^{\pm}$ mode (-2.86%). And also a small A_{CP} fit bias in $B^{\pm} \to \eta(\gamma\gamma)K^{\pm}$ mode (-2.9%).

Since we use no correlate signal PDFs to describe a small correlate signal smaple, that is possible to have a small fit bias. But we have fit bias in $B^{\pm} \to \eta(\gamma\gamma)K^{\pm}$ mode and do not have bias in $B^{\pm} \to \eta(\gamma\gamma)\pi^{\pm}$ mode. We find that the reason is come for rare B background. Because there is no bias in continuum background in $B^{\pm} \to \eta(\gamma\gamma)K^{\pm}$ mode. To the ratio of signal and rare B background in $B^{\pm} \to \eta(\gamma\gamma)\pi^{\pm}$ mode is 4 times larger than in $B^{\pm} \to \eta(\gamma\gamma)K^{\pm}$ mode.

6.2.1 $B^{\pm} \to \eta(\gamma\gamma)K^{\pm}$ and $B^{\pm} \to \eta(\gamma\gamma)\pi^{\pm}$ Signal Yield Ensemble Test

Table 6.4: The poisson distribution mean for signal and background in our ensemble test.

	$B^{\pm} \to \eta(\gamma\gamma)K^{\pm}$	$B^{\pm} \to \eta(\gamma\gamma)\pi^{\pm}$
Signals	240	435
Continuum Background	80000	160000
Rare B Background	540	290
Feedacross Background	36	27

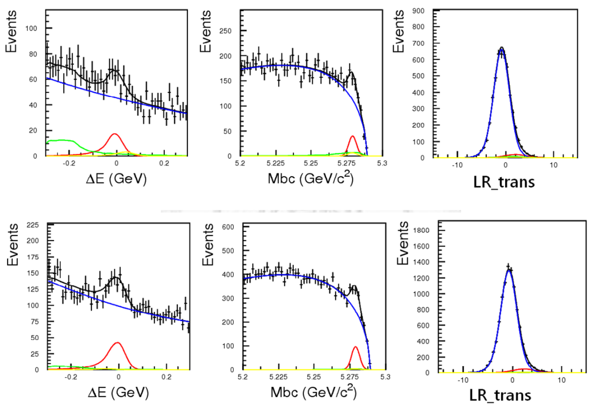

Figure 6.3: The projection plots from ensemble test. The red line is signal PDF, blue line is continuum background, green for rare B and yellow for freedacross. The ΔE plot is showed with projection $M_{bc} > 5.27$ and $\mathcal{L}R > 0.7$. M_{bc} plot is showed with projection $-0.15 < \Delta E < 0.1$ and $\mathcal{L}R > 0.7$. $\mathcal{L}R$ plot is showed with projection $-0.15 < \Delta E < 0.1$ and $M_{bc} > 5.27$. The top one is from $B^{\pm} \to \eta(\gamma\gamma)K^{\pm}$ mode, and the bottom one is from $B^{\pm} \to \eta(\gamma\gamma)\pi^{\pm}$.

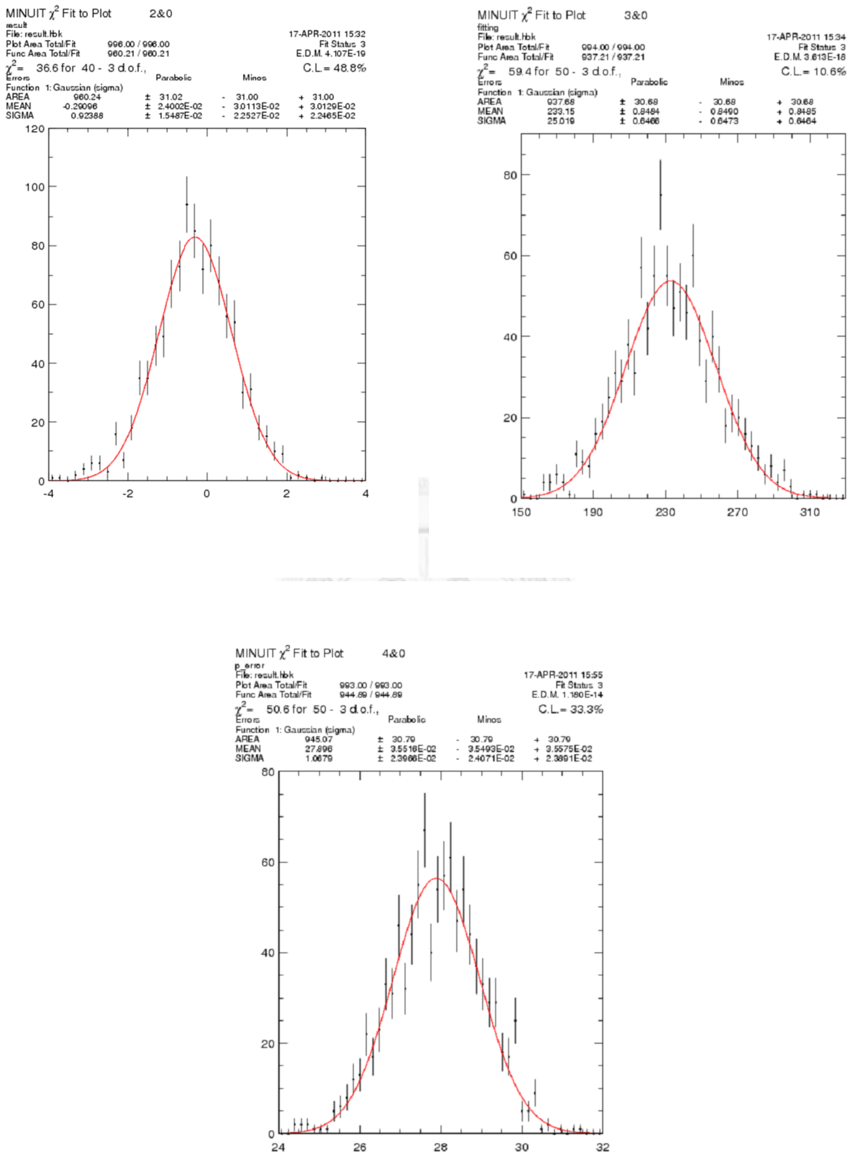

Figure 6.4: The ensemble test result in $B^{\pm} \to \eta(\gamma\gamma)K^{\pm}$ mode. Pull(upper left side), yield(upper right side) and error(bottom) distribution.

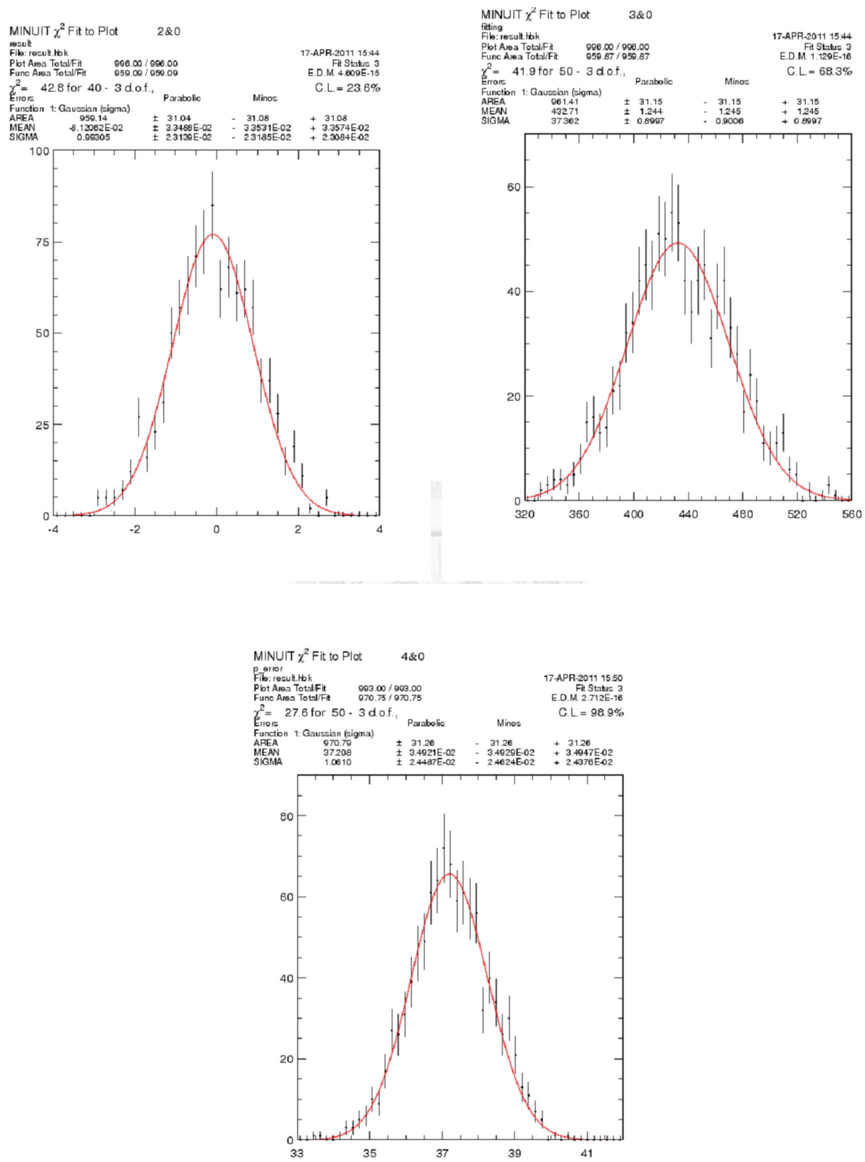

Figure 6.5: The ensemble test result in $B^{\pm} \to \eta(\gamma\gamma)\pi^{\pm}$ mode. Pull(upper left side), yield(upper right side) and error(bottom) distribution.

6.2.2 $B^{\pm} \to \eta(\pi^+\pi^-\pi^0)K^{\pm}$ and $B^{\pm} \to \eta(\pi^+\pi^-\pi^0)\pi^{\pm}$ Signal Yield Ensemble Test

Table 6.5: The poisson distribution mean for signal and background in our ensemble test.

	$B^{\pm} \to \eta(\pi^+\pi^-\pi^0)K^{\pm}$	$B^{\pm} \to \eta(\pi^+\pi^-\pi^0)\pi^{\pm}$
Signals	93	166
Continuum Background	33000	58000
Rare B Background	150	95
Feedacross Background	13	10

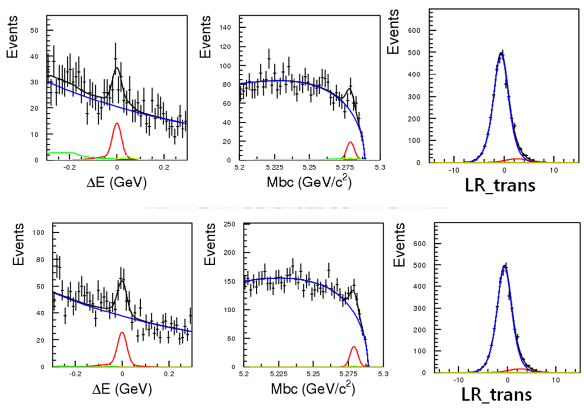

Figure 6.6: The projection plots from ensemble test. The ΔE plot is showed with projection $M_{bc} > 5.27$ and $\mathcal{L}R > 0.7$. M_{bc} plot is showed with projection $-0.1 < \Delta E < 0.08$ and $\mathcal{L}R > 0.7$. $\mathcal{L}R$ plot is showed with projection $-0.1 < \Delta E < 0.08$ and $M_{bc} > 5.27$. The top one is from $B^{\pm} \to \eta(\pi^+\pi^-\pi^0)K^{\pm}$ mode, and the bottom one is from $B^{\pm} \to \eta(\pi^+\pi^-\pi^0)\pi^{\pm}$.

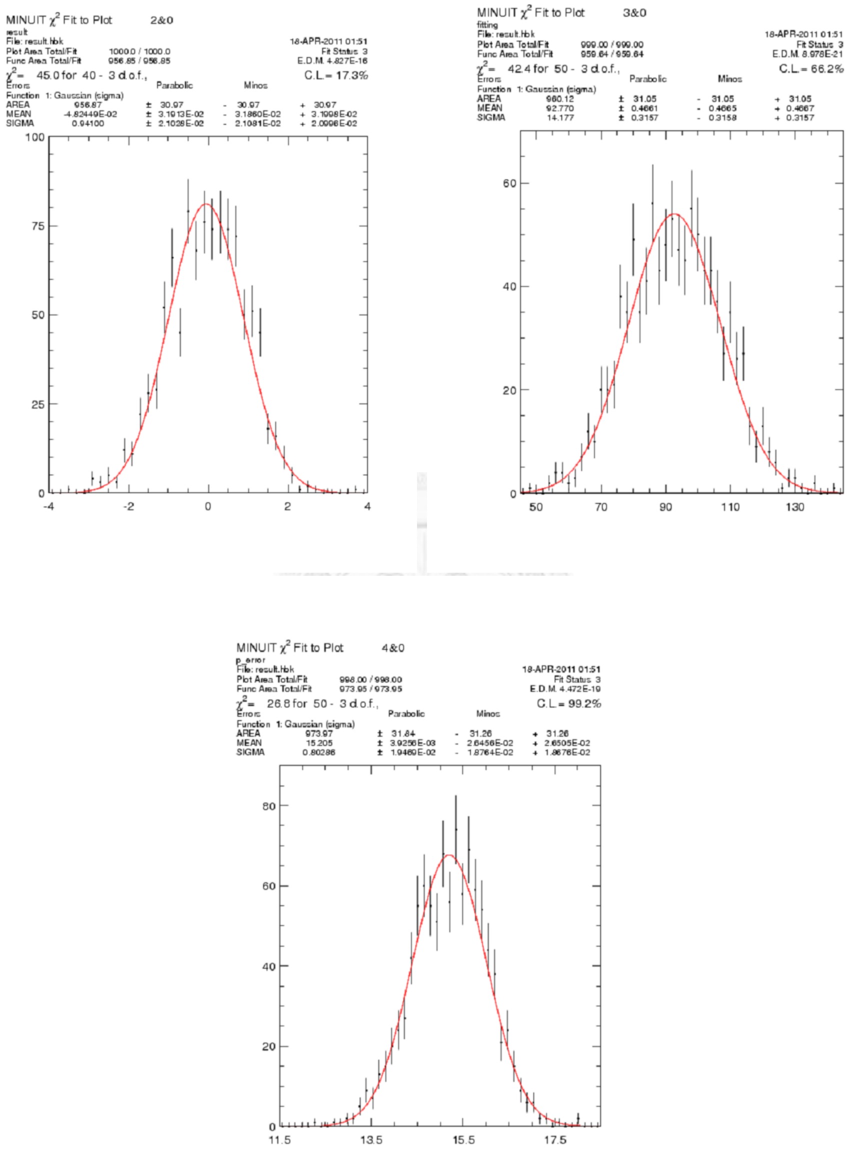

Figure 6.7: The ensemble test result in $B^{\pm} \rightarrow \eta(\pi^{+}\pi^{-}\pi^{0})K^{\pm}$ mode. Pull(upper left side), yield(upper right side) and error(bottom) distribution.

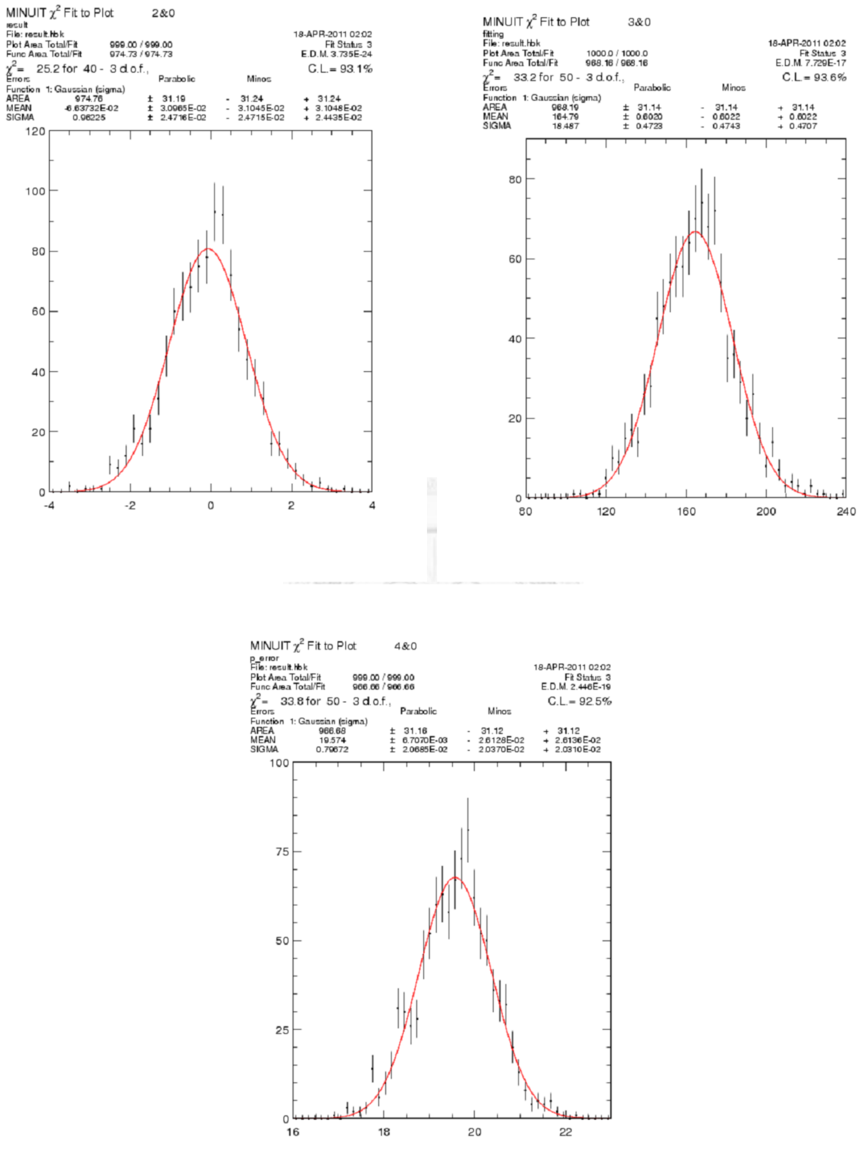

Figure 6.8: The ensemble test result in $B^{\pm} \to \eta(\pi^{+}\pi^{-}\pi^{0})\pi^{\pm}$ mode. Pull(upper left side), yield(upper right side) and error(bottom) distribution.

6.2.3 $B^0 \to \eta(\gamma\gamma)K_S^0$ Signal Yield Ensemble Test

Table 6.6: The poisson distribution mean for signal and background in our ensemble test.

	$B^0 \to \eta(\gamma\gamma)K_S^0$
Signals	34
Continuum Background	14000
Rare B Background	60

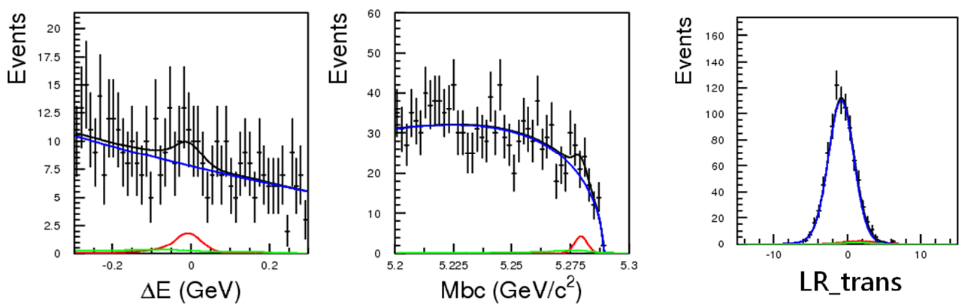

Figure 6.9: The projection plots from ensemble test in $B^{\pm} \to \eta(\gamma\gamma)K_S^0$ mode. The ΔE plot is showed with projection $M_{bc} > 5.27$ and $\mathcal{L}R > 0.7$. M_{bc} plot is showed with projection $-0.15 < \Delta E < 0.1$ and $\mathcal{L}R > 0.7$. $\mathcal{L}R$ plot is showed with projection $-0.15 < \Delta E < 0.1$ and $M_{bc} > 5.27$.

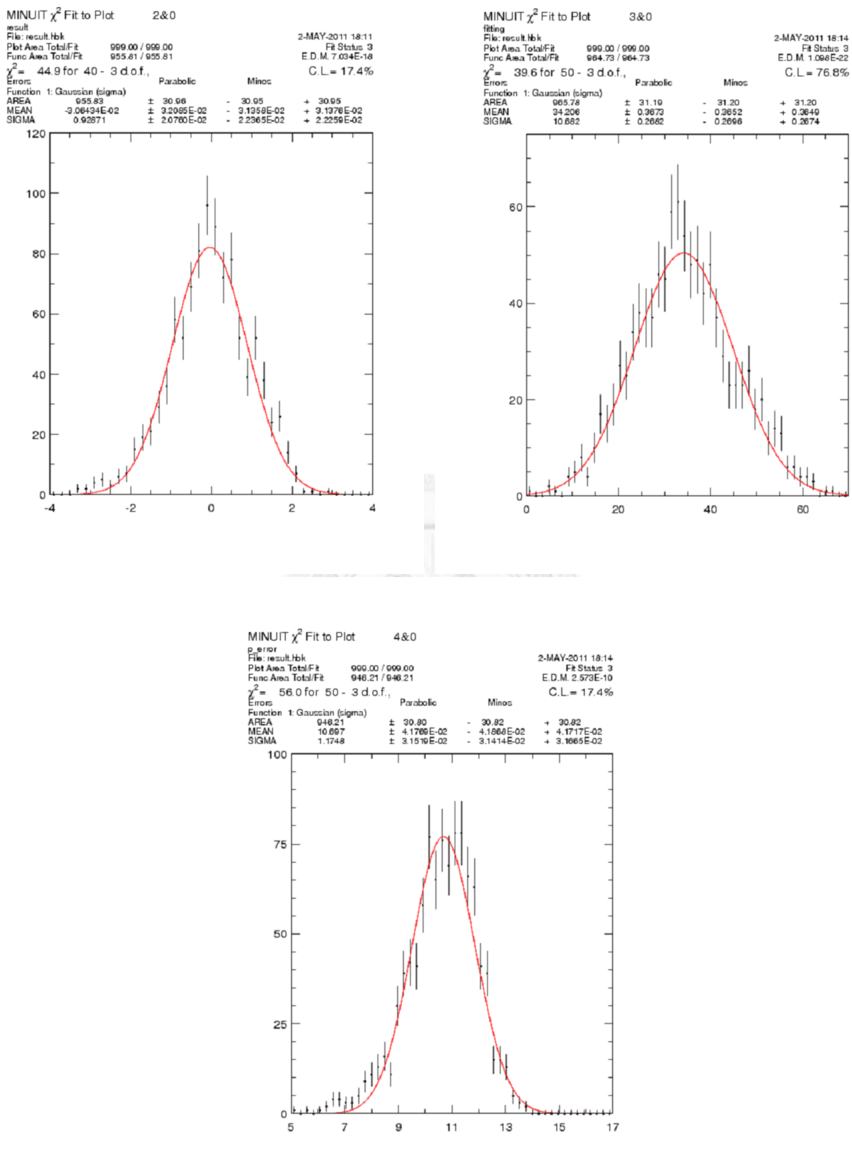

Figure 6.10: The ensemble test result in $B^0 \to \eta(\gamma\gamma)K_S^0$ mode. Pull(upper left side), yield(upper right side) and error(bottom) distribution.

6.2.4 $B^0 \to \eta(\pi^+\pi^-\pi^0)K_S^0$ Signal Yield Ensemble Test

Table 6.7: The poisson distribution mean for signal and background in our ensemble test.

	$B^0 \to \eta(\pi^+\pi^-\pi^0)K_S^0$
Signals	13
Continuum Background	2500
Rare B Background	6

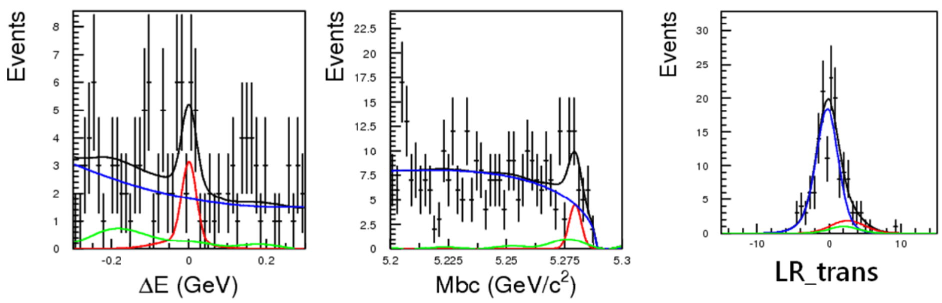

Figure 6.11: The projection plots from ensemble test in $B^0 \to \eta(\pi^+\pi^-\pi^0)K_S^0$ mode. The ΔE plot is showed with projection $M_{bc} > 5.27$ and $\mathcal{L}R > 0.7$. M_{bc} plot is showed with projection $-0.15 < \Delta E < 0.1$ and $\mathcal{L}R > 0.7$. $\mathcal{L}R$ plot is showed with projection $-0.15 < \Delta E < 0.1$ and $M_{bc} > 5.27$.

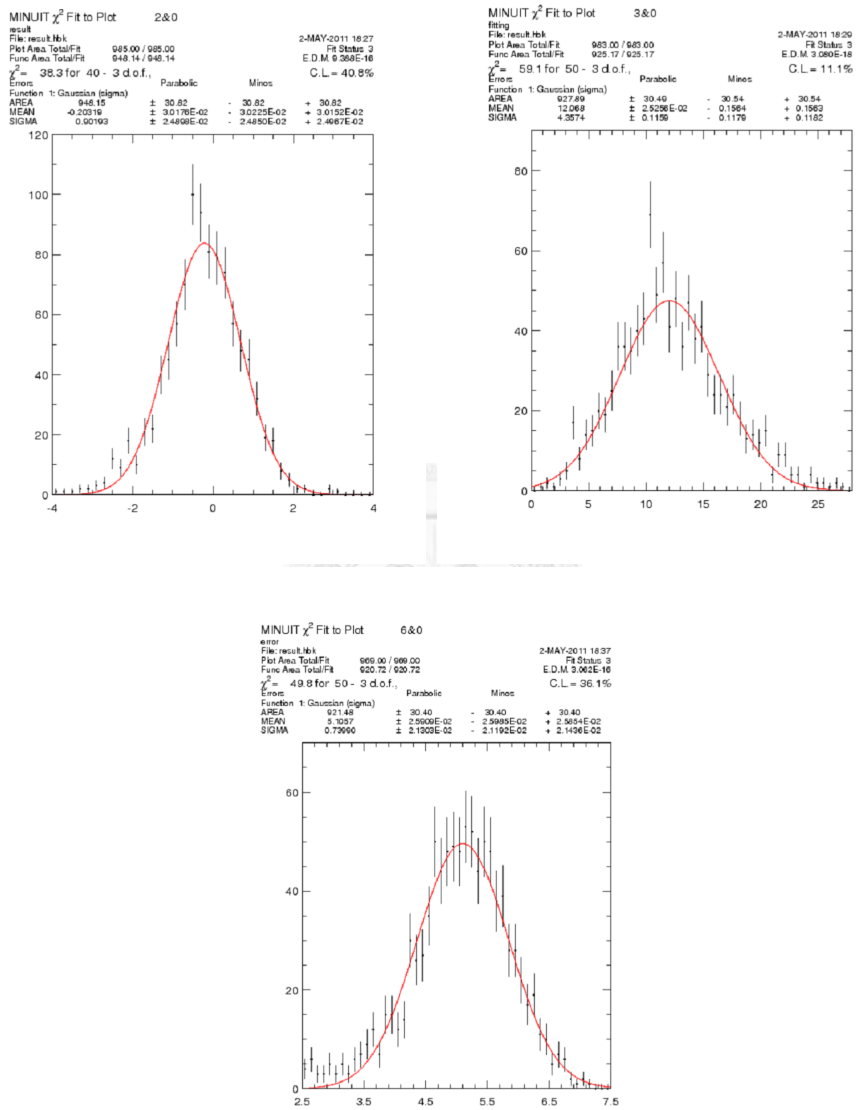

Figure 6.12: The ensemble test result in $B^0 \to \eta(\pi^+\pi^-\pi^0)K_S^0$ mode. Pull(upper left side), yield(upper right side) and error(bottom) distribution.

$B^{\pm} -> \eta(\gamma\gamma)$ K$^{\pm}$

	The Poisson distribution mean of events in sample	Fitting result	Error
Signal	240	233.13	±0.85
Continuum bck	80000	79999.94	±8.99
Rare B bck	540	557.47	±2.40

$B^{\pm} -> \eta(\gamma\gamma)$ $\pi^{\pm}$

	The Poisson distribution mean of events in sample	Fitting result	Error
Signal	435	432.71	±1.24
Continuum bck	160000	159987	±12.4
Rare B bck	290	294.66	±0.14

Figure 6.13: The fit bias of signal and background in $B^{\pm} \to \eta(\gamma\gamma)K^{\pm}$ and $B^{\pm} \to \eta(\gamma\gamma)\pi^{\pm}$ mode. Only small bias in signal and rare B background in $B^{\pm} \to \eta(\gamma\gamma)K^{\pm}$ mode.

6.2.5 $B^{\pm} \to \eta(\gamma\gamma)K^{\pm}$ and $B^{\pm} \to \eta(\gamma\gamma)\pi^{\pm}$ A_{CP} Ensemble Test

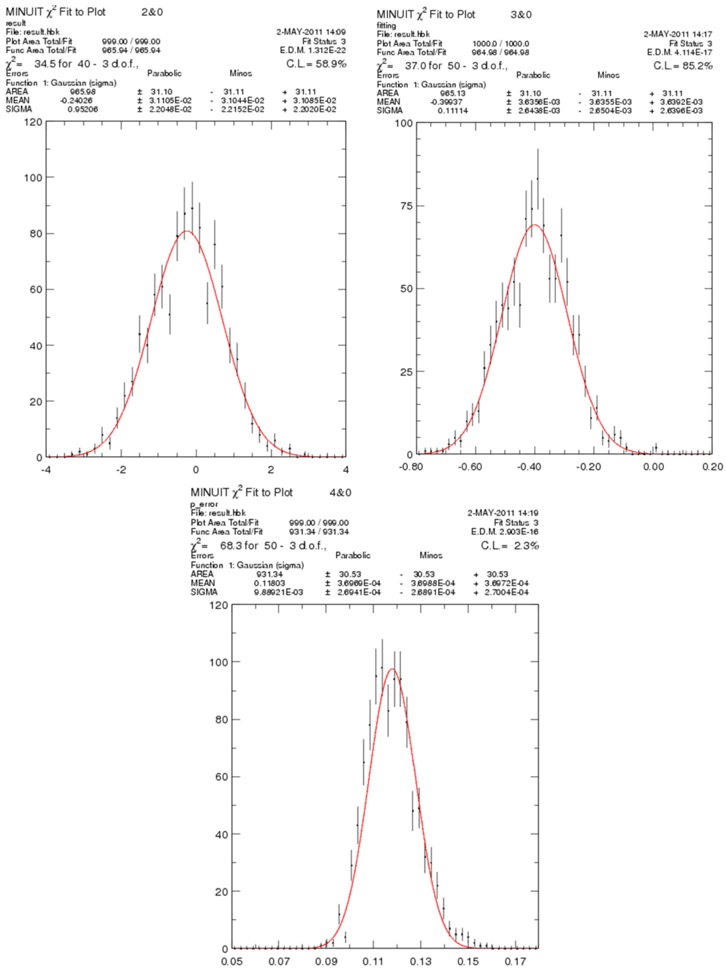

Figure 6.14: The ensemble test result in $B^{\pm} \to \eta(\gamma\gamma)K^{\pm}$ mode. Pull(upper left side), A_{CP}(upper right side) and error(bottom) distribution. The PDG value is equal to -0.37.

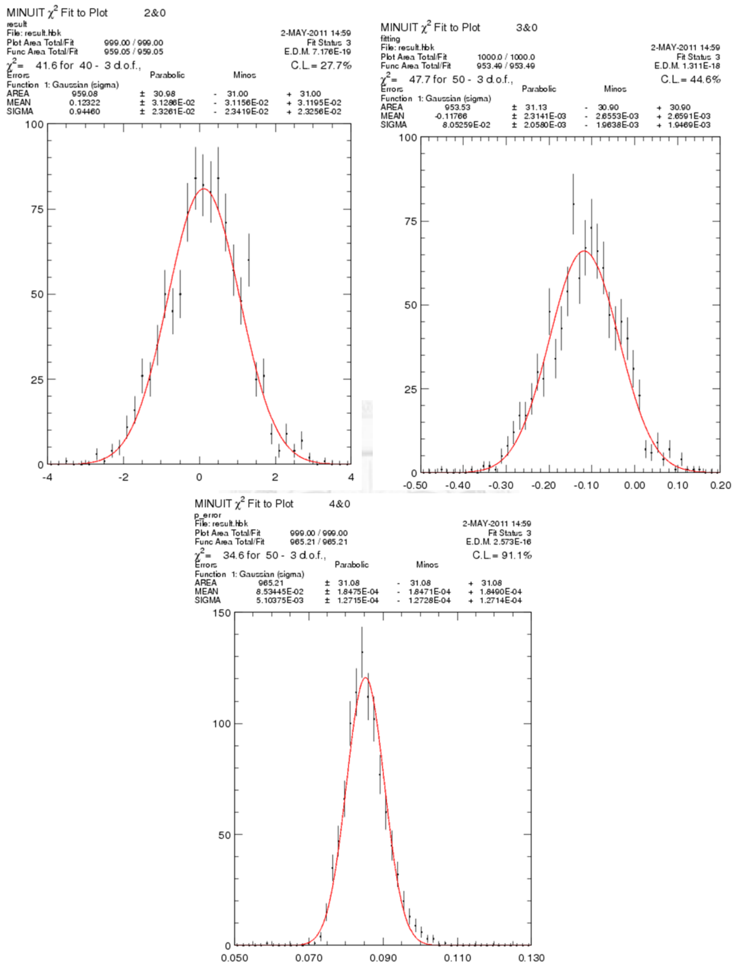

Figure 6.15: The ensemble test result in $B^{\pm} \to \eta(\gamma\gamma)\pi^{\pm}$ mode. Pull(upper left side), A_{CP}(upper right side) and error(bottom) distribution.The PDG value is equal to -0.13.

6.2.6 $B^{\pm} \to \eta(\pi^+\pi^-\pi^0)K^{\pm}$ and $B^{\pm} \to \eta(\pi^+\pi^-\pi^0)\pi^{\pm}$ A_{CP} Ensemble Test

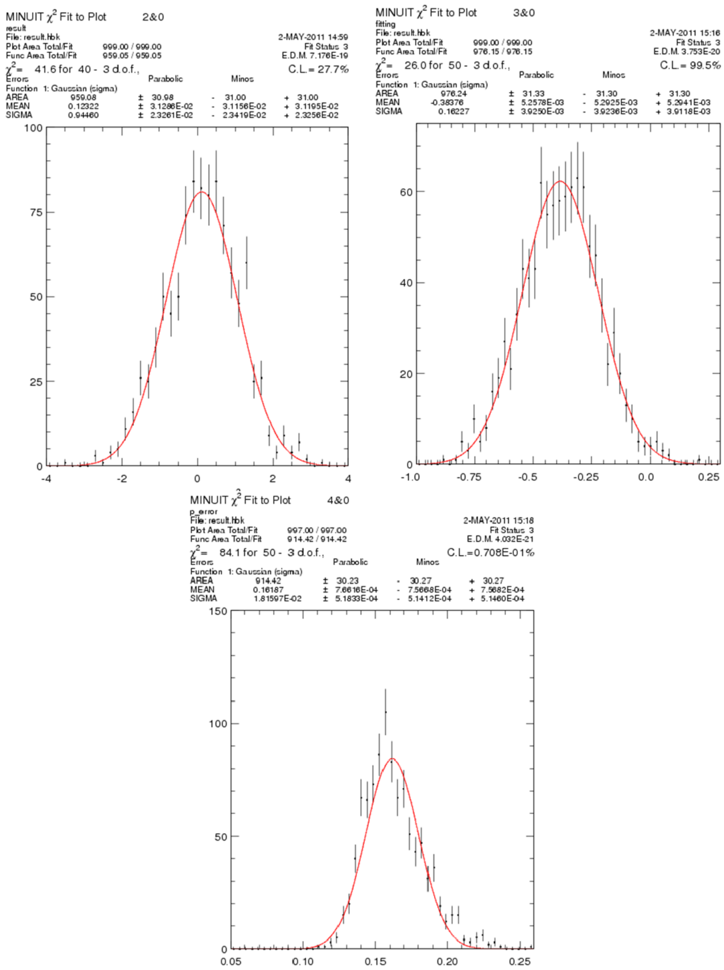

Figure 6.16: The ensemble test result in $B^{\pm} \to \eta(\pi^+\pi^-\pi^0)K^{\pm}$ mode. Pull(upper left side), A_{CP}(upper right side) and error(bottom) distribution. The PDG value is equal to -0.37.

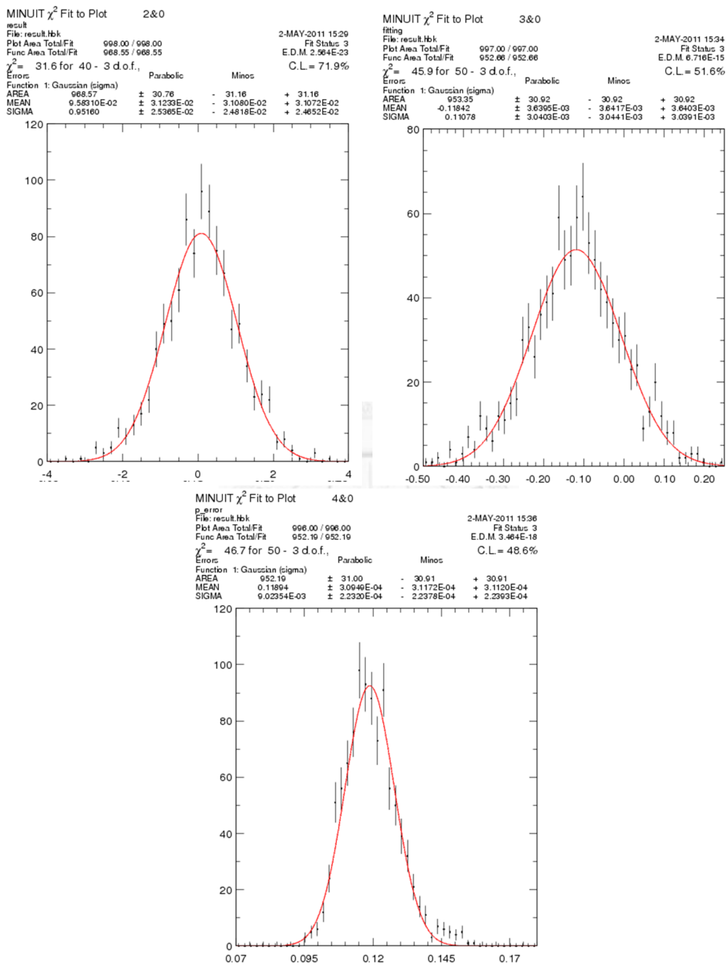

Figure 6.17: The ensemble test result in $B^{\pm} \rightarrow \eta(\pi^{+}\pi^{-}\pi^{0})\pi^{\pm}$ mode. Pull(upper left side), A_{CP}(upper right side) and error(bottom) distribution.The PDG value is equal to -0.13.

6.2.7 $B^{\pm} \to \eta(\gamma\gamma)K_S^0$ and $B^{\pm} \to \eta(\pi^+\pi^-\pi^0))K_S^0$ A_{CP} Ensemble Test

$B -> \eta(\gamma\gamma)\ \mathrm{K}_S^0$

Acp value in sample	Fitting result	Error	Bias
-0.1	-0.1212	±0.0236	-0.0212
-0.2	-0.2154	±0.0230	-0.0154
-0.3	-0.3332	±0.0221	-0.0332
-0.4	-0.4016	±0.0217	-0.0016
-0.5	-0.4771	±0.0195	-0.0229

$B -> \eta(\pi^+\pi^-\pi^0)\ \mathrm{K}_S^0$

Acp value in sample	Fitting result	Error	Bias
-0.1	-0.1049	±0.0262	-0.0049
-0.2	-0.1700	±0.0269	+0.0300
-0.3	-0.2948	±0.0252	+0.005
-0.4	-0.4160	±0.0250	-0.0160
-0.5	-0.4652	±0.0224	-0.0348

Figure 6.18: The ensemble test result in $B^0 \to \eta(\gamma\gamma)K_S^0$ and $B^0 \to \eta(\pi^+\pi^-\pi^0))K_S^0$ mode. Pull(upper left side), A_{CP}(upper right side) and error(bottom) distribution. The bias is within two sigma.

Chapter 7

Systematics Error and Efficiency Correction

The dominate error in $B \to \eta h$ mode is statistical error. We estimate our statistical errors are 11% in $\eta(\gamma\gamma)K^{\pm}$, 8% in $\eta(\gamma\gamma)\pi^{\pm}$, 16% in $\eta(\pi^+\pi^-\pi^0)K^{\pm}$, 12% in $\eta(\pi^+\pi^-\pi^0)\pi^{\pm}$, 34% in $\eta(\gamma\gamma)K_S^0$, and 40% in $\eta(\pi^+\pi^-\pi^0)K_S^0$. Our systmatics errors are about 4.5% in $\eta h^{\pm}$, 7% in ηK_S^0. The systmatics error in this analysis include the following:

- $\mathcal{L}R$ cut uncertainty : describle in section 5.1
- PID uncertainty : describle in section 5.2
- PDF uncertainty for translated $\mathcal{L}R$, M_{bc} and ΔE : Use the error of the fudge factors to vary the signal PDFs and will be given after box opening.
- Tracking uncertainty : There is 0.34% error for each charged track, which is determined from partially reconstructed D^* decay [10].
- η and π^0 uncertainty : describle in section 5.3.
- Fit bias : We have a small fit bias in $\eta(\gamma\gamma)K^{\pm}$ mode, and no bias in order modes. Therefore, we give 2.9% fit bias systmatics errors for signal yield and 2.9% for A_{CP} in $\eta(\gamma\gamma)K^{\pm}$ mode.

- K_S^0 uncertainty : The systematics error is 1.61% (For hight momentum K_S^0). Which is studied in $D^* \to \pi D^0$ and $D^0 \to K_S^0 \pi^+ \pi^+$ mode. [8].

- Uncertainty of numbers of $B\overline{B}$ pairs in real data : The systematics error is 1.37%. There is $771.581 \pm 10.566 \times 10^6$ $B\overline{B}$ pairs in real data.

- Error from MC efficiency : Given by the ratio of statistical error in the total yield of the signal MC. And is less than 0.55 % for all our ηh mode.

- Rare B PDF uncertainty : The uncertainty is given by the difference between float the rare B yield and fix to expected values.

7.1 The efficiency of $\mathcal{L}R$ cut

We calculate the $\mathcal{L}R$ of $B^+ \to \overline{D}^0 \pi^+$ candidates by using the same fisher discriminant, $cos\theta_B$ and ΔZ distribution obtained in the $B \to \eta h$ decays, and then extract the signal yields by 3-D $\mathcal{L}R - \Delta E - M_{\rm bc}$ fit and calculate the ratio with and without $\mathcal{L}R$ cut. And we use a low $\mathcal{L}R$ cut, $\mathcal{L}R > 0.2$ in all $B \to \eta h$ decay modes. The results for MC and data are list in Table 7.1. The error of efficiency listed in Table 7.1 is given by binomial error : $error = \sqrt{\frac{efficiency \times (1 - efficiency)}{N}}$, where N represents the yield without $\mathcal{L}R$ cut. And the $\mathcal{L}R$ systematic error is calculated by :$\sqrt{(ratio - 1)^2 + error_{ratio}^2}$. The control sample 3-D fitting results are showed in Fig 7.1, and 7.2 for $\mathcal{L}R > 0.2$.

Table 7.1: The $\mathcal{L}R$ cut efficiency for data and MC of the control sample.

	$\eta(\gamma\gamma)K^{\pm}$	$\eta(\gamma\gamma)\pi^{\pm}$	$\eta(\gamma\gamma)K_S^0$
Data	0.9114 ± 0.0011	0.9342 ± 0.0010	0.9295 ± 0.0010
MC	0.9106 ± 0.0009	0.9302 ± 0.0008	0.9247 ± 0.0008
Ratio $(Data/MC)$	1.0009 ± 0.0015	1.0043 ± 0.0013	1.0052 ± 0.0014
$\mathcal{L}R$ systemic error (%)	0.178	0.451	0.539

	$\eta(\pi^+\pi^-\pi^0)K^{\pm}$	$\eta(\pi^+\pi^-\pi^0)\pi^{\pm}$	$\eta(\pi^+\pi^-\pi^0)K_S^0$
Data	0.9049 ± 0.0011	0.9441 ± 0.0009	0.9285 ± 0.0010
MC	0.8998 ± 0.0009	0.9385 ± 0.0007	0.9243 ± 0.0008
Ratio $(Data/MC)$	1.0057 ± 0.0016	1.0060 ± 0.0012	1.0045 ± 0.0014
$\mathcal{L}R$ systemic error (%)	0.589	0.610	0.474

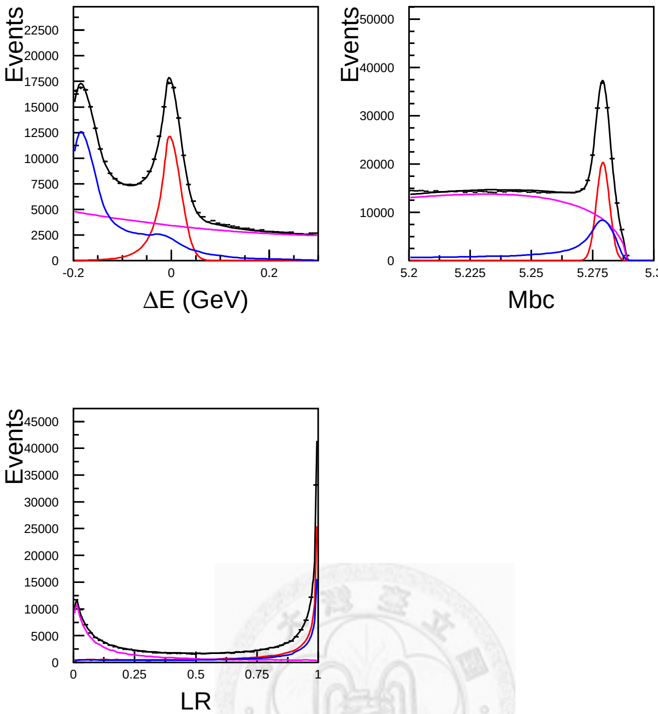

Figure 7.1: The ΔE, $M_{\rm bc}$ and $\mathcal{L}R$ distribution for $B^+ \to \overline{D}^0(K^+\pi^-\pi^0)\pi^+$ in data, no $\mathcal{L}R$ cut is required.

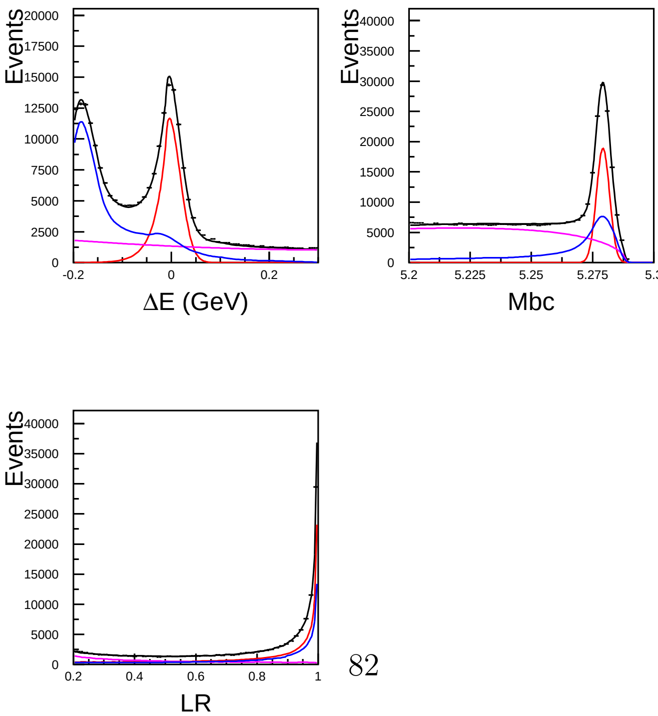

Figure 7.2: The ΔE, $M_{\rm bc}$ and $\mathcal{L}R$ distribution for $B^+ \to \overline{D}^0(K^+\pi^-\pi^0)\pi^+$ in data, $\mathcal{L}R > 0.2$ is required.

7.2 Systematics of Particle Identification

The PID efficiency and fake rate are studied by using the inclusive D^* sample via PID Group. The discrepancy between signal MC and data is corrected when calculating branching ratio. And its error will consider a part of systmatics error.

Table 7.2: The KID efficiency (%) and fake rate for $B^\pm \to \eta K^\pm$ and $B^\pm \to \eta\pi^\pm$, here $K^\pm$ and $\pi^\pm$ come from $B^\pm$. Ratio = $(Data/MC)$.

	K^+	K^-	π^+	π^-
Data eff.	83.675 ± 0.503	84.384 ± 0.526	89.341 ± 0.647	88.605 ± 0.543
MC eff.	86.998 ± 0.091	87.124 ± 0.092	92.905 ± 0.077	92.754 ± 0.077
Ratio	96.251 ± 0.920	97.065 ± 0.950	96.241 ± 1.037	95.552 ± 0.916
Data fake	0.112 ± 0.005	0.107 ± 0.005	0.069 ± 0.005	0.075 ± 0.005
MC fake	0.086± 0.001	0.085 ± 0.001	0.039 ± 0.001	0.042 ± 0.001
Ratio	131.125 ± 8.143	126.912 ± 8.363	186.411 ± 18.067	191.673 ± 16.614

Table 7.3: The KID efficiency (%) for $B \to \eta(\pi^+\pi^-\pi^0)h$. The $\pi^\pm$ efficiency comes from η.

	π^+	π^-
Data eff.	93.553 ± 0.430	93.483 ± 0.443
MC eff.	96.325 ± 0.028	96.421 ± 0.025
Ratio	97.419 ± 0.753	97.314 ± 0.765

7.3 Systmatics Error of η and π^0 Uncertainty

The systematics error comes from $\eta \to \gamma\gamma$ or $\pi^0 \to \gamma\gamma$ uncertainty is 4.0%. The uncertainty is studied in comparing the ratios of data/MC in

$D^0 \to K^-\pi^+$ and $D^0 \to K^-\pi^+\pi^0$ decays. The π^0 used to give the $\eta \to \gamma\gamma$ uncertainty is selected with same high momentum as $\eta \to \gamma\gamma$ [11] [13].

7.4 Summary of Systematics Error

Here we show the summary table of systematics error, and PDF systematics error need to be study after opening box.

Table 7.4: The summary of branching fractions systematics error (%) for each mode.

Uncertainty	$\eta(\gamma\gamma)K^{\pm}$	$\eta(\gamma\gamma)\pi^{\pm}$	$\eta(\gamma\gamma)K_S^0$
$\mathcal{L}R$ cut	0.178	0.451	0.539
PID	0.935	0.977	0.0
ΔE and M_{bc} PDF	2.30	0.5	1.78
$\mathcal{L}R$ PDF	0.6	0.5	0.32
Tracking	0.35	0.35	0.7
η mass cut	4.0	4.0	4.0
π^0 mass cut	0.0	0.0	0.0
K_S^0 selection	0.0	0.0	1.61
Number of $B\overline{B}$ pairs	1.37	1.37	1.37
MC efficiency	0.55	0.55	0.55
Rare B PDF	1.9	0.6	1.9
Total	5.0	4.5	5.0

Uncertainty	$\eta(\pi^+\pi^-\pi^0)K^{\pm}$	$\eta(\pi^+\pi^-\pi^0)\pi^{\pm}$	$\eta(\pi^+\pi^-\pi^0)K_S^0$
$\mathcal{L}R$ cut	0.589	0.610	0.474
PID	2.475	2.291	1.518
ΔE and M_{bc} PDF	0.38	0.2	0.37
$\mathcal{L}R$ PDF	0.5	0.66	0.5
Tracking	1.05	1.05	1.4
η mass cut	4.0	4.0	4.0
π^0 mass cut	4.0	4.0	4.0
K_S^0 selection	0.0	0.0	1.61
Number of $B\overline{B}$ pairs	1.37	1.37	1.37
MC efficiency	0.55	0.55	0.55
Rare B PDF	0.82	0.23	0.7
Total	6.6	6.6	6.5

Table 7.5: The summary of A_{CP} systematics error (%) for each mode.

Uncertainty	$\eta(\gamma\gamma)K^{\pm}$	$\eta(\gamma\gamma)\pi^{\pm}$	$\eta(\gamma\gamma)K_S^0$
ΔE and M_{bc} PDF	0.3	0.3	-
$\mathcal{L}R$ PDF	0.2	0.2	-
Rare B PDF	0.7	0.6	-
ΔE mean shift from high momentum π^0	0.2	0.4	-
Total	0.8	0.8	-

Uncertainty	$\eta(\pi^+\pi^-\pi^0)K^{\pm}$	$\eta(\pi^+\pi^-\pi^0)\pi^{\pm}$	$\eta(\pi^+\pi^-\pi^0)K_S^0$
ΔE and M_{bc} PDF	0.25	0.23	-
$\mathcal{L}R$ PDF	0.3	0.2	-
Rare B PDF	0.4	0.3	-
ΔE mean shift from high momentum π^0	-	-	-
Total	0.6	0.4	-

Chapter 8

Box Opening Result

In this chapter, we show the final result in real data. Both branching fraction and A_{cp} result are close to P.Chang's previous measurment. In our measurment, the A_{cp} significances reach 3 in both $B^{\pm} \to \eta K^{\pm}$ and $B^{\pm} \to \eta \pi^{\pm}$. Branching fraction significance is larger than 5 in $B^0 \to \eta K^0$.

Table 8.1: Summary table of branching fractions and other details for each decay mode. Detection efficiency ϵ_{eff} including sub-decay branching fraction, yield, fit bias, significance (Sig.), measured branching fraction (B), and A_{CP} for the $B \to \eta h$ decays. Thre first errors are statistical and the second ones are systematic.

Mode	ϵ_{eff} (%)	Yield	Bias	Sig.	$B(10^{-6})$	A_{CP}
$B^{\pm} \to \eta K^{\pm}$				13.2	$2.12^{+0.23}_{-0.22} \pm 0.11$	-0.38 ± 0.11
$\eta_{\gamma\gamma} K^{\pm}$	13.71	$201.88^{+27.08}_{-26.48}$	-6.77	10.2	$2.07 \pm 0.27 \pm 0.10$	-0.36 ± 0.13
$\eta_{3\pi} K^{\pm}$	4.94	$80.17^{+14.92}_{-13.85}$	0	8.6	$2.29^{+0.43}_{-0.40} \pm 0.15$	-0.42 ± 0.18
$B^{\pm} \to \eta \pi^{\pm}$				22.4	$4.07 \pm 0.26 \pm 0.21$	-0.19 ± 0.06
$\eta_{\gamma\gamma} \pi^{\pm}$	15.34	$480.61^{+35.06}_{-35.97}$	0	19.0	$4.24^{+0.31}_{-0.32} \pm 0.19$	-0.14 ± 0.08
$\eta_{3\pi} \pi^{\pm}$	5.44	$138.55^{+18.50}_{-17.47}$	0	12.2	$3.63 \pm 0.49 \pm 0.25$	$-0.31^{+0.13}_{-0.12}$
$B^0 \to \eta K^0$				5.4	$1.27^{+0.33}_{-0.29} \pm 0.08$	
$\eta_{\gamma\gamma} K^0$	4.15	$38.03^{+12.62}_{-11.45}$	0	4.0	$1.18^{+0.39}_{-0.35} \pm 0.06$	
$\eta_{3\pi} K^0$	1.48	$16.23^{+6.45}_{-5.43}$	0	4.1	$1.48^{+0.59}_{-0.49} \pm 0.10$	

Table 8.2: Summary table of A_{CP} in each decay mode.

Mode	Bias	Sig.	A_{CP}
$B^{\pm} \to \eta K^{\pm}$		3.8	-0.38 ± 0.11
$\eta_{\gamma\gamma} K^{\pm}$	-0.029	2.9	-0.36 ± 0.13
$\eta_{3\pi} K^{\pm}$	0	2.4	-0.42 ± 0.18
$B^{\pm} \to \eta \pi^{\pm}$		3.0	-0.19 ± 0.06
$\eta_{\gamma\gamma} \pi^{\pm}$	0	1.8	-0.14 ± 0.08
$\eta_{3\pi} \pi^{\pm}$	0	2.5	$-0.31^{+0.13}_{-0.12}$

Table 8.3: Summary table of continuum background A_{CP} in each decay mode. All of them are less than 10% of statistical error in signal A_{CP}.

Mode	A_{CP}
$\eta_{\gamma\gamma} K^{\pm}$	-0.0034 ± 0.0037
$\eta_{3\pi} K^{\pm}$	-0.0037 ± 0.0027
$\eta_{\gamma\gamma} \pi^{\pm}$	$+0.0026 \pm 0.0058$
$\eta_{3\pi} \pi^{\pm}$	-0.0125 ± 0.0044

Table 8.4: Summary table of yields of continuum background in each decay mode.

Mode	Yield
$\eta_{\gamma\gamma} K^{\pm}$	76237 ± 282
$\eta_{3\pi} K^{\pm}$	30895 ± 178
$\eta_{\gamma\gamma} \pi^{\pm}$	145935 ± 377
$\eta_{3\pi} \pi^{\pm}$	51774 ± 216
$\eta_{\gamma\gamma} K^0_S$	13325 ± 116
$\eta_{3\pi} K^0_S$	5528 ± 74

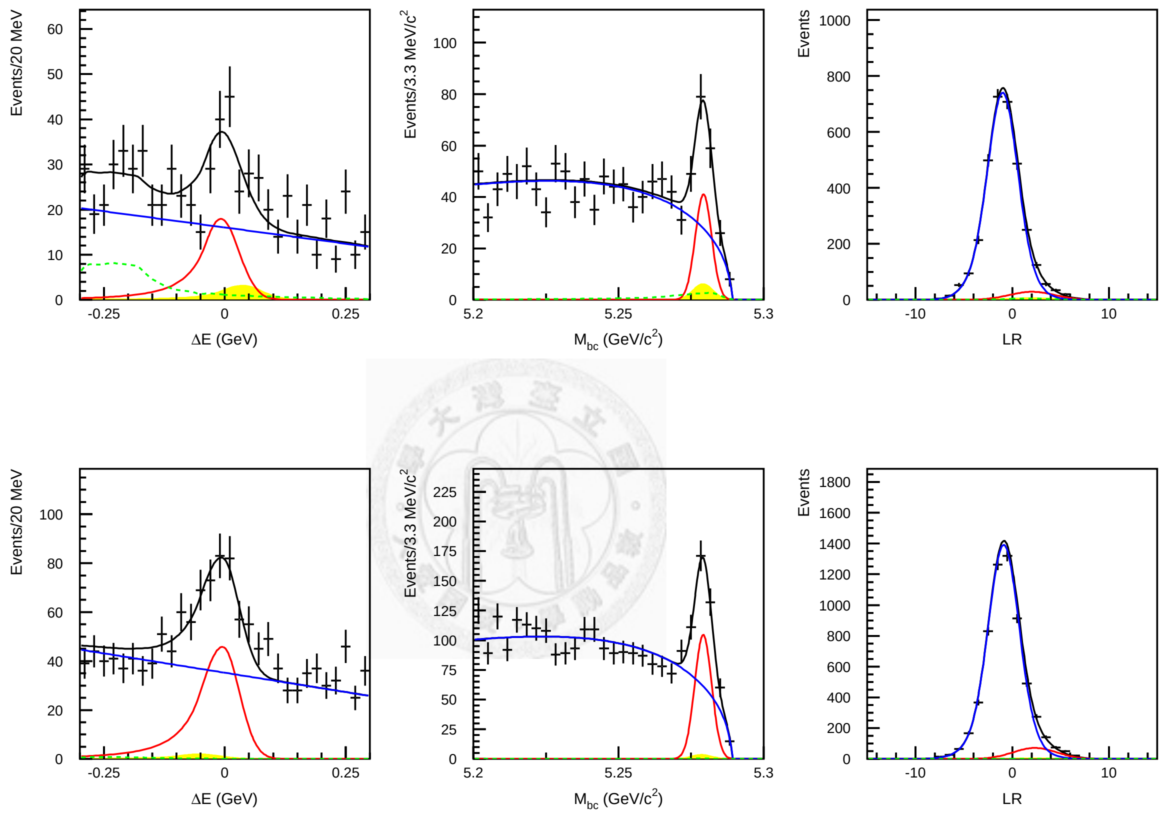

Figure 8.1: The projection plots from real data in $B^{\pm} \to \eta(\gamma\gamma)K^{\pm}$(top) and $B^{\pm} \to \eta(\gamma\gamma)\pi^{\pm}$(bottom). The red line is signal PDF, blue line is continuum background, green dashed line for rare B and yellow region for freedacross. The ΔE plot is showed with projection $M_{bc} > 5.27$ and $\mathcal{L}R > 1.95$. M_{bc} plot is showed with projection $-0.1 < \Delta E < 0.08$ and $\mathcal{L}R > 1.95$. $\mathcal{L}R$ plot is showed with projection $-0.1 < \Delta E < 0.08$ and $M_{bc} > 5.27$.

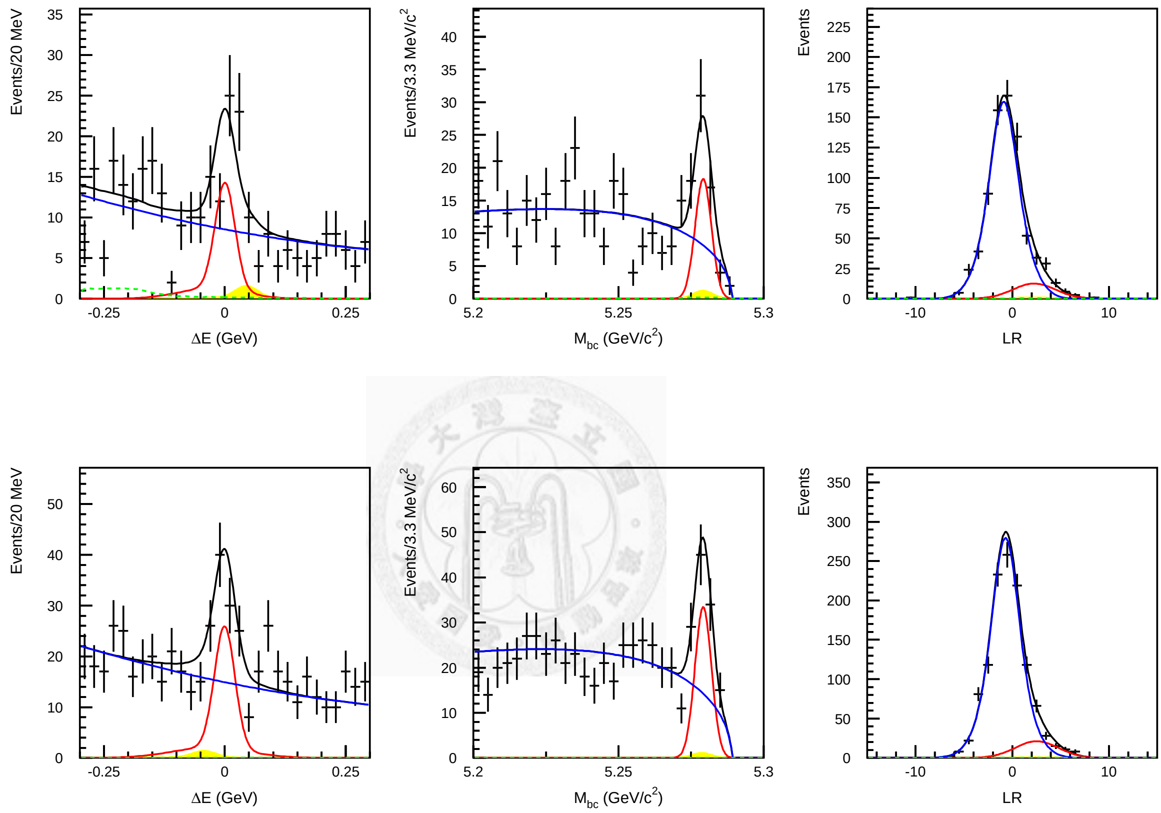

Figure 8.2: The projection plots from real data in $B^{\pm} \to \eta(\pi^{+}\pi^{-}\pi^{0})K^{\pm}$(top) and $B^{\pm} \to \eta(\pi^{+}\pi^{-}\pi^{0})\pi^{\pm}$(bottom). The red line is signal PDF, blue line is continuum background, green dashed line for rare B and yellow region for freedacross. The ΔE plot is showed with projection $M_{bc} > 5.27$ and $\mathcal{L}R > 1.95$. M_{bc} plot is showed with projection $-0.05 < \Delta E < 0.05$ and $\mathcal{L}R > 1.95$. $\mathcal{L}R$ plot is showed with projection $-0.05 < \Delta E < 0.05$ and $M_{bc} > 5.27$.

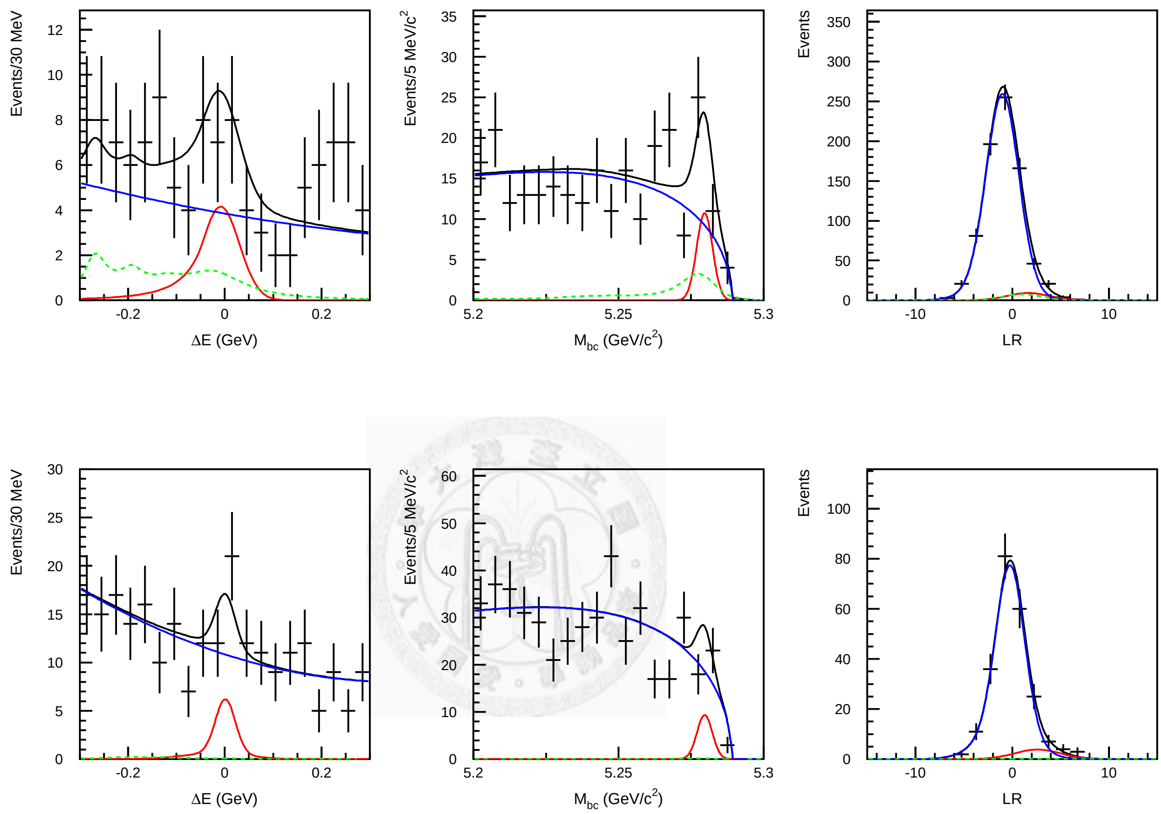

Figure 8.3: The projection plots from real data in $B^0 \to \eta(\gamma\gamma)K_S^0$(top). The red line is signal PDF, blue line is continuum background, green dashed line for rare B. The ΔE plot is showed with projection $M_{bc} > 5.27$ and $\mathcal{L}R > 1.1$. M_{bc} plot is showed with projection $-0.1 < \Delta E < 0.08$ and $\mathcal{L}R > 1.1$. $\mathcal{L}R$ plot is showed with projection $-0.1 < \Delta E < 0.08$ and $M_{bc} > 5.27$. And the projection plots from real data in $B^0 \to \eta(\pi^+\pi^-\pi^0)K_S^0$(bottom). The ΔE plot is showed with projection $M_{bc} > 5.27$ and $\mathcal{L}R > 0.51$. M_{bc} plot is showed with projection $-0.05 < \Delta E < 0.05$ and $\mathcal{L}R > 0.51$. $\mathcal{L}R$ plot is showed with projection $-0.05 < \Delta E < 0.05$ and $M_{bc} > 5.27$.

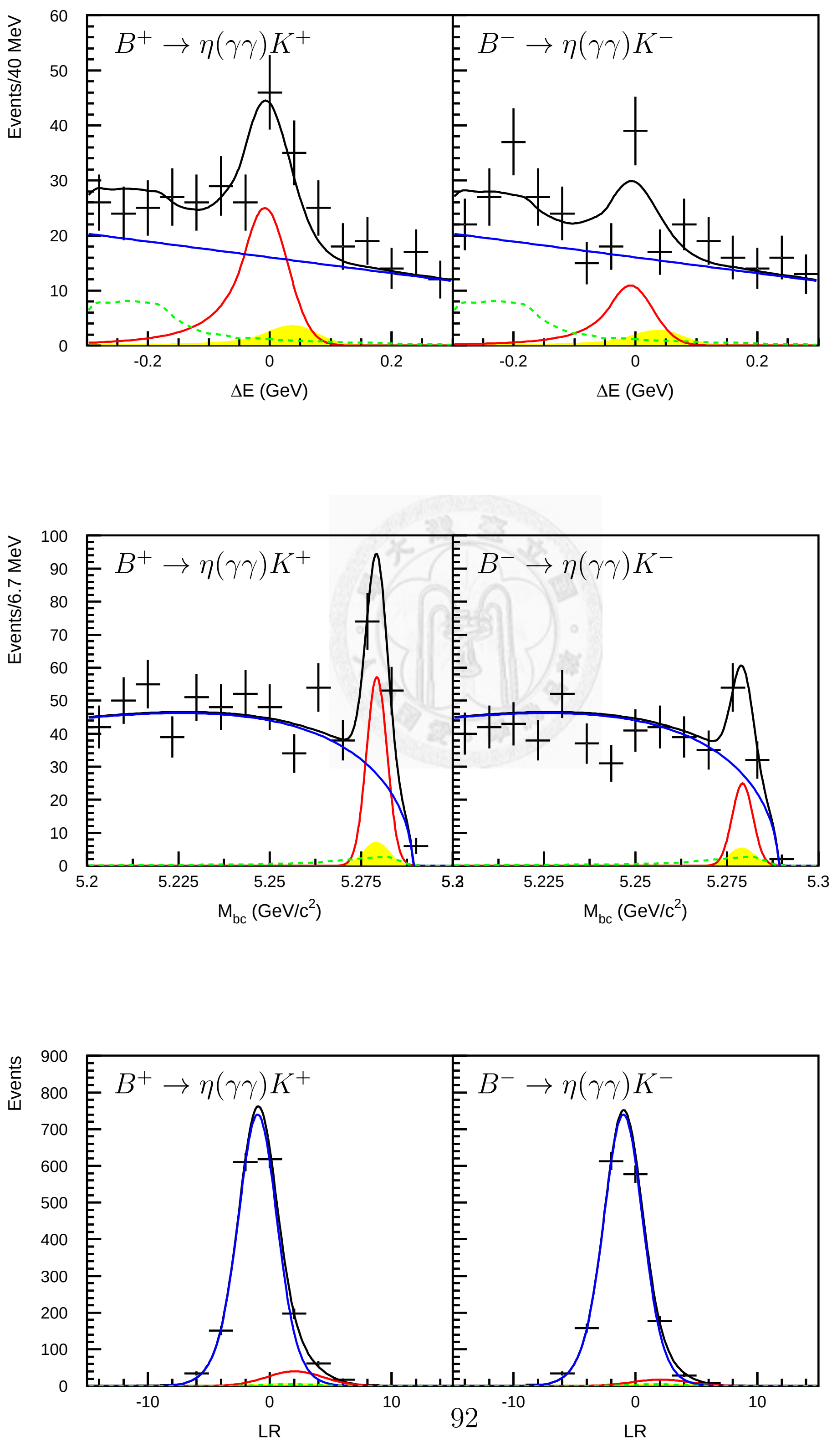

Figure 8.4: The projection plots in $B^+ \to \eta(\gamma\gamma)K^+$(left) and $B^- \to \eta(\gamma\gamma)K^-$(right).

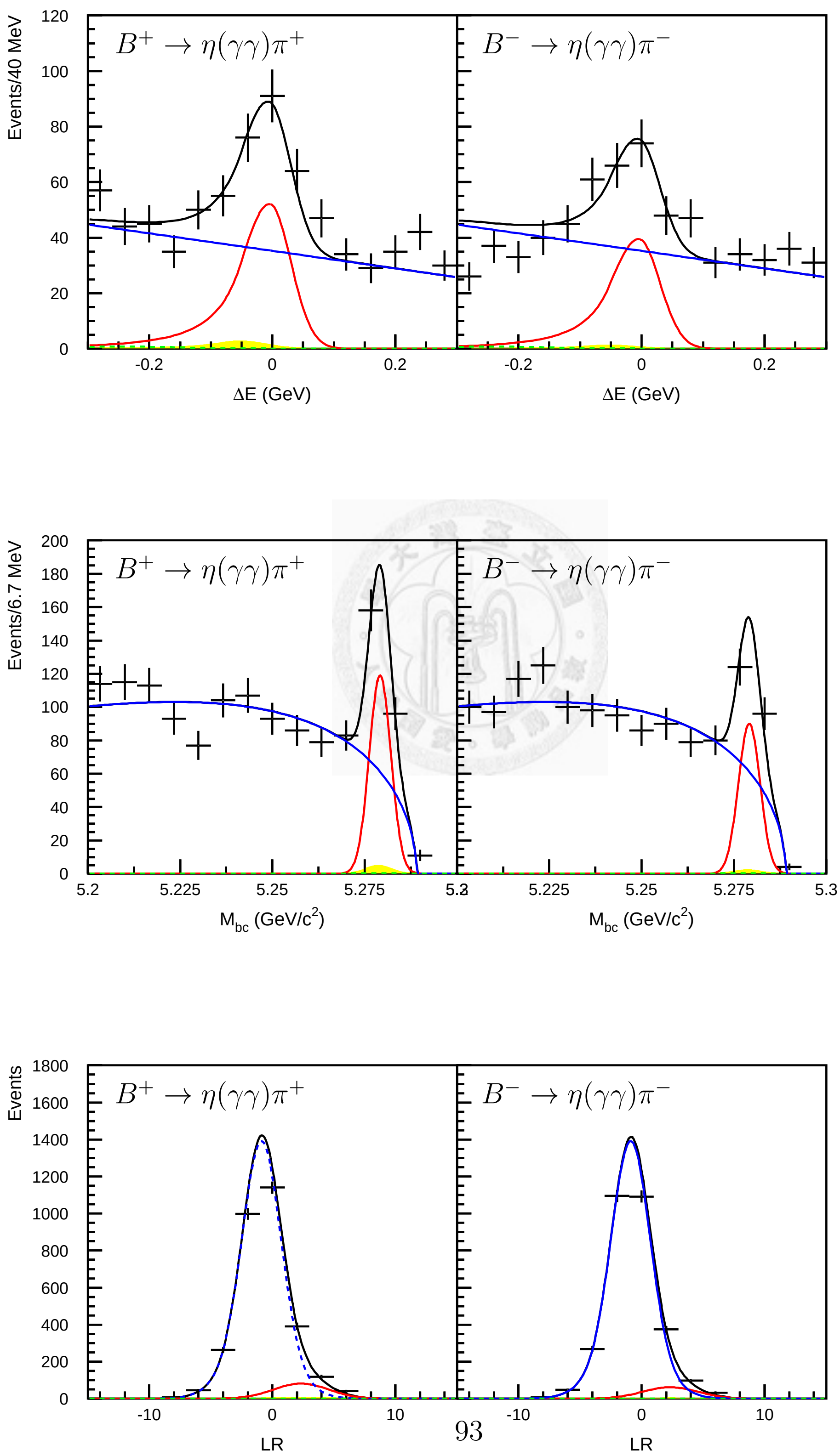

Figure 8.5: The projection plots in $B^+ \to \eta(\gamma\gamma)\pi^+$(left) and $B^- \to \eta(\gamma\gamma)\pi^-$(right).

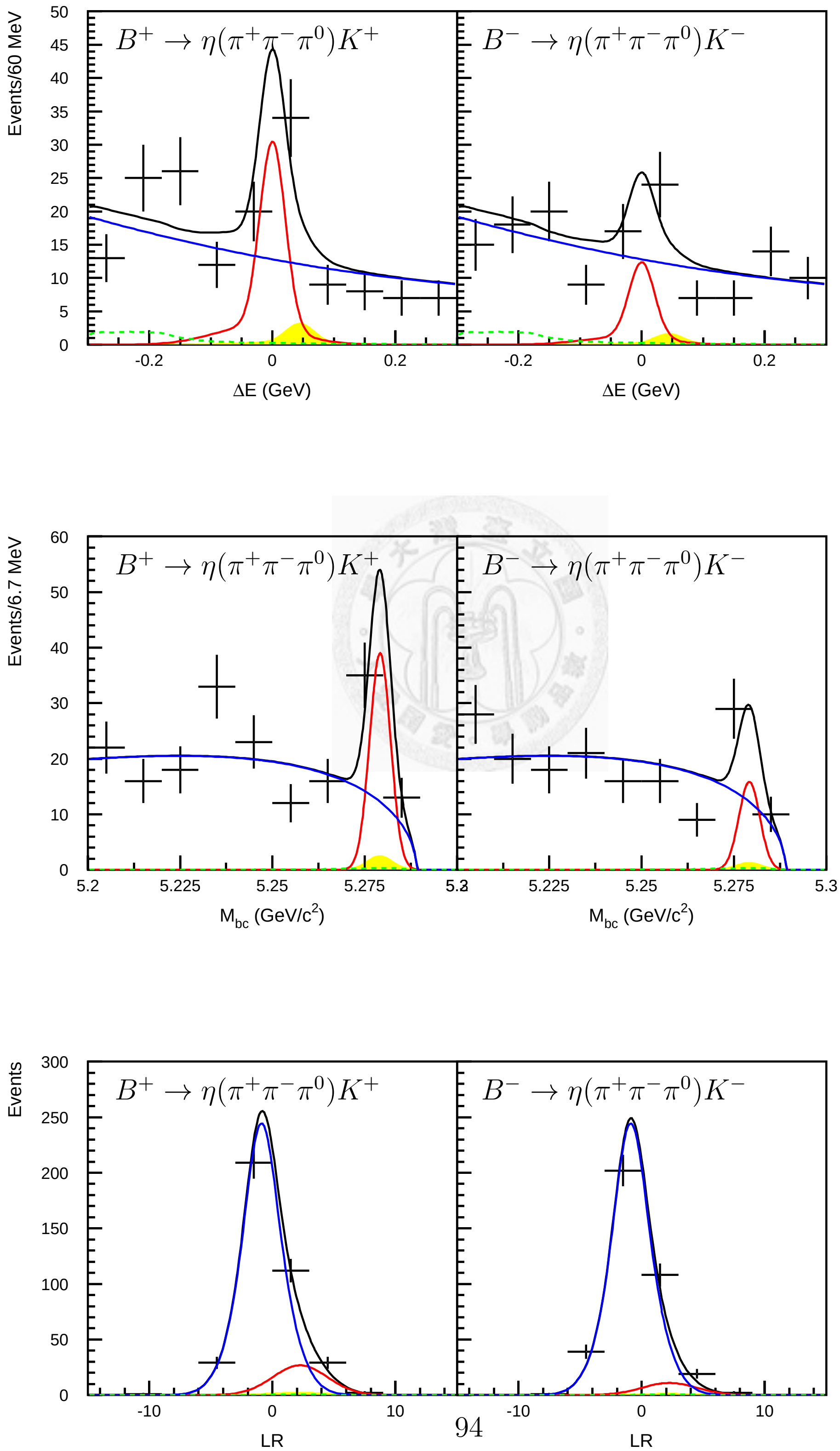

Figure 8.6: The projection plots in $B^+ \to \eta(\pi^+\pi^-\pi^0)K^+$(left) and $B^- \to \eta(\pi^+\pi^-\pi^0)K^-$(right).

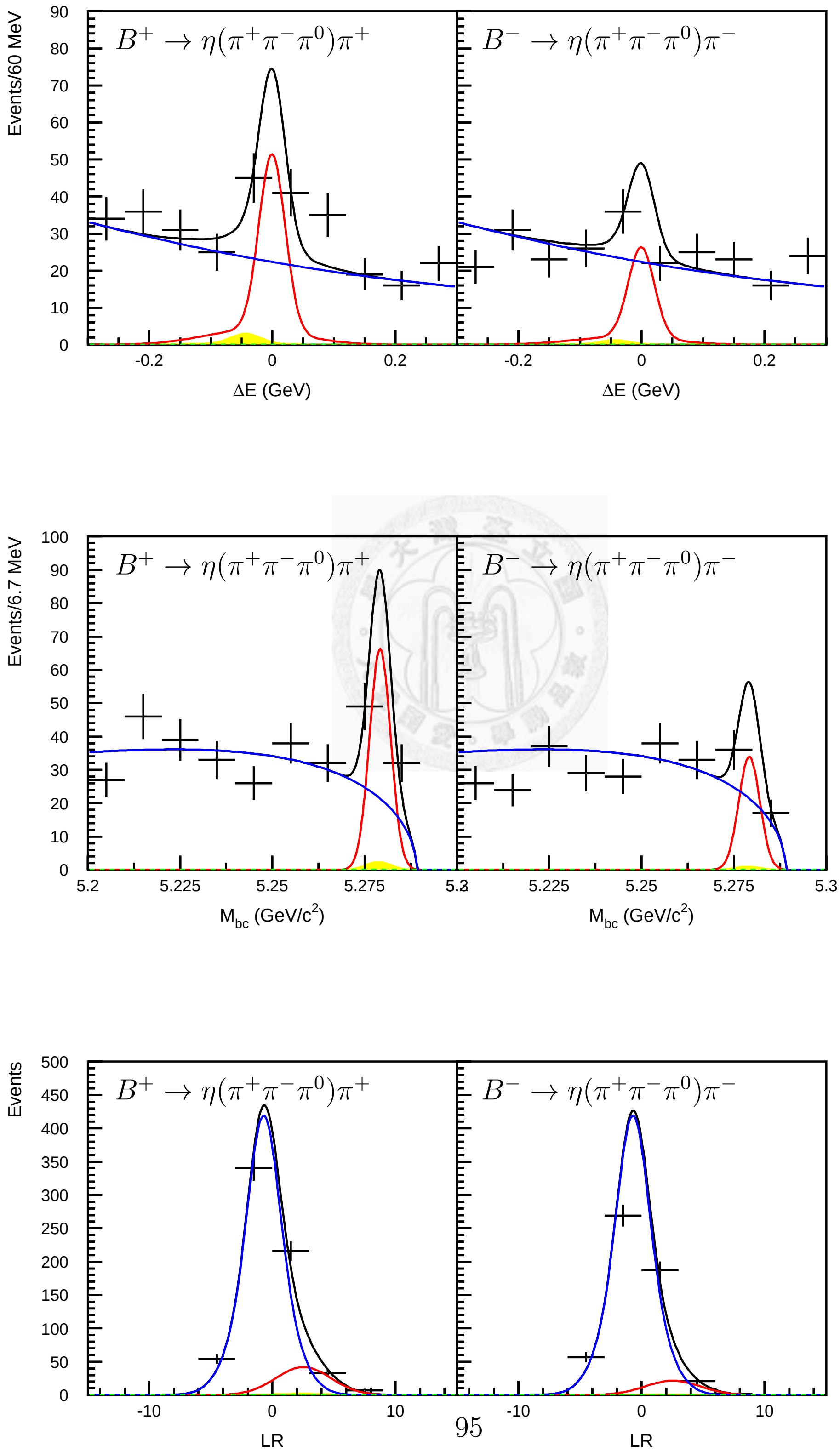

Figure 8.7: The projection plots in $B^+ \to \eta(\pi^+\pi^-\pi^0)\pi^+$(left) and $B^- \to \eta(\pi^+\pi^-\pi^0)\pi^-$(right).

Appendix A

Figure Of Merit

The Figure of Merit (F.O.M.), defined as $N_S/\sqrt{N_S + N_B}$, where N_S and N_B denote the expected total signal and background yields in the signal box.

We calculate N_S by

$$N_S = N_{B\overline{B}} \times \mathcal{B}F_{P.D.G.} \times \epsilon_{\mathrm{MC}}$$

And calculate N_B by

$$N_B = \frac{region2}{region1} \times region3$$

region1, region2 and region3 denote the number of events in those data side-band regions.

Here shows the way to do the The $\mathcal{L}R$ cut selection in $B^{\pm} \to \eta K^{\pm}$ decay mode.

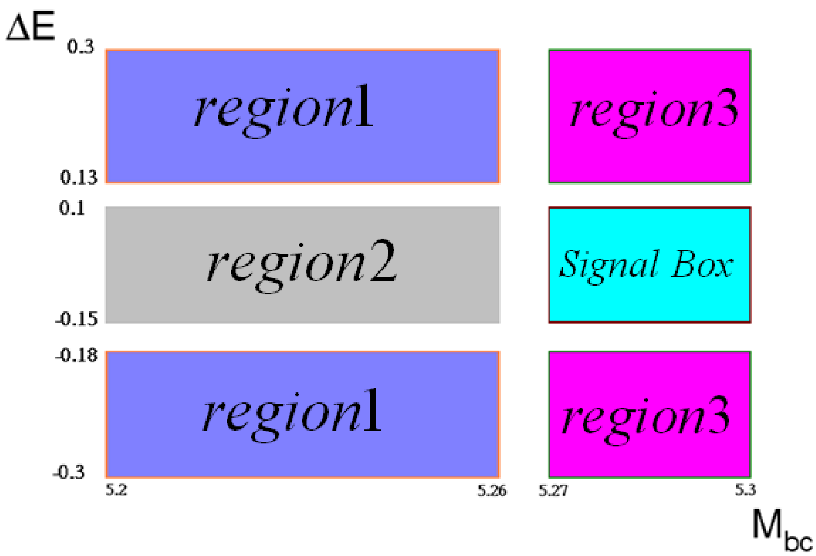

Figure A.1: The diagram of different regions in $B^{\pm} \to \eta K^{\pm}$ decay mode's sample box.

For the $B^{\pm} \to \eta K^{\pm}$ decay mode, we sperate six $q_B \times q \times r$ bins from -1 $\sim$ 1. The $\mathcal{L}R$ cut selections for each $q_B \times q \times r$ bins in 2D fit is optimized by maximizing the statistical significance ,Total Figure of Merit.

$$\text{Total F.O.M.}=\sum_{i=1}^{6} \frac{N_{S,i}}{\sqrt{N_{S,i}+N_{B,i}}}$$

where i denotes the six $q_B \times q \times r$ bins.

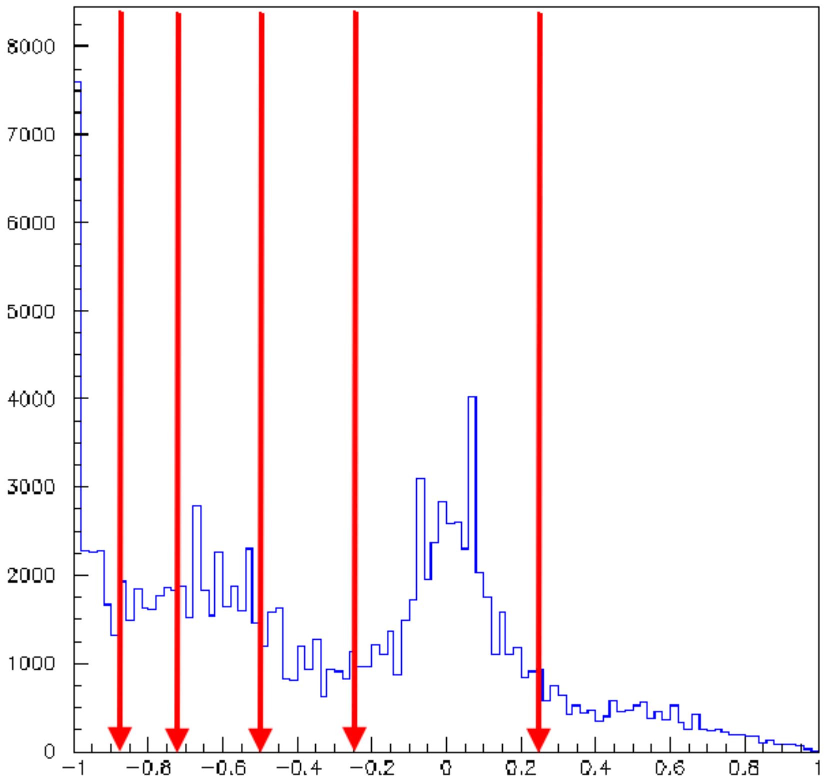

Figure A.2: The distribution of $q_B \times q \times r$ in $B^{\pm} \to \eta K^{\pm}$ decay mode.

Table A.1: Table A.1: The summarization of $\mathcal{L}R$ cuts in each $q_B \times q \times r$ bins in $B^{\pm} \to \eta K^{\pm}$ decay mode.

$q_B \times q \times r$	$\mathcal{L}R$ cuts
$-1 \sim -0.875$	0.5
$-0.875 \sim -0.75$	0.85
$-0.75 \sim -0.5$	0.85
$-0.5 \sim -0.25$	0.9
$-0.25 \sim 0.25$	0.95
$0.25 \sim 1$	0.95
Total N_S	148.12
Total N_B	341.67
Total $F.O.M.$	6.693
Removed qq background	97.76 %
Retaind Signal	55.08 %

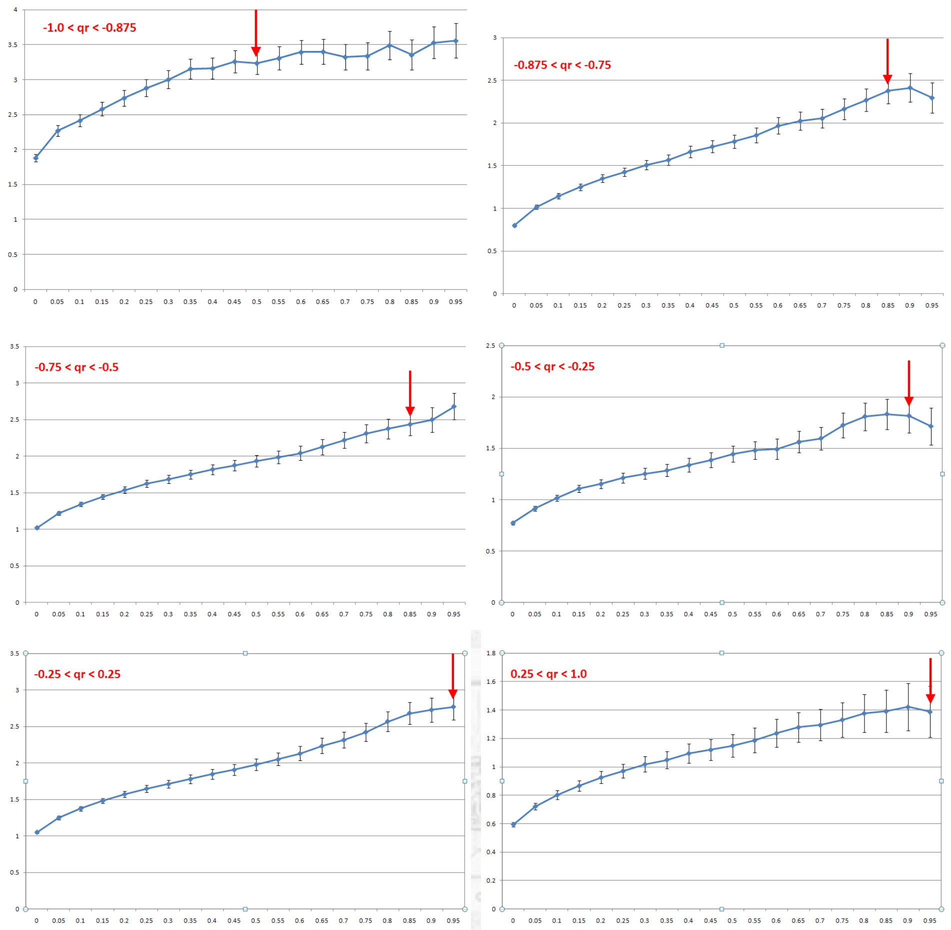

Figure A.1: Figure A.3: The F.O.M. distribution in different $q_B \times q \times r$ bins from $B^{\pm} \to \eta K^{\pm}$ decay, The red arrows show the $\mathcal{L}R$ cut selections.

Appendix B

The Translated $\mathcal{L}R$

In order to describe the likelihood ratio with analytical function. We translate the $\mathcal{L}R$ with $Trans(\mathcal{L}R) = log(\frac{\mathcal{L}R - lb}{up - \mathcal{L}R})$ provided by Gagan Mohanty. Here up is the upper bound which is equal to 1.0, and lb means the lower bound which is equal to our LR cuts(0.2).

Our translate function is $Trans(\mathcal{L}R) = log(\frac{\mathcal{L}R - 0.2}{1.0 - \mathcal{L}R})$. Its first order differential is always larger than zero when $0.2 < \mathcal{L}R < 1.0$. So, the translate function is an injective function when $0.2 < \mathcal{L}R < 1.0$. And the probability for each value will not change if the translate function is an injective function.

After the translation our signal and background likelihood ratio could be fit well with one Gaussian or two Gaussian. We also translate the $\mathcal{L}R$ in our control sample $B^+ \to \overline{D^0}\pi^+$ to study the fudge factors of the translated $\mathcal{L}R$. So, we could calibrate and give systematic error for the translated $\mathcal{L}R$ between real data and signal. The translate function also give a better resolution in $0.8 < \mathcal{L}R < 1.0$ ($0.2 < \mathcal{L}R < 0.4$) which include most of signal(continuum background). Therefore, we could describe the probability better with equal bins after translated.

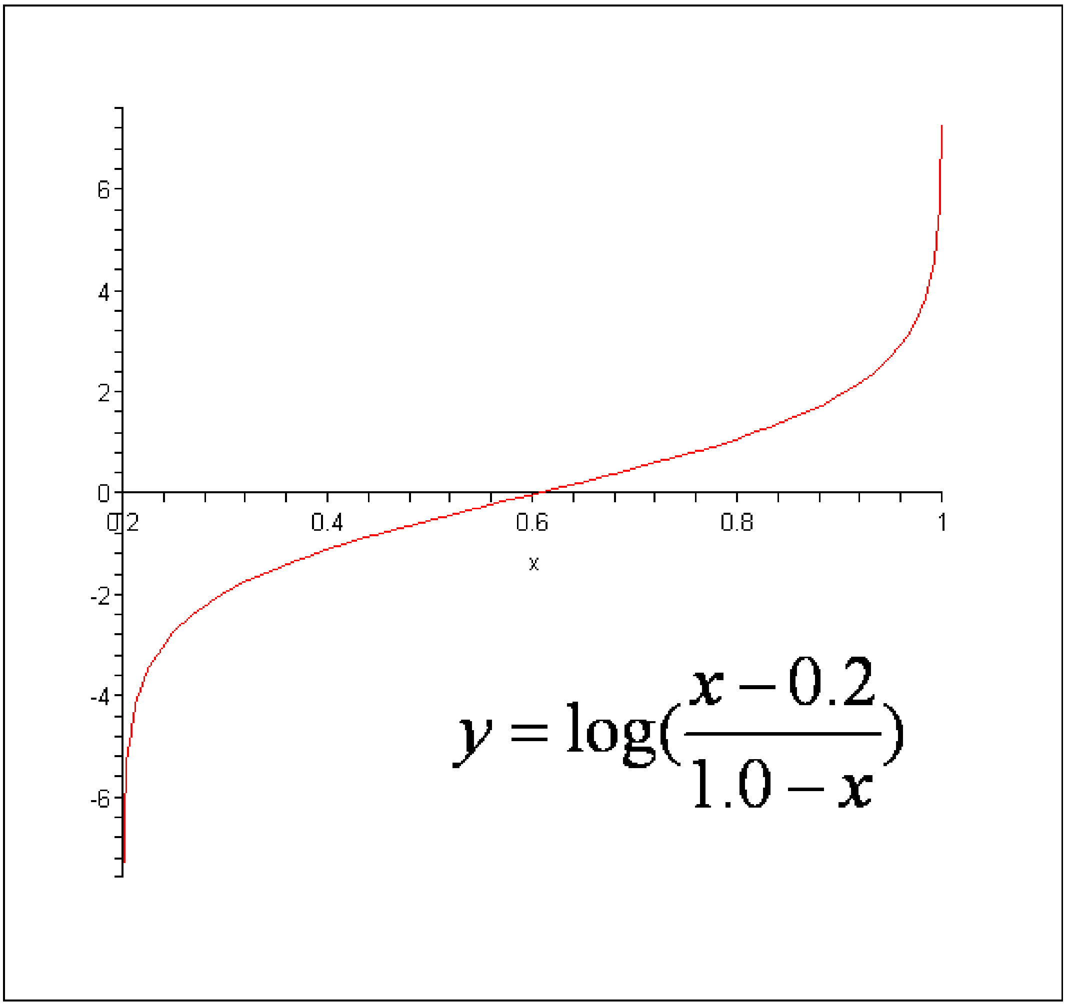

Figure B.1: The translate function. First order differential is larger than zero when $0.2 < x < 1.0$. Also give a better resolution in $0.8 < x < 1.0$ and $0.2 < x < 0.4$ after translated.

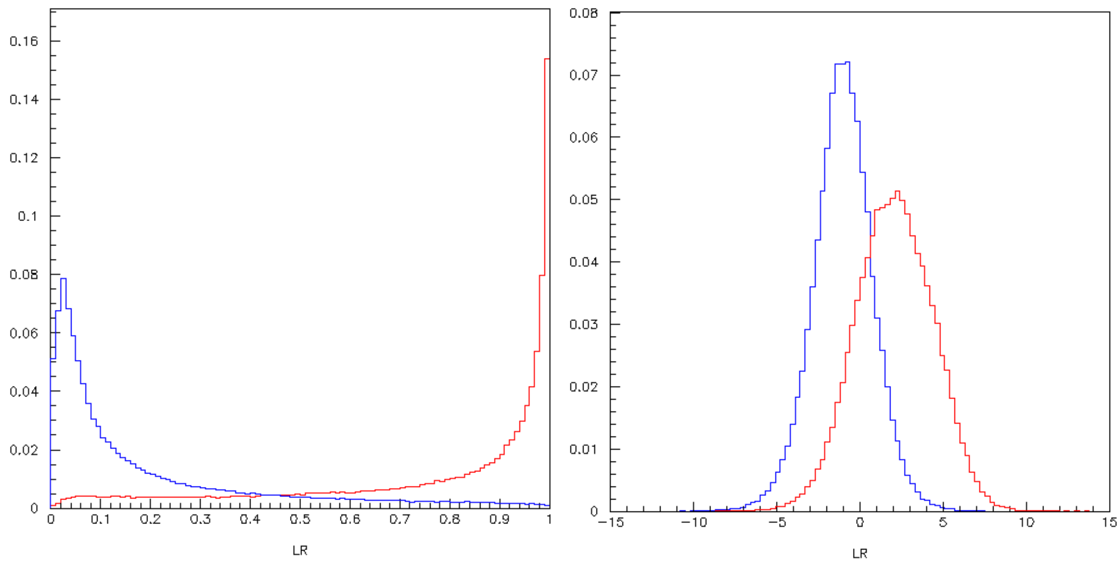

Figure B.2: The $\mathcal{L}R$(left) and the translated $\mathcal{L}R$(right) in $B^{\pm} \to \eta(\gamma\gamma)K^{\pm}$ decay. The red line shows the signal and blue line stands for countinuum background.

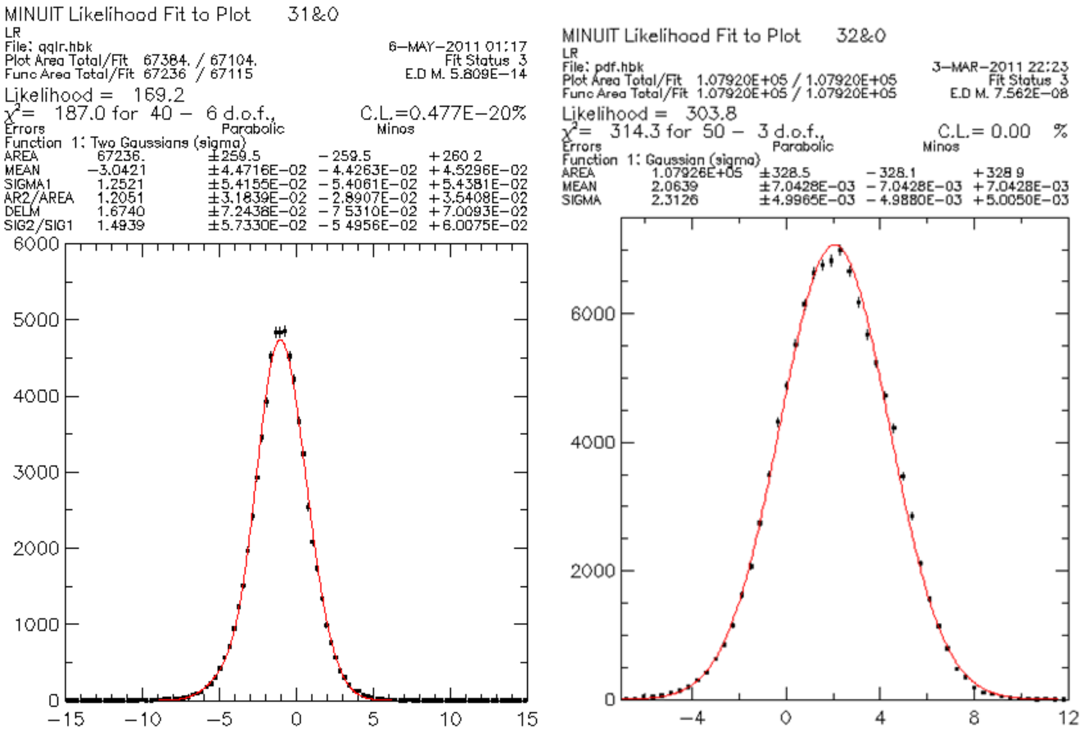

Figure B.3: Describe the translated $\mathcal{L}R$ of $B^{\pm} \to \eta(\gamma\gamma)K^{\pm}$ countinuum background with two Gaussian(left). Describe the translated $\mathcal{L}R$ of $B^{\pm} \to \eta(\gamma\gamma)K^{\pm}$ signal with one Gaussian(right).

Appendix C

The modify M_{bc}

In the Belle detector, the resolution of charged particles is better than photons. Therefore, not only the ΔE and reconstructed mass width become larger but is also case correlation problem when reconstructe particles with photon final state. So, Deb Mohapatra and Nakao-San provide a new M_{bc} (the modify M_{bc}) which is replace the photon energy with the calculated value in $B \to K^*\gamma$ study [9].

The typical M_{bc} is defined by: M_{bc}=$\sqrt{E_{beam}^2 - P_{recon}^2}$
E_{beam}, $E_{recon}$and P_{recon} are the beam energy,the reconstructed energy and the reconstructed momentum

The modify M_{bc} in $B \to \eta h$ study is defined by:

$$M_{bc}{=}\sqrt{E_{beam}^2 - (\overrightarrow{P_h} + \frac{\overrightarrow{P_\eta}}{|P_\eta|}\sqrt{(E_{beam} - E_h)^2 - M_\eta})^2}.$$

Where P_h is the $K^\pm, \pi^\pm$ or K_S^0 momentum.

The modify M_{bc} in our control sample $B^+ \to \overline{D^0}\pi^+$ study is defined by:

$$M_{bc}{=}\sqrt{E_{beam}^2 - (\overrightarrow{P_\pi} + \frac{\overrightarrow{P_{\overline{D^0}}}}{|P_{\overline{D^0}}|}\sqrt{(E_{beam} - E_{\pi^+})^2 - M_{\overline{D^0}}})^2}.$$

Where P_π is the π^+ momentum.

The modify M_{bc} provide a better M_{bc} resolution when one or more final states is high energy photons, such as : $B^\pm \to \eta(\gamma\gamma)K^\pm$ and $B^\pm \to \eta(\gamma\gamma)\pi^\pm$ decays. And provide a same M_{bc} resolution as the typical M_{bc} in $B \to \eta(\pi^+\pi^-\pi^0)h$ and $B^+ \to \overline{D^0}\pi^+$ decays. The modify M_{bc} also reduce the correlation between ΔE and M_{bc} in $B \to \eta(\gamma\gamma)h$ decays, and lead us to use non-correlated PDFs to describe the signal.

In the $B \to \eta(\gamma\gamma)h$ and $B \to \eta(\pi^+\pi^-\pi^0)h$ decays, most of the rare B background come from three-body decays. The B mesons reconstruction in rare B background should miss one or more final state particles. The photons energy loss are always overestimated in modify M_{bc} for the rare B background. Therefore, the modify M_{bc} is better than the typical M_{bc} in seperate the signal and rare B background. (For example: one of our rare B background is $B \to \eta K^*$ decay, and we should miss a pion in $B^\pm \to \eta(\gamma\gamma)K^\pm$ reconstruction, and the η energy loss will be overestimated in modify M_{bc}.) Here we use the modify M_{bc} in all our $B \to \eta h$ study.

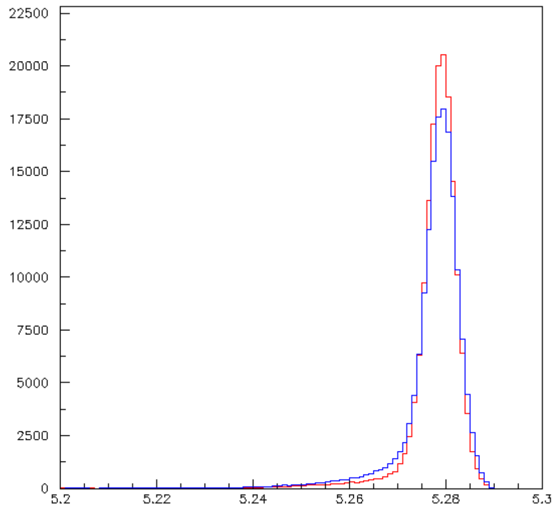

Figure C.1: The modify M_{bc}(red) and typical M_{bc}(blue) in $B^{\pm} \to \eta(\gamma\gamma)K^{\pm}$ signal MC. Better resolution is provided by the modify M_{bc}.

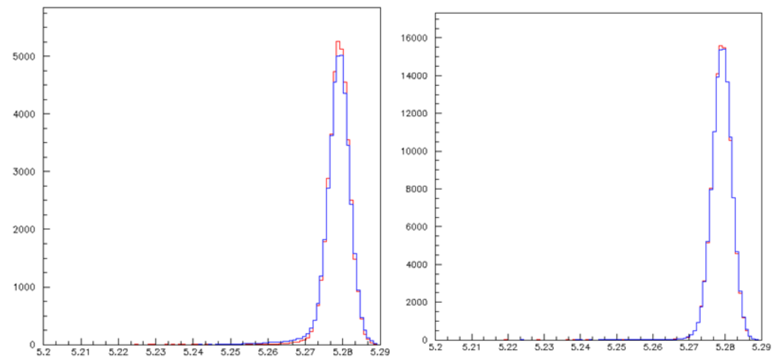

Figure C.2: The modify M_{bc}(red) and typical M_{bc}(blue) in $B^{\pm} \to \eta(\pi^{+}\pi^{-}\pi^{0})K^{\pm}$(left) and $B^{+} \to \overline{D^{0}}\pi^{+}$(right) signal MC.

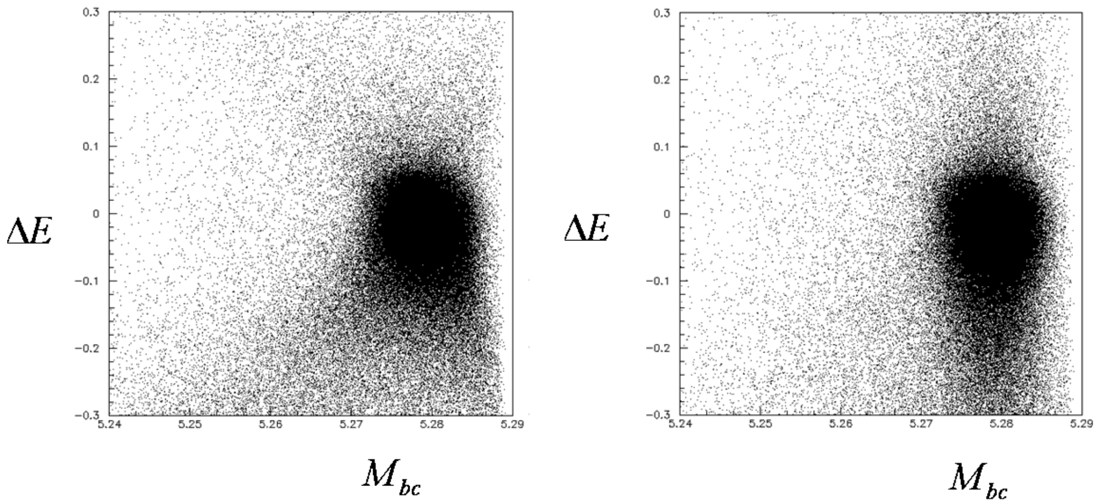

Figure C.3: The modify ΔE and typical M_{bc} scatter plot(left), ΔE and modify M_{bc} scatter plot(right). Correlation is reduced in modify M_{bc}.

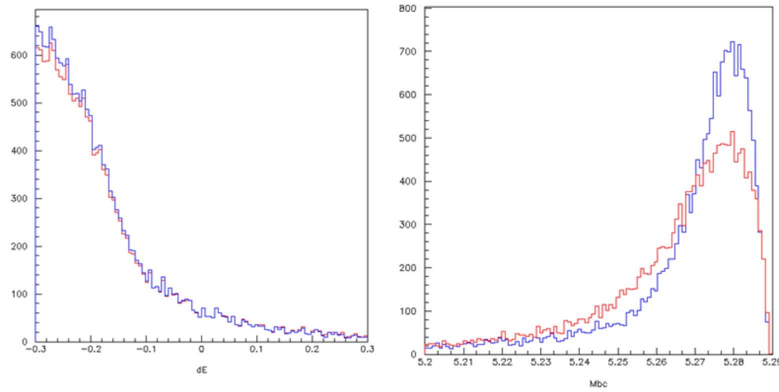

Figure C.4: The ΔE(left) and M_{bc}(right) distributions in $B^{\pm} \to \eta(\gamma\gamma)K^{\pm}$ rare B background, The red one is from modify M_{bc} and blue one is typical M_{bc}. The modify M_{bc} provide a better seperation between signal and rare B background.

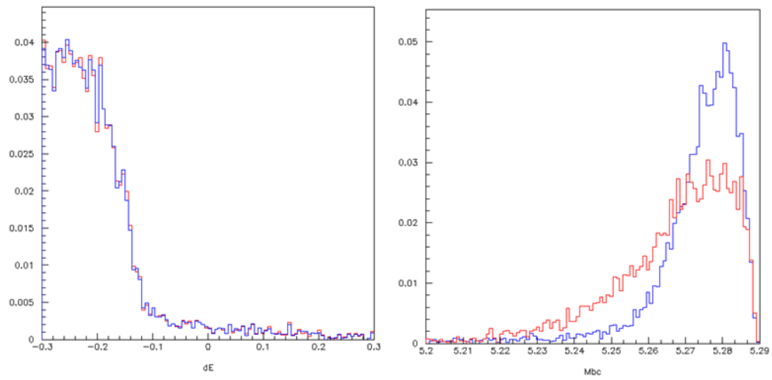

Figure C.5: The ΔE(left) and M_{bc}(right) distributions in $B^{\pm} \to \eta(\pi^+\pi^-\pi^0)K^{\pm}$ rare B background, The red one is from modify M_{bc} and blue one is typical M_{bc}. The modify M_{bc} provide a better seperation between signal and rare B background.

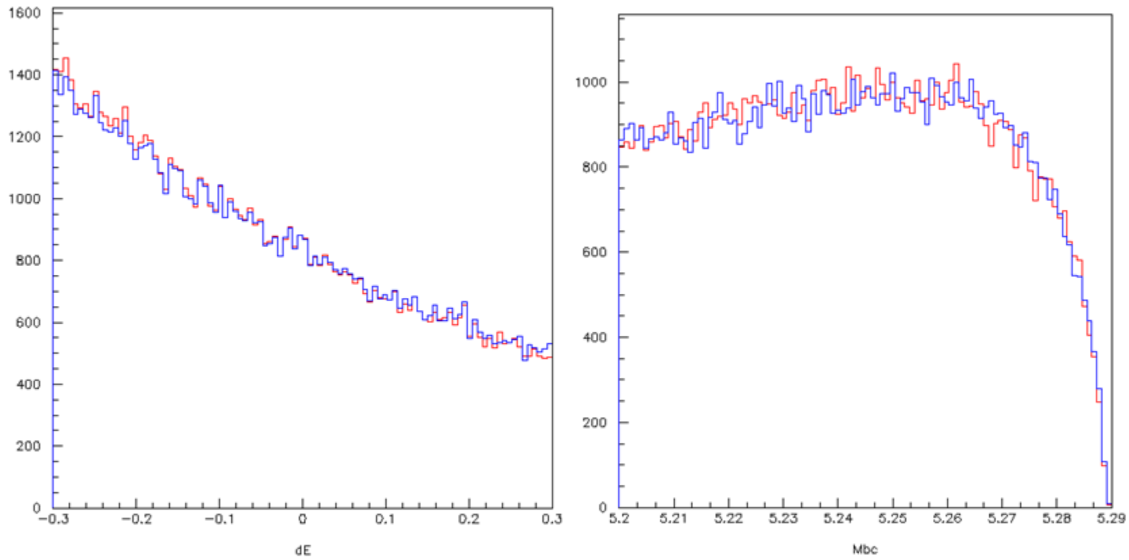

Figure C.6: The ΔE(left) and M_{bc}(right) distributions in $B^{\pm} \to \eta(\gamma\gamma)K^{\pm}$ continuum background, The red one is from modify M_{bc} and blue one is typical M_{bc}. The distributions are same in two definition.

Appendix D

Self Cross Feed Study

The SCF in our study is incuded in signal PDF. And our MC efficiency is also include SCF events. So the branching ratio need not to be calibrate. Here we give the ratio of SCF in our signal. The SCF ratio is studied with function idhep in MC. The idhep function is used to give the particle type for particle in MC. So we can check the event is ture or not with idhep by checking the particle type of the final states particles and their mothers and grandmothers etc... But we find that the SCF ratio is too high if we check all the particles' type in our candidate. And there is also a clear peaks in ΔE, M_{bc}, and η mass distributions in our SCF events. The reason is come from the true gamma is somehow interacting with material before the calorimeter. So, we defined a new definition of true signal.

We do not require the gamma id and gamma's mother's id. But we still require the gamma's grandmother's, or gamma's grand grandmother's, or gamma's grand grand grandmother's id to make sure the gamma is comes from the true B meson in $B \to \eta(\gamma\gamma)h$ mode. (we require the gamma's grand grandmother's, or gamma's grand grand grandmother's, or gamma's grand grand grand grandmother's id is comes form the ture B meson in $B \to \eta(\pi^+\pi^-\pi^0)h$ mode.) And all the charged particle and their mother's id is still required in true signal. Then we find that the ratio of SCF drop, and there is no clear peaks in ΔE, M_{bc}, and η mass distributions in SCF events after that. We give that the SCF ratio is $3 \sim 4.5\%$ in $B \to \eta(\gamma\gamma)h$ mode, and $7 \sim 10\%$ in $B \to \eta(\pi^+\pi^-\pi^0)h$ mode. Here we show the ΔE and M_{bc} distributions in true siganl and SCF. [The explanation of gamma id problem and solution is given by Karim Trabelsi, and is also confirmed by P. Chang.]

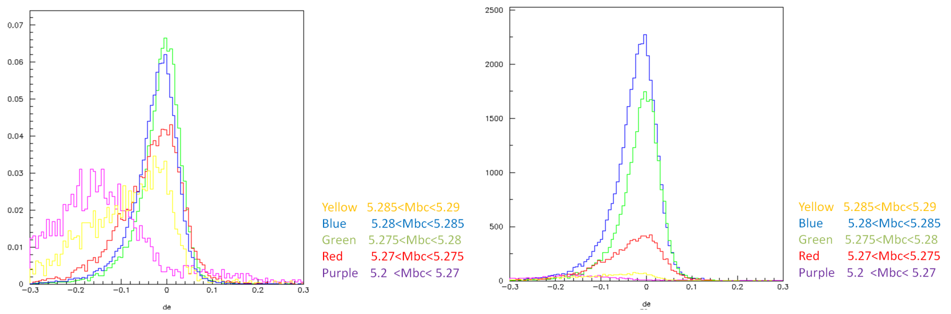

Figure D.1: The ΔE plots in different M_{bc} regions of $B^\pm \to \eta(\gamma\gamma)K^\pm$ mode in true signal with(left) and without(right) normalization.

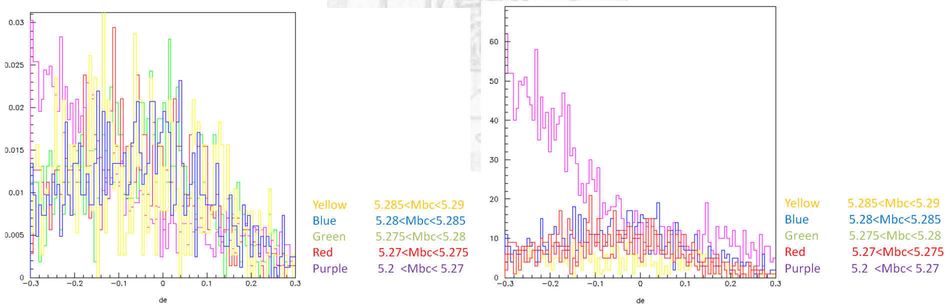

Figure D.2: The ΔE plots in different M_{bc} regions of $B^\pm \to \eta(\gamma\gamma)K^\pm$ mode in SCF with(left) and without(right) normalization.

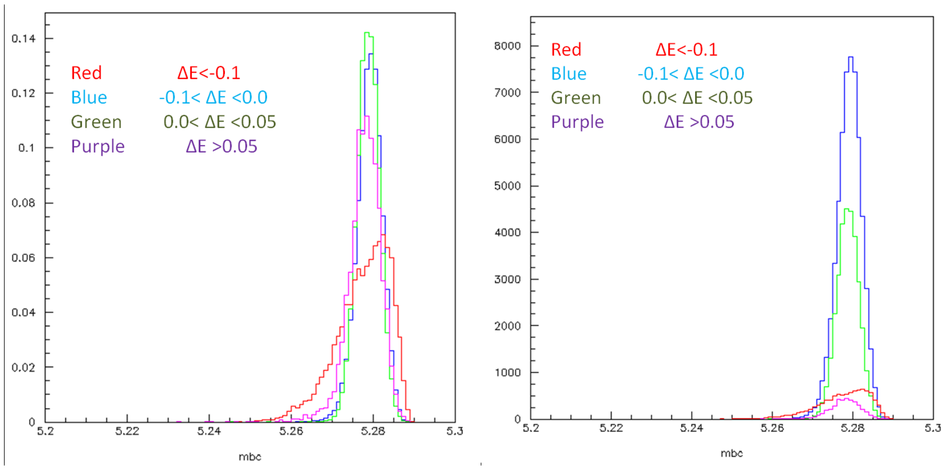

Figure D.3: The M_{bc} plots in different ΔE regions of $B^{\pm} \to \eta(\gamma\gamma)K^{\pm}$ mode in true signal with(left) and without(right) normalization.

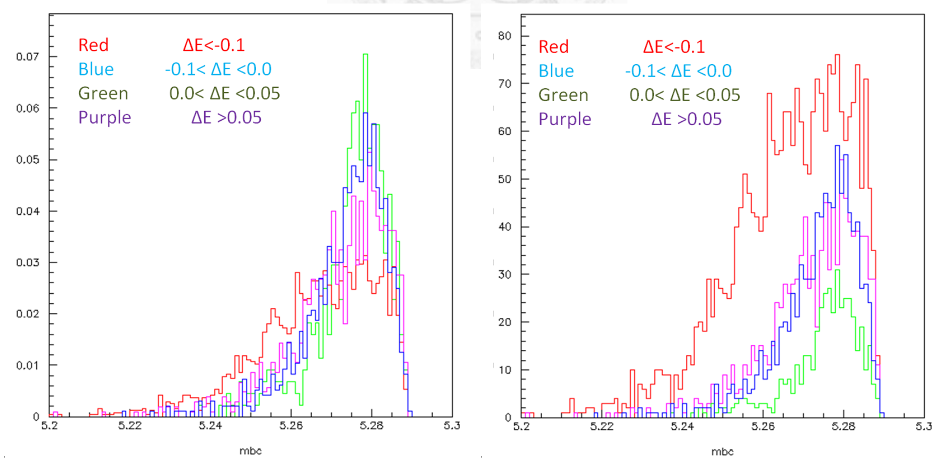

Figure D.4: The M_{bc} plots in different ΔE regions of $B^{\pm} \to \eta(\gamma\gamma)K^{\pm}$ mode in SCF with(left) and without(right) normalization.

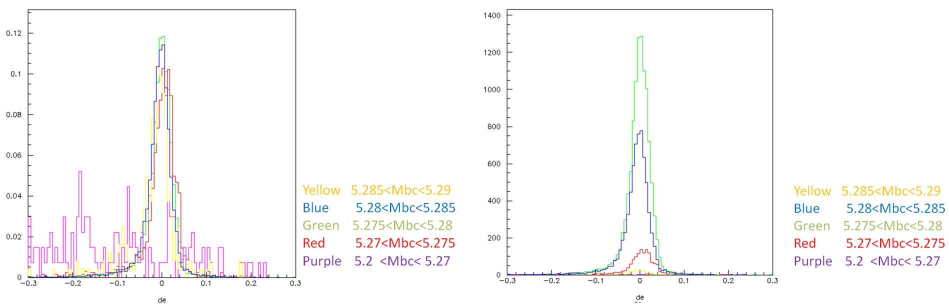

Figure D.5: The ΔE plots in different M_{bc} regions of $B \to \eta(\pi^+\pi^-\pi^0)K^\pm$ mode in true signal with(left) and without(right) normalization.

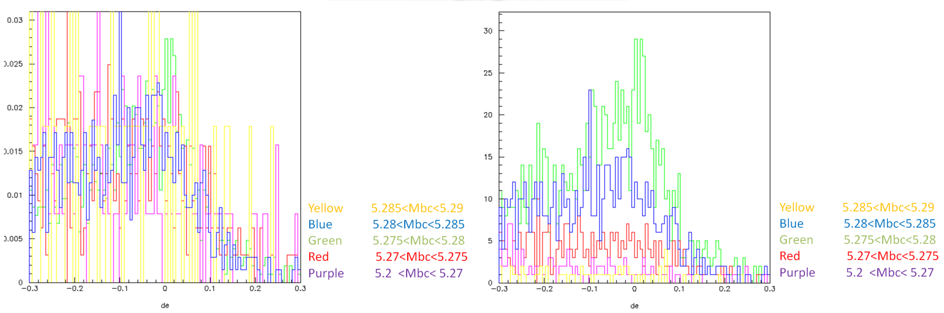

Figure D.6: The ΔE plots in different M_{bc} regions of $B \to \eta(\pi^+\pi^-\pi^0)K^\pm$ mode in SCF with(left) and without(right) normalization.

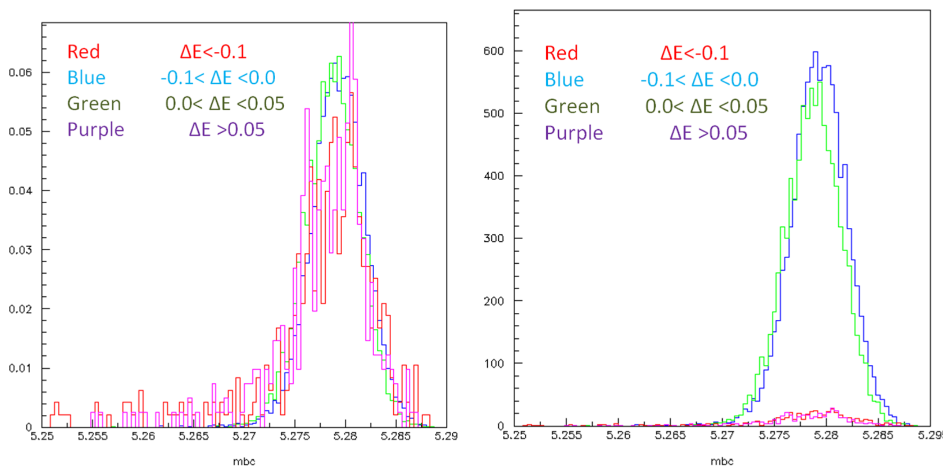

Figure D.7: The M_{bc} plots in different ΔE regions of $B \to \eta(\pi^+\pi^-\pi^0)K^\pm$ mode in true signal with(left) and without(right) normalization.

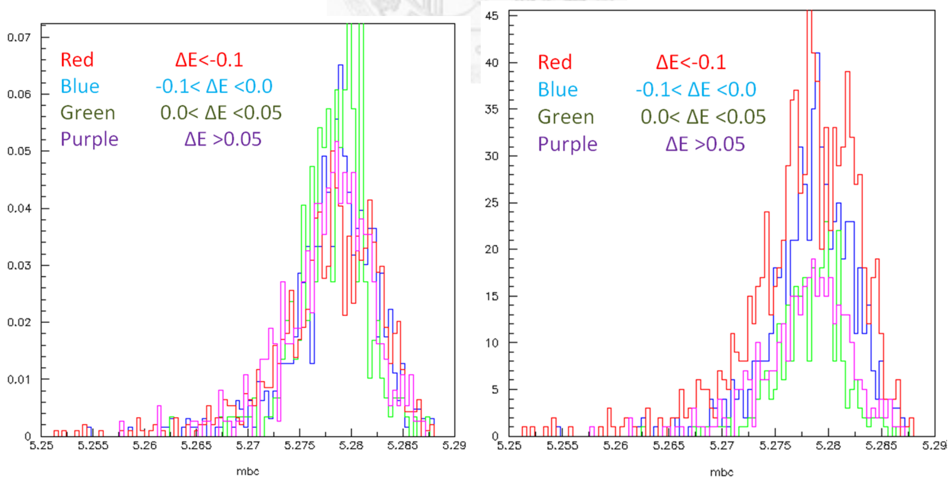

Figure D.8: The M_{bc} plots in different ΔE regions of $B \to \eta(\pi^+\pi^-\pi^0)K^\pm$ mode in SCF with(left) and without(right) normalization.

Appendix E

Fudge Factors Study in High π^0 Momentum Region

In order to make the control sample more like the $B \to \eta(\gamma\gamma)h$ decay. We study $B^+ \to \overline{D}^0(K^+\pi^-\pi^0)\pi^+$ with required π^0 momentum larger than 1 GeV. And compare the fudge factors found with or without π^0 momentum requirement. Although the M_{bc} width, ΔE mean and ΔE width are not close at two sample. And the fudge factors between two sample are still close or within error.

The fudge factors without π^0 momentum requirement is study at 2-D fit. There are about 36% events in our control sample imply π^0 momentum larger than 1 GeV. After apply the π^0 momentum requirement the correlation between M_{bc} and ΔE become a little bit strong. So we study it in one dimensional fit. And the number of generic B background is fixed in M_{bc} 1-D real data fit. (We use the yield of generic B background in 2-D data fit times the MC ratio between with and without π^0 momentum requirement to give this value.)

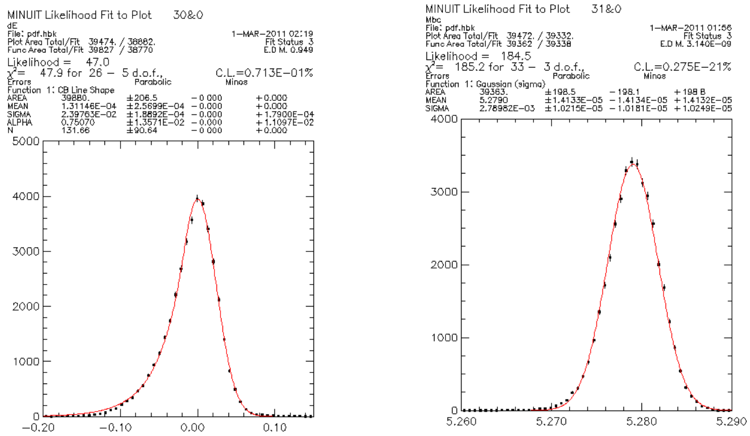

Figure E.1: The ΔE (left) and M_{bc} (right) 1-D fit from signal MC (control sample). $\mathcal{L}R$ cut larger than 0.2 is applied.

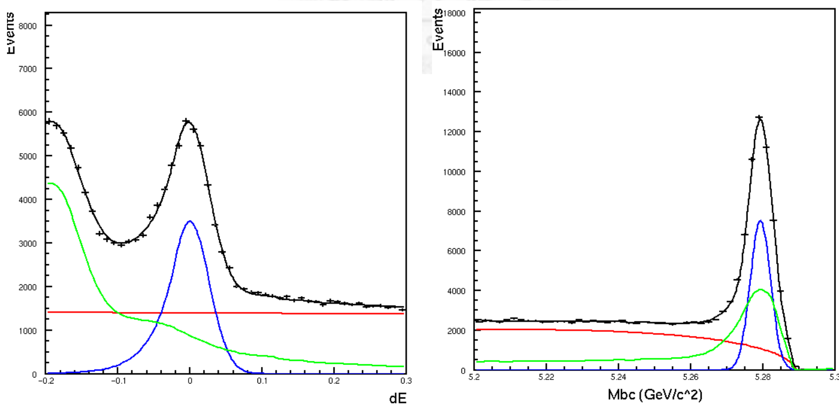

Figure E.2: The ΔE (left) and M_{bc} (right) 1-D fit from real data (control sample). $\mathcal{L}R$ cut larger than 0.2 is applied. The blue line shows the signal PDF, red for continuum background, and green for generic B background.

	DATA(MeV)	MC(MeV)	Pi0 Momentum Requirement	Shift(MeV)
Mbc mean	5279.210±0.015	5279.025±0.007	NO	0.185±0.017
Mbc mean	5279.297±0.031	5279.0 ±0.014	>1.0 GeV	0.270 ±0.034

	DATA(MeV)	MC(MeV)	Pi0 Momentum Requirement	Scale (Data/MC)
Mbc width	2.659±0.013	2.638±0.009	NO	1.008±0.006
Mbc width	2.797 ±0.023	2.790±0.010	>1.0 GeV	1.003±0.009

	DATA(MeV)	MC(MeV)	Pi0 Momentum Requirement	Shift(MeV)
dE mean	-6.447±0.223	-5.525±0.159	NO	-0.922±0.274
dE mean	-0.229±0.307	0.131±0.257	>1.0 GeV	-0.430±0.400

	DATA(MeV)	MC(MeV)	Pi0 Momentum Requirement	Scale (Data/MC)
dE width	24.254±0.119	21.613±0.142	NO	1.122±0.008
dE width	26.814±0.287	23.976±0.189	>1.0 GeV	1.118±0.013

Figure E.3: The fudge fators study in different π^0 momentum regions.

Appendix F

The Significance

The significance of signal without the systematic error effect is defined as

$$Significance = \sqrt{-2ln\frac{L_0}{L_{max}}}.$$

Where L_0 is the likelihood at zero yield or A_{cp} and L_{max} is the maximized likelihood. In order to include the PDF systematic uncertainties into significance, we smear the likelihood (L) distribution with a Gaussian. where Gaussian width is obtained from the product of the branching fraction (A_{cp}) and PDFs systematic error percentage :

$$Width = Br. \times \text{PDFs Systematic Error}(\%).$$

And the area of the Gaussian is fixed to the orgin bins area. And the significances after smearing are very very close to the orgin one for all our mode in both branching fraction and A_{cp} significances (Because the statistical uncertainties are at least 15 times lagers than the PDF systematic error in our study).

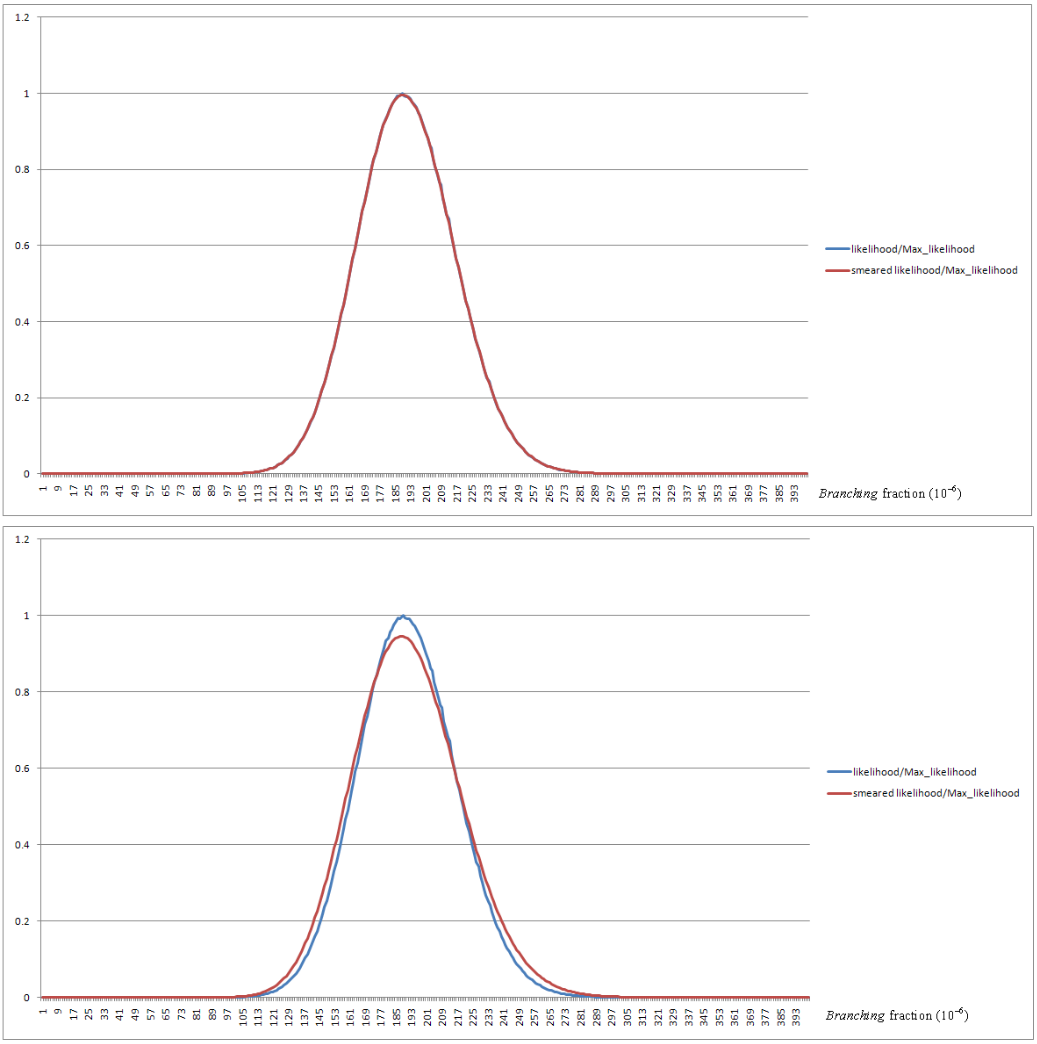

Figure F.1: The $\frac{likelihood}{Max(likelihood)}$ in different branching fraction in $B^{\pm} \rightarrow \eta(\gamma\gamma)K^{\pm}$ mode (top). The blue line is before smearing, and red line is after smearing with PDFs systematic error. And they overlap completely because the PDFs systematic error is very small. So we also show the effect in smearing with total systematic error (bottom). And it is a dome, we do not use the bottom one to calculate significance.

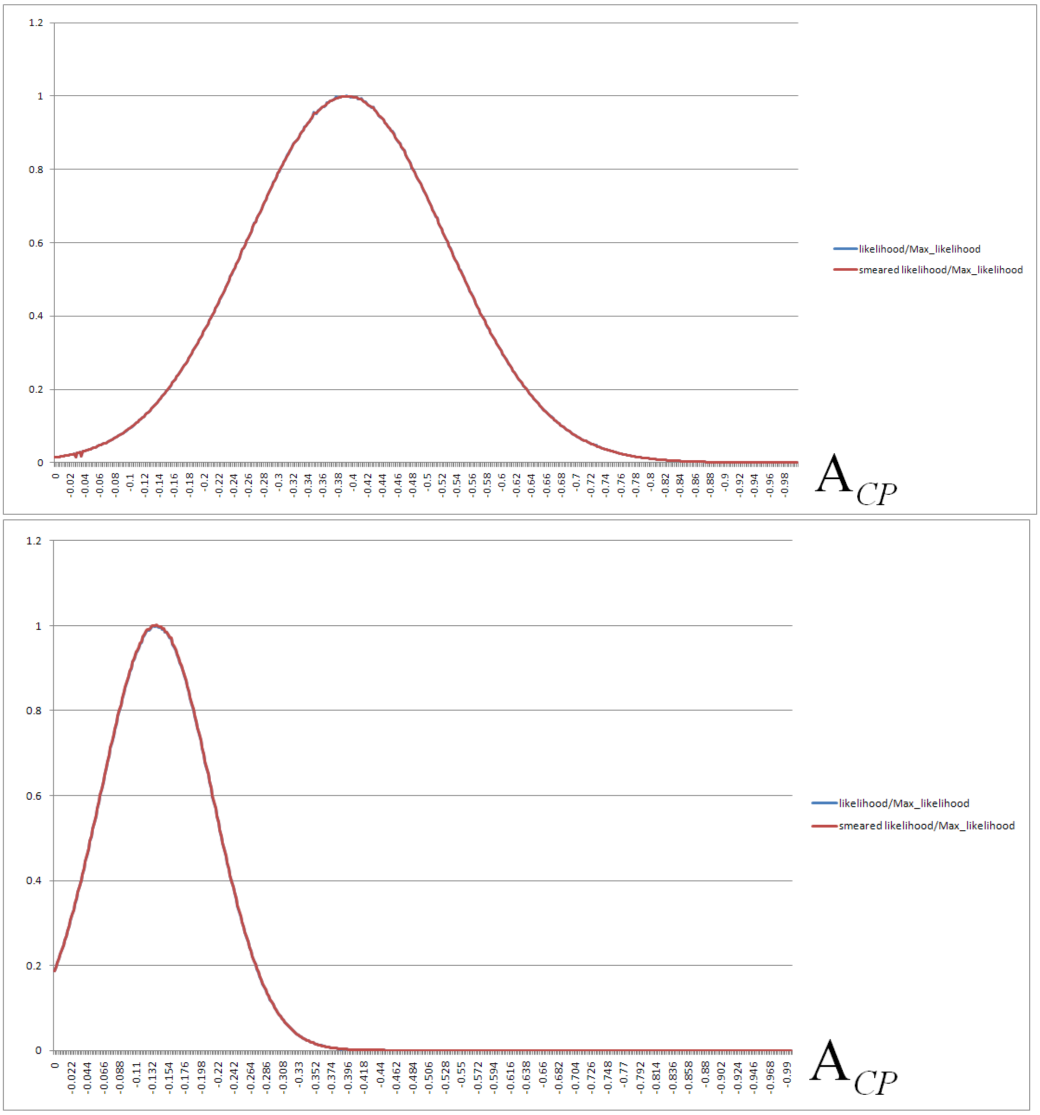

Figure F.2: The $\frac{likelihood}{Max(likelihood)}$ in different A_{CP} in $B^{\pm} \to \eta(\gamma\gamma)K^{\pm}$ mode (top). And in $B^{\pm} \to \eta(\gamma\gamma)\pi^{\pm}$ mode (bottom). The blue line is before smearing, and red line is after smearing with PDFs systematic error. And they overlap completely because the PDFs systematic error is very small.

Appendix G

$\eta \to \gamma\gamma$ and $\eta \to \pi^+\pi^-\pi^0$ result combination

We combine the $\eta \to \gamma\gamma$ and $\eta \to \pi^+\pi^-\pi^0$ result with finding the maximum point of combined likelihood in different branching fraction or A_{CP}. And the combined significances and statistical errors are also giving in the combined likelihood distribution. So all the result will equal to use a combine fitter.

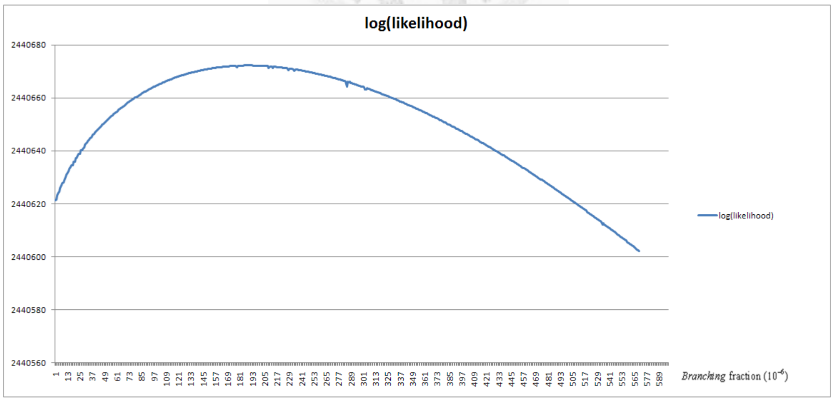

Figure G.1: The *log*(*likelihood*) distribution in different branching fraction in $B^{\pm} \to \eta(\gamma\gamma)K^{\pm}$ mode.

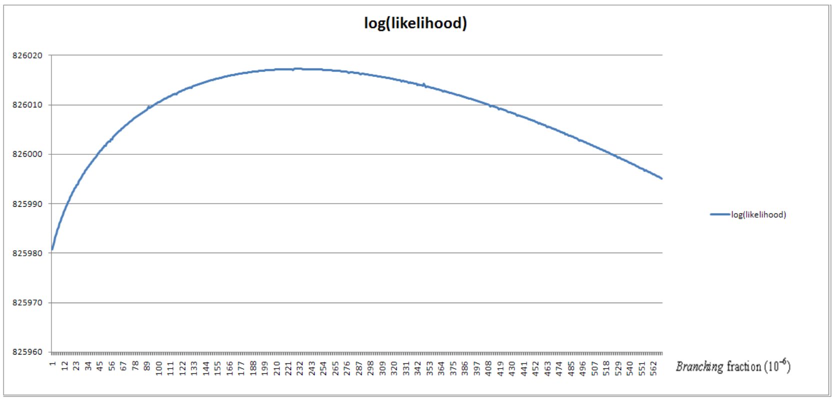

Figure G.2: The $log(likelihood)$ distribution in different branching fraction in $B^{\pm} \to \eta(\pi^+\pi^-\pi^0)K^{\pm}$ mode.

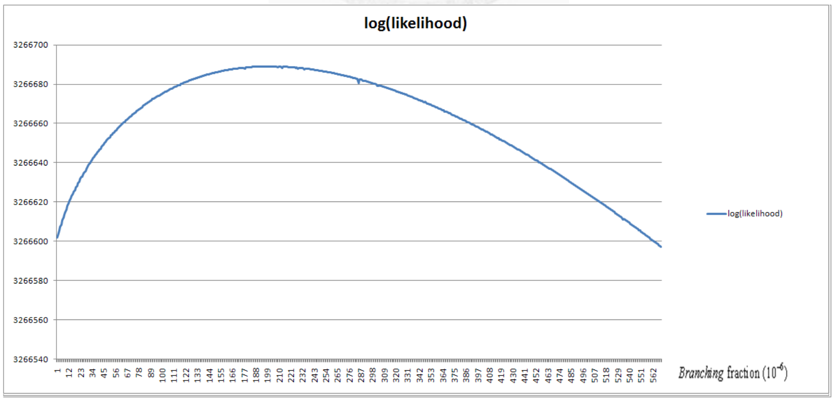

Figure G.3: The combined $log(likelihood)$ in $B^{\pm} \to \eta K^{\pm}$ mode.

Appendix H

Assumptions in Branching Fraction Measurements

In the branching fraction measurements, there are three assumed constant which are $\Gamma(B^+B^-)/\Gamma(B^0\overline{B^0})$ in $\Upsilon(4S)$ decay, efficiency for $B\overline{B}$ events $\epsilon_{B\overline{B}}$ and ratio of the efficiency for $q\overline{q}$ events $r(\epsilon_{q\bar{q}})$.

We assume that in $\Upsilon(4S)$ decay $\Gamma(B^+B^-)/\Gamma(B^0\overline{B^0}) = 1$. And PDG give the $\Gamma(B^+B^-)/\Gamma(B^0\overline{B^0}) = 1.065 \pm 0.026$ in evaluation and 1.031 ± 0.033 in average.

In Belle analysis, the number of $B\overline{B}$ pairs is calculated by :

$$N_{B\overline{B}} = \frac{N^{on} - r(\epsilon_{q\bar{q}})\alpha N^{off}_{q\bar{q}}}{\epsilon_{B\overline{B}}}$$

Where $r(\epsilon_{q\bar{q}})$ is the ratio of the efficiency for $q\overline{q}$ events in off-resonance data to the efficiency for $q\overline{q}$ events in on-resonance data. $\epsilon_{B\overline{B}}$ is the efficiency for $B\overline{B}$ events. Both $r(\epsilon_{qq})$ and $\epsilon_{B\overline{B}}$ are given by MC study. And $\alpha = N^{on}_{q\bar{q}}/N^{off}_{q\bar{q}}$ which is studied in on-resonance and off-resonance through Bhabha and mu-pair events.

Table H.1: Summary table of $\epsilon_{B\overline{B}}$ and $r(\epsilon_{q\bar{q}})$.

Quantity	Exp.7 to 55	Exp.61	Exp.63	Exp.65
$\epsilon_{B\overline{B}}$	0.9913	0.9897	0.9897	0.9893
$r(\epsilon_{q\bar{q}})$	0.9958	1.0001	0.9990	0.9998

Bibliography

[1] B. Aubert, B meson decays to charmless meson pairs containing η or $\eta^{'}$ mesons. , Phys. Rev. D80: 112-002, 2009.

[2] J. Wicht, Search for resonant $B^{\pm} \rightarrow K^{\pm}h$, $B^{\pm} \rightarrow K^{\pm}\gamma\gamma$ Decays at Belle. , Phys. Lett. B662: 323-329, 2008.

[3] P. Chang, Improved measurements of branching fractions and CP asymmetries in $B \rightarrow \eta h$ decays. , Phys. Rev. D75: 071-104, 2007.

[4] S.J. Richichi, Two-body B meson decays to η and $\eta^{'}$: Observation of $B \rightarrow \eta K^{*}$, Phys. Rev. Lett. 85: 520-524, 2000.

[5] F. Fang, Study of $K_S \rightarrow \pi^{+}\pi^{-}$ selection, Belle Note 323 (2000).

[6] K. Nakamura et al. (Particle Data Group), J. Phys. G37: 075-021, 2010.

[7] K. Abe et al., (Belle Collaboration), hep-ex/0308036, 2003.

[8] Eric White, Determination of K_S Efficiency and Systematic Uncertainty, Belle Note 1207 (2011).

[9] Mikihiko Nakao, Measurement of $B \rightarrow K^{*}\gamma$ Asymmetries and Branching Fractions, Belle Note 513 (2004).

[10] B. Bhuyan, High P_T Tracking Efficiency Using Partially Reconstructed D^{*} Decays, Belle Note 1165 (2010).

[11] P. Chang, Update of Branching Fractions and CP Asymmetries for $B \rightarrow \eta h$ Decays with 500 fb^{-1}, Belle Note 939, (20/7/2006).

[12] J. Wicht, Search for resonant $B^{\pm} \to K^{\pm}h$, $B^{\pm} \to K^{\pm}\gamma\gamma$. , Belle Note 936, (27/3/2007).

[13] C.Y. Lin, Relative π^0 efficiency using $D^0 \to K\pi$ and $D^0 \to K\pi\pi^0$, Belle Note 916, (21/6/2006).

[14] H. Kakuno, Neutral B Flavor Tagging for the Measurement of Mixing-induced CP Violation at Belle, hep-ex0403022, (7/2/2008).

[15] M. Herrero,"THE STANDARD MODEL", arXiv:hep-ph/98122242

[16] T.D. Lee, C.N. Yang ,"Question of Parity Conservation in Weak Interaction", Phys. Rev. **104**, 254258 (1956).

[17] C.S. Wu ,"Experimental Test of Parity Conservation in Beta decay", Phys. Rev. **105**, 14131415 (1957).

[18] J.H. Christenson, *et al.*,"Evidence for the 2π decay of the K_S^0 meson", Phys. Rev. Lett. **13**, 128140 (1964).

[19] Makoto Kobayashi and Toshihide Maskawa, "CP-Violation in the Renormalizable Theory of Weak Interaction", Prog. Theor. Phys. Vol. **49** Page 652 (1972).

[20] S. W. Herb, D. C. Hom, L. M. Lederman, J. C. Sens, H. D. Snyder, and J. K. Yoh, "Observation of a Dimuon Resonance at 9.5 GeV in 400-GeV Proton-Nucleus Collisions", Phys. Rev. Lett. **39**, 252255 (1977).

[21] M. Hazumi, Phys. Lett. B **583**, 285 (2004).

[22] S. Kurokawa, E. Kikutani, "Overview of the KEKB accelerators", Nuclear Instruments and Methods in Physics Research A **499** (2003) 1 - 7.

[23] M. T. Cheng *et al.* Letter of intent for a study of CP violation in B meson decays; KEK Report, 94-2 1994

[24] http://nobelprize.org/nobel_prizes/physics/laureates/2008/

[25] A. Abashian *et al.* (Belle Collaboration), Nucl. Instr. and Meth. A **479**, 117 (2002).

[26] BELLE HOME PAGE
http://belle.kek.jp

[27] A. Abashian *et al.* Nucl. Instr. and Meth. A **491**, 69-82 (2002).

[28] The EvtGen home page
http://www.slac.standford.edu/lange/EvtGen/

[29] GEANT - Detector Description and Simulation Tool
http://wwwasd.web.cern.ch/wwwasd/geant/index.html

[30] Particle data group
http://pdg.lbl.gov

[31] F.Fang, Study of $K_S \to \pi^+\pi^-$ Selection, Belle Note 323 (2000).

[32] Geoffray C. Fox and Stephen Wolfram, Phys. Rev. Lett. **41**, 1581 - 1585 (1978).

[33] B. Aubert *et al.* (BABAR Collaboration), Phys. Rev. D81:051101, 2010.

[34] G. Punzi (2003), physics/0308063.

[35] H. Albrecht *et al.* (ARGUS Collaboration), Phys. Lett. B **229**, 304 (1989).

Evidence for direct CP Violation in $B^+ \to \eta h^+$ and Observation of $B^0 \to \eta K^0$

Using a data set of 772×10^6 $B\overline{B}$ pairs collected with the Belle detector at the KEKB asymmetric-energy e^+e^- collider, we observe the decay $B^0 \to \eta K^0$ with a significance of 5.4 standard deviations (σ), and we measure $\mathcal{B}(B^0 \to \eta K^0) = (1.27^{+0.33}_{-0.29} \pm 0.08) \times 10^{-6}$. In addition, we determine the decay branching fractions $\mathcal{B}(B^\pm \to \eta K^\pm) = (2.12^{+0.23}_{-0.22} \pm 0.11) \times 10^{-6}$ and $\mathcal{B}(B^\pm \to \eta\pi^\pm) = (4.07 \pm 0.26 \pm 0.21) \times 10^{-6}$. We measure the charge asymmetries $A_{CP}(B^\pm \to \eta K^\pm) = -0.38 \pm 0.11 \pm 0.01$ and $A_{CP}(B^\pm \to \eta\pi^\pm) = -0.19 \pm 0.06 \pm 0.01$ with a significance of 3.8σ and 3.0σ, respectively. The first and second uncertainties reported on all measurements are statistical and systematic, respectively.

PACS numbers: 13.25.Hw, 12.15.Hh, 11.30.Er

Charmless hadronic B decays play an important roles in understanding the dynamics of B decays. The decays $B \to \eta K$ ($B \to \eta\pi$) are expected to proceed primarily through $b \to s$ ($b \to d$) penguin processes and a $b \to u$ tree transition. The penguin amplitudes may interfere with the tree amplitude, resulting in a large direct CP asymmetry (A_{CP}) [1, 2]. Theoretical expectations for contributions from other mechanisms [3–8] also suggest a large A_{CP} although the sign could be positive or negative. Previous Belle [9] and Babar [11] measurements have indicated a large negative A_{CP} in the case of $B \to \eta K^\pm$.

In this Letter, we report the first observation of the $B^0 \to \eta K^0$ decay. This decay is expected to be dominated by the $\bar{b} \to \bar{s}s\bar{s}$ and $\bar{b} \to \bar{s}d\bar{d}$ penguins processes shown in Fig. 1. For $B^\pm \to \eta h^\pm$ ($h = K$ or π), we also present evidence for the non-zero direct CP asymmetry

$$A_{CP} \equiv \frac{N(B^- \to \eta h^-) - N(B^+ \to \eta h^+)}{N(B^- \to \eta h^-) + N(B^+ \to \eta h^+)}, \qquad (1)$$

where $N(B^\pm \to \eta h^\pm)$ denotes the yield obtained for the $B^\pm \to \eta h^\pm$ decay.

This analysis is performed on a sample of $(772 \pm 11) \times 10^6$ $B\overline{B}$ pairs collected with the Belle detector at the KEKB e^+e^- asymmetric-energy (3.5 GeV on 8 GeV) collider [12] operating at the $\Upsilon(4S)$ resonance. The production rates of B^+B^- and $B^0\overline{B}^0$ pairs are assumed to be equal in $\Upsilon(4S)$ decay.

The Belle detector [13] is a large-solid-angle magnetic spectrometer that consists of a silicon vertex detector

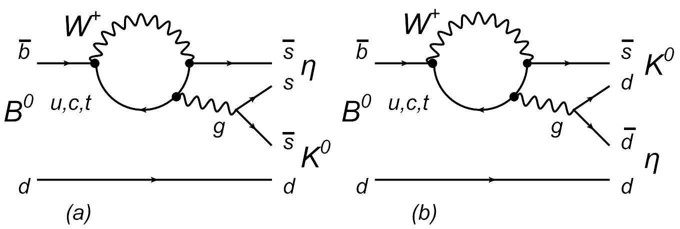

FIG. 1: (a) The $\bar{b} \to \bar{s}s\bar{s}$ and (b) $\bar{b} \to \bar{s}d\bar{d}$ penguin diagrams for $B^0 \to \eta K^0$ decay.

(SVD), a 50-layer central drift chamber (CDC), an array of aerogel threshold Cherenkov counters (ACC), a barrel-like arrangement of time-of-flight scintillation counters (TOF), and an electromagnetic calorimeter comprised of CsI(Tl) crystals located inside a superconducting solenoid coil that provides a 1.5 T magnetic field. An iron flux-return located outside the coil is instrumented to detect K_L^0 mesons and to identify muons.

The event selection and B candidate reconstruction are similar to those documented in our previous publication [9]. Two η decay channels are considered in the analysis: $\eta \to \gamma\gamma$ ($\eta_{\gamma\gamma}$) and $\eta \to \pi^+\pi^-\pi^0$ ($\eta_{3\pi}$). We require the two photons from the η and π^0 candidates to have laboratory energies ($E_{\gamma i},\ i = 1, 2$) above 50 MeV. In the $\eta_{\gamma\gamma}$ reconstruction, the photon energy asymmetry in the laboratory frame, $\frac{|E_{\gamma 1} - E_{\gamma 2}|}{E_{\gamma 1} + E_{\gamma 2}}$, is restricted to be less than 0.9 to reduce the large combinatorial background from soft photons. Neither photon from $\eta_{\gamma\gamma}$ is allowed to pair with any other photon having an energy greater than 100 MeV to form a π^0 candidate. Candidate π^0 mesons are selected by requiring the two-photon invariant mass to be in a window between 115 MeV/c^2 and 152 MeV/c^2. The momentum vector of each photon is then adjusted to constrain the mass of the photon pair to the nominal π^0 mass.

Candidate $\eta_{3\pi}$ mesons are reconstructed by combining π^0 candidates with a pair of oppositely charged tracks that originate from the interaction point (IP). We require the invariant mass of the $\eta_{\gamma\gamma}$ and $\eta_{3\pi}$ candidates to be in the intervals $(501, 573)$ MeV/c^2 and $(538.5, 556.5)$ MeV/c^2 respectively. After the selection of each candidate, the η mass constraint is implemented by adjusting momentum vectors of the daughter particles.

Charged tracks that are not used to form K_S^0 candidates are required to have a distance of closest approach with respect to the IP of less than 3.0 cm along the beam direction (z) and less than 0.3 cm in the transverse plane. Charged kaons and pions are identified using dE/dx information from the CDC, Cherenkov light yields in the ACC and time of flight in the TOF, which are combined to form a likelihood ratio, $\mathcal{R}_{K/\pi} = \mathcal{L}_K/(\mathcal{L}_K + \mathcal{L}_\pi)$, where

$\mathcal{L}_K$ ($\mathcal{L}_\pi$) is the likelihood that the track is a kaon (pion). Charged tracks with $\mathcal{R}_{K/\pi} > 0.6$ (< 0.4) are regarded as kaons (pions) for $B^\pm \to \eta K^\pm$ ($B^\pm \to \eta\pi^\pm$) decays. A looser requirement, $\mathcal{R}_{K/\pi} < 0.6$ for pions, is used for the $\eta \to \pi^+\pi^-\pi^0$ selection. Furthermore, we reject charged tracks consistent with an electron or a muon hypothesis in $B^\pm \to \eta h^\pm$ and $B^0 \to \eta K^0$ decays.

The K^0_S candidates are reconstructed from pairs of oppositely charged tracks with an invariant mass lying between 488 MeV/c^2 and 508 MeV/c^2. Each candidate must have a displaced vertex with a flight direction consistent with that of a K^0_S meson originating from the IP.

Candidate B mesons are identified using the modified beam-energy constrained mass [15], $M_{\rm bc} = \sqrt{(E^*_{\rm beam}/c^2)^2 - |\vec{p}^*_B/c|^2}$, and the energy difference, $\Delta E = E^*_B - E^*_{\rm beam}$, where $E^*_{\rm beam}$ is the beam energy, and E^*_B and $\vec{p}^*_B$ are the energy and modified momentum, respectively, of the B candidate in the $\Upsilon(4S)$ rest frame. The energy E^*_B is calculated as $E^*_B = E^*_\eta + E^*_{h'}$, where h' denotes K^0_S, $K^\pm$, or $\pi^\pm$. The momentum $\vec{p}^*_B$ is calculated according to

$$\vec{p}^*_B = \vec{p}^*_{h'} + \frac{\vec{p}^*_\eta}{|\vec{p}^*_\eta|} \times \sqrt{(E^*_{\rm beam} - E^*_{h'})^2 - M^2_\eta}, \qquad (2)$$

where M_η is the nominal η mass [16]. Since charged tracks are determined with better precision than photon, the η decays to neutral particles that have worse momentum resolution than charged tracks. The $\vec{p}^*_B$ resolution is improved because the h' momentum and $E^*_{\rm beam}$ are determined more precisely than $\vec{p}^*_\eta$. Events with $M_{\rm bc} > 5.2$ GeV/c^2 and $|\Delta E| < 0.3$ GeV are retained for the further analysis.

The dominant background arises from $e^+e^- \to q\bar{q}$ ($q = u, d, s, c$) continuum events. We use topological event variables to distinguish spherically distributed $B\overline{B}$ events from the jet-like continuum background. First we combine a set of modified Fox-Wolfram moments [17] into a Fisher discriminant. Then we compute a likelihood that is the product of probabilities based on the Fisher discriminant, $\cos\theta_B$ and Δz. Here θ_B is the angle between the B flight direction and the beam direction in the $\Upsilon(4S)$ rest frame, and Δz is the decay flight length difference along beam direction between the signal B and its accompanying B. A likelihood ratio, $\mathcal{R} = \mathcal{L}_s/(\mathcal{L}_s + \mathcal{L}_{q\bar{q}})$, is formed out of signal ($\mathcal{L}_s$) and background ($\mathcal{L}_{q\bar{q}}$) likelihoods, where are obtained from a GEANT-based [18] Monte Carlo (MC) simulation samples. Signal MC events are generated with EVTGEN [19], which includes the PHOTOS [20] simulation package to take into account final state radiation. We require $\mathcal{R} > 0.2$ to suppress continuum background in all modes. We translate the $\mathcal{R}$ to $\mathcal{R}'$ after applying the $\mathcal{R}$ requirement, which is defined as:

$$\mathcal{R}' = \ln\left(\frac{\mathcal{R} - \mathcal{R}_{\rm min}}{\mathcal{R}_{\rm max} - \mathcal{R}}\right) \qquad (3)$$

Where $\mathcal{R}_{\rm min}$ ($\mathcal{R}_{\rm max}$) is equal to 0.2 (1.0). This translation ensures that both signal and background $\mathcal{R}'$ distributions are described by an analytic function.

Signal yields are extracted by performing an extended unbinned three-dimensional maximum likelihood fits. The likelihood for each B^+ mode is defined as

$$\mathcal{L} = e^{-\sum_j N_j} \times \prod_i (\sum_j N_j \mathcal{P}^i_j) \quad \text{and}$$

$$\mathcal{P}^i_j = \frac{1}{2}[1 - q^i \cdot A_{CPj}] P_j(M^i_{\rm bc}, \Delta E^i, \mathcal{R}'^i), \qquad (4)$$

where i denotes the i-th event and N_j is the number of events for the category j, which corresponds to either signal, continuum, the feed-across due to K-π misidentification, or the background from other charmless B decays. $P_j(M_{\rm bc}, \Delta E, \mathcal{R}'^i)$ is the probability density function (PDF) in $M_{\rm bc}$, ΔE and $\mathcal{R}'$. Here q is the B-meson charge. For the B^0 mode, $\mathcal{P}^i_j$ in Eq. 4 is simply $P_j(M^i_{\rm bc}, \Delta E^i, \mathcal{R}'^i)$. The validity of the three-dimensional fit is established with large ensemble tests with MC and with fits to a control sample of $B^+ \to \overline{D^0}(K^+\pi^-\pi^0)\pi^+$ decays.

All the signal and feed-across background PDFs in $M_{\rm bc}$ and $\mathcal{R}'$ are described by a single Gaussian. In $B \to \eta_{\gamma\gamma} h$ ($B \to \eta_{3\pi} h$) modes PDFs in ΔE are described by a Crystal Ball [21] (a sum of two Gaussians) function . The peak positions and resolutions in $M_{\rm bc}$, ΔE and $\mathcal{R}'$ are adjusted according to the differences observed between data and MC in the $B^+ \to \overline{D^0}\pi^+$ or $B^+ \to \pi^0 K^+$ control samples.

The continuum background in ΔE is described by a second-order polynomial, while the $M_{\rm bc}$ distribution is parameterized by an ARGUS function, $f(x) = x\sqrt{1-x^2}\exp[-\xi(1-x^2)]$, where x is $M_{\rm bc}/E_{\rm beam}$ and ξ is a free parameter in the fit [22]; the $\mathcal{R}'$ PDF is a double Gaussian function. The background PDFs in $M_{\rm bc}$ and ΔE for charmless B decays are both modeled by smoothed two-dimensional histograms obtained from a large MC sample; the $\mathcal{R}'$ PDF is a single Gaussian.

We perform a simultaneous fit to $B^\pm \to \eta K^\pm$ and $B^\pm \to \eta\pi^\pm$ candidates, since these two decay modes feed into each other. In the likelihood fits all N_j and A_{CPj} are allowed to vary except for the feed-across backgrounds. The values of A_{CP} and branching fraction for feed-across background in $\eta K^\pm$ ($\eta\pi^\pm$) is fixed to that of the signal in $\eta\pi^\pm$ ($\eta K^\pm$). Figure 2 shows the $M_{\rm bc}$, ΔE and $\mathcal{R}'$ projections of the fit in $B^0 \to \eta K^0_S$. Corresponding projections for the B^+ and B^- samples are shown separately in Fig. 3.

The branching fraction for each mode is calculated by dividing the efficiency-corrected signal yield by the number of $B\overline{B}$ pairs. The dominant systematic errors on the branching fraction come from MC modeling of the η, π^0, and K^0_S selection efficiency, which are 4.0%, 4.0% and 1.6%, respectively. The systematic error due to $\mathcal{R}(K/\pi)$ selection is estimated from the

TABLE I: Detection efficiency (ϵ_{eff}) including sub-decay branching fractions, yields, significance of branching fraction $\Sigma(\mathcal{B})$, measured branching fraction $\mathcal{B}$, significance of charge asymmetry $\Sigma(A_{CP})$ and charge asymmetry A_{CP} for the $B \to \eta h$ decays. Thre first errors are statistical and the second ones are systematic.

Mode	ϵ_{eff} (%)	Yield	$\Sigma(\mathcal{B})$	$\mathcal{B}$ (10^{-6})	$\Sigma(A_{CP})$	A_{CP}
$B^{\pm} \to \eta K^{\pm}$			13.2	$2.12^{+0.23}_{-0.22} \pm 0.11$	3.8	$-0.38 \pm 0.11 \pm 0.01$
$\eta_{\gamma\gamma} K^{\pm}$	13.25	$201.88^{+27.08}_{-26.48}$	10.2	$2.07 \pm 0.27 \pm 0.10$	2.9	$-0.36 \pm 0.13 \pm 0.01$
$\eta_{3\pi} K^{\pm}$	4.94	$80.17^{+14.92}_{-13.85}$	8.6	$2.29^{+0.43}_{-0.40} \pm 0.15$	2.4	$-0.42 \pm 0.18 \pm 0.01$
$B^{\pm} \to \eta \pi^{\pm}$			22.4	$4.07 \pm 0.26 \pm 0.21$	3.0	$-0.19 \pm 0.06 \pm 0.01$
$\eta_{\gamma\gamma} \pi^{\pm}$	15.34	$480.61^{+35.06}_{-35.97}$	19.0	$4.24^{+0.31}_{-0.32} \pm 0.19$	1.8	$-0.14 \pm 0.08 \pm 0.01$
$\eta_{3\pi} \pi^{\pm}$	5.44	$138.55^{+18.50}_{-17.47}$	12.2	$3.63 \pm 0.49 \pm 0.25$	2.5	$-0.31^{+0.13}_{-0.12} \pm 0.01$
$B^{0} \to \eta K^{0}$			5.4	$1.27^{+0.33}_{-0.29} \pm 0.08$		
$\eta_{\gamma\gamma} K^{0}$	4.15	$38.03^{+12.62}_{-11.45}$	4.0	$1.18^{+0.39}_{-0.35} \pm 0.06$		
$\eta_{3\pi} K^{0}$	1.48	$16.23^{+6.45}_{-5.43}$	4.1	$1.48^{+0.59}_{-0.49} \pm 0.10$		

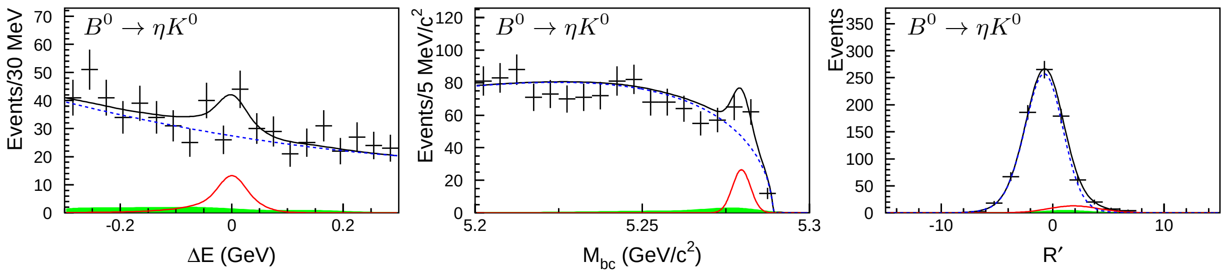

FIG. 2: ΔE (left), $M_{\rm bc}$ (middle) and $\mathcal{R}'$ (right) distributions for $B^0 \to \eta K^0$ candidates with the $\eta_{\gamma\gamma}$ and $\eta_{3\pi}$ modes combined. Points with errors represent the data, the full fit functions are shown by black solid curves, signals are shown by red solid curves, dashed lines show the continuum contributions and filled histograms are the contributions from charmless B decays. The ΔE, $M_{\rm bc}$ and $\mathcal{R}'$ projections of the fit are for events that have 5.27 GeV/c^2 $< M_{\rm bc} <$ 5.3 GeV/c^2 and $\mathcal{R}'$ >0.55, -0.1 GeV< $|\Delta E| <$ 0.08 GeV and $\mathcal{R}'$ >0.55, -0.1 GeV< $|\Delta E| <$ 0.08 GeV and 5.27 GeV/c^2 $< M_{\rm bc} <$ 5.3 GeV/c^2, respectively.

$D^{*+} \to D^0(K^-\pi^+)\pi^+$ sample. Systematic error due to the charged-track reconstruction efficiency is estimated to be 0.35% per track which is determined from the $D^{*\pm} \to D^0\pi^{\pm}(D^0 \to \pi^+\pi^-K^0_S)$ decay. Data-MC efficiency difference due to the likelihood ratio $\mathcal{R}$ cut is investigated with the $B^+ \to \overline{D}{}^0\pi^+$. The fitting systematic errors come from the signal PDF modeling, which we estimate from changes to the fit parameters after varying the calibration factors by one standard deviation. The systematic errors in charmless B decays PDF modeling is estimated by the difference between floated and fixed the yields to the expected values in charmless B decays. The systematic error due to the uncertainty in the total number of $B\overline{B}$ pairs is 1.4% and the error due to limited signal MC statistics used to evaluate the efficiency is 0.55%. The systematic errors in A_{CP} include detector bias, the uncertainties on detector bias and PDF modeling. The possible detector bias due to the tracking acceptance and $\mathcal{R}(K/\pi)$ selection for $A_{CP}(B^{\pm} \to \eta\pi^{\pm})$ is evaluated using the fitting A_{CP} value of the continuum background [23]. The detector bias of $A_{CP}(B^{\pm} \to \eta K^{\pm})$ is evaluated using the $D_s^+ \to \phi\pi^+[\phi \to K^+K^-]$ and $D^0 \to K^-\pi^+$ samples [23]. There is a contribution to the A_{CP} systematic uncertainty from the modeling of the signal PDFs. The total systematic errors of A_{CP} are in the range $(8.2 - 14.2) \times 10^{-3}$.

A statistical significance is calculated as $\mathcal{S} = \sqrt{-2\ln(\mathcal{L}_0/\mathcal{L}_{\rm max})}$, where $\mathcal{L}_0$ is the likelihood value for the zero signal yield or A_{CP}, and $\mathcal{L}_{max}$ is the nominal likelihood value. The total significance including PDF modeling systematic uncertainty is calculated after smearing the likelihood distribution with the respective PDF modeling systematic error. In Table I, a sum of fitted signal yields, charged asymmteries and the average efficiency are listed. The combined result of two η decay modes is obtained from a simultaneous fit.

In summary, using a data sample containing 772 $\times 10^6$ $B\overline{B}$ pairs and a robust three-dimensional fit, we provide a new measurements based on signal yields 150% more than those reported in our previous publications [9, 10]. We improve on the following measurements of the branching fractions and charge asymmetries, $\mathcal{B}(B^{\pm} \to \eta K^{\pm}) = (2.12^{+0.23}_{-0.22} \pm 0.11) \times 10^{-6}$, $\mathcal{B}(B^{\pm} \to \eta\pi^{\pm}) = 4.07 \pm 0.26 \pm 0.21) \times 10^{-6}$. $A_{CP}(B^{\pm} \to \eta K^{\pm}) = -0.38 \pm 0.11 \pm 0.01$ and $A_{CP}(B^{\pm} \to \eta\pi^{\pm}) = -0.19 \pm 0.06 \pm 0.01$. The significance of $A_{CP}(\eta K^+)$ $[A_{CP}(\eta\pi^+)]$ is 3.8σ [3.0σ]. In addition, we observe $B^0 \to \eta K^0$ with a branching fraction $\mathcal{B}(B^0 \to \eta K^0) = (1.27^{+0.33}_{-0.29} \pm 0.08) \times 10^{-6}$. Our

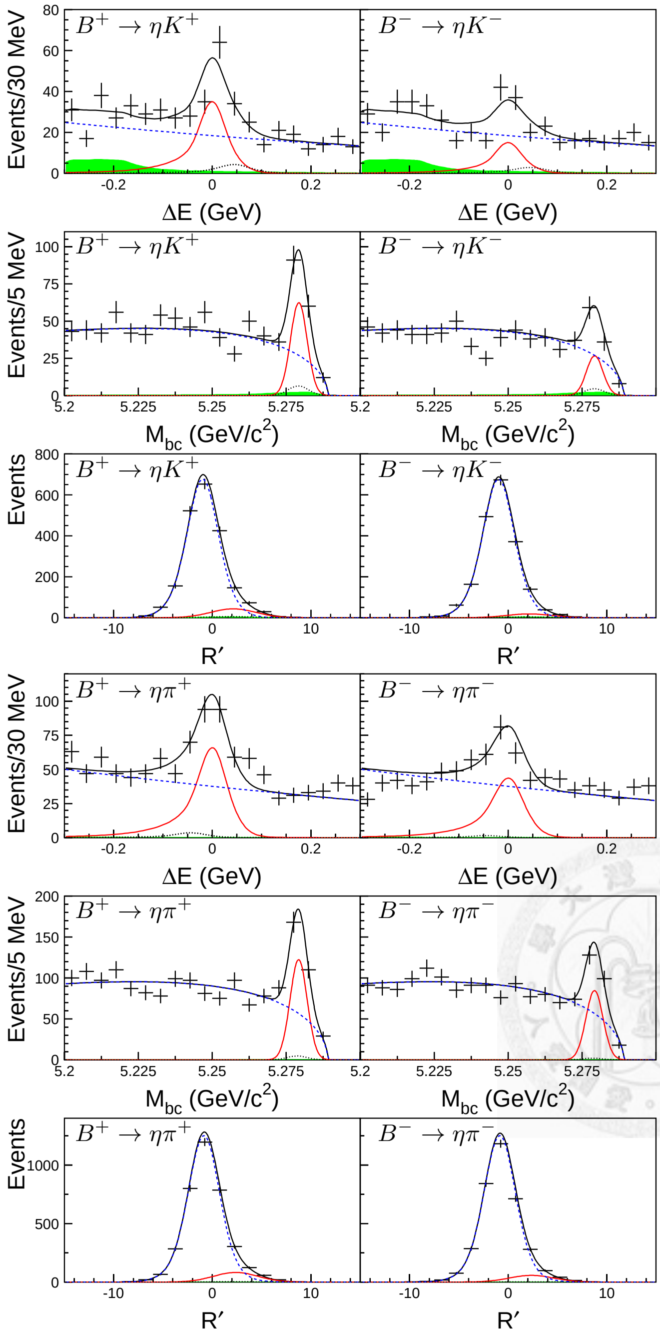

FIG. 3: ΔE, $M_{\rm bc}$ and $\mathcal{R}'$ projections for $B^+ \to \eta h^+$ (left) and $B^- \to \eta h^-$ (right) candidates with the $\eta_{\gamma\gamma}$ and $\eta_{3\pi}$ modes combined. Points with errors represent the data, the full fit functions are shown by black solid curves, signals are shown by red solid curves, dashed lines show the continuum contributions, dotted lines for feed-across background from misidentification and filled histograms are the contributions from charmless B decays. The ΔE, $M_{\rm bc}$ and $\mathcal{R}'$ projections of the fits are for events that have 5.27 GeV/c^2 $< M_{\rm bc} <$ 5.3 GeV/c^2 and $\mathcal{R}'$ >1.95, -0.1 GeV< $|\Delta E|$ < 0.08 GeV and $\mathcal{R}'$ >1.95, -0.1 GeV< $|\Delta E|$ < 0.08 GeV and 5.27 GeV/c^2 $< M_{\rm bc} <$ 5.3 GeV/c^2, respectively.

measurements are consistent with previous results [9, 10], and have better precision than previously reported values [9, 11].

We thank the KEKB group for excellent operation of the accelerator, the KEK cryogenics group for efficient solenoid operations, and the KEK computer group and the NII for valuable computing and Super-SINET network support. We acknowledge support from MEXT and JSPS (Japan); ARC and DEST (Australia); NSFC and KIP of CAS (China); DST (India); MOEHRD, KOSEF and KRF (Korea); KBN (Poland); MIST (Russia); ARRS (Slovenia); SNSF (Switzerland); NSC and MOE (Taiwan); and DOE (USA).

[1] H. J. Lipkin, Phys. Lett. B **254**, 247 (1991).
[2] M. Bander, D. Silverman and A. Soni, Phys. Rev. Lett. **43**, 242 (1979).
[3] H.-Y. Cheng and C,-K. Chua, Phys. Rev. D **80**, 114008 (2009).
[4] Z. J. Xiao, Z. Q. Zhang, X. Liu and L. B. Guo, Phys. Rev. D **78**, 114001 (2008).
[5] H. S. Wang, X. Liu, Z. J. Xiao, L. B. Guo and C. D. Lu, Nucl. Phys. B **738**, 243 (2006).
[6] A.G. Akeroyd, C.H. Chen, and C.Q. Geng, Phys. Rev. D **75**, 054003 (2007).
[7] A. R. Williamson and J. Zupan, Phys. Rev. D **74**, 014003 (2006) [Erratum-ibid. D **74**, 03901 (2006)].
[8] M. Beneke and M. Neubert, Nucl. Phys. B **651**, 225 (2003).
[9] P. Chang *et al.* (Belle Collaboration), Phys. Rev. D **75**, 071104 (2007).
[10] J. Wicht *et al.* (Belle Collaboration), Phys. Lett. B **662**, 323 (2008).
[11] B. Aubert *et al.* (BaBar Collaboration), Phys. Rev. D **80**, 112002 (2009).
[12] S. Kurokawa and E. Kikutani, Nucl. Instr. Meth. A **499**, 1 (2003), and other papers included in this volume.
[13] A. Abashian *et al.* (Belle Collaboration), Nucl. Instr. Meth. A **479**, 117 (2002).
[14] Z. Natkaniec *et al.* (Belle SVD2 Group), Nucl. Instr. Meth. A **560**, 1 (2006).
[15] M. Nakao *et al.* (Belle Collaboration), Phys. Rev. D **69**, 112001 (2004). We follow their $M_{\rm bc}$ definition and modify it for η to improve the resolution for signal $M_{\rm bc}$ and reduce the correlation between ΔE and $M_{\rm bc}$.
[16] http://pdg.lbl.gov/
[17] G. C. Fox and S. Wolfram, Phys. Rev. Lett. **41** 1581 (1978). The modified moments used in this paper are described in, S. H. Lee *et al.* (Belle Collaboration), Phys. Rev. Lett. **91**, 261801 (2003).
[18] R. Brun *et al.*, GEANT 3.21, CERN Report No. DD/EE/84-1 (1987).
[19] D. J. Lange, Nucl. Instrum. Meth. A 462, 152 (2001).
[20] E. Barberio and Z. Was, Comput. Phys. Commun. **79**, 291 (1994); P. Golonka and Z. Was, hep-ph/0506026.
[21] T. Skwarnicki *et al.*, DESY **F31-86-02**, (1986) (unpublished).
[22] H. Albrecht *et al.* (ARGUS Collaboration), Phys. Lett. B **241**, 278 (1990).

[23] K. Sakai, T. Kawasaki *et al.* (Belle Collaboration), Phys. Rev. D **82**, 091104 (2010). Since the high purity of pions in $B^{\pm} \to \eta\pi^{\pm}$ continumm component, we use the charge asymmetry in the continuum component to evaluate the charged pion detector bias, as there are fake kaons coming form protons in $B^{\pm} \to \eta K^{\pm}$ continumm component. We choose the $D_S^{+} \to \phi\pi^{+}[\phi \to K^{+}K^{-}]$ and $D^{0} \to K^{-}\pi^{+}$ samples to evaluate the charged kaon detector bias.